Marcelo Sampaio De Simone Teixeira

Effects of CO_2 injection on mechanical properties of carbonate rocks

Tese de Doutorado

Thesis presented to the Programa de Pós-graduação em Engenharia Civil of PUC-Rio in partial fulfillment of the requirements for the degree of Doutor em Ciências – Engenharia Civil.

Advisor: Prof. Deane de Mesquita Roehl
Co-Advisor: Prof. Lourdes Maria Silva de Souza

Rio de Janeiro
September 2022

Marcelo Sampaio De Simone Teixeira

Effects of CO_2 injection on mechanical properties of carbonate rocks

Thesis presented to the Programa de Pós-graduação em Engenharia Civil of PUC-Rio in partial fulfillment of the requirements for the degree of Doutor em Ciências – Engenharia Civil. Approved by the Examination Committee:

Prof. Deane de Mesquita Roehl
Advisor
Departamento de Engenharia Civil e Ambiental da PUC-Rio

Prof. Lourdes Maria Silva de Souza
Co-Advisor
Departamento de Engenharia Civil e Ambiental da PUC-Rio

Prof. Raquel Quadros Velloso
Departamento de Engenharia Civil e Ambiental da PUC-Rio

Prof. Janine Vieira
UFF

Prof. Leonardo Guimarães
UFPE

Prof. Fernanda Pereira
UERJ

Rio de Janeiro, September 2nd, 2022

Marcelo Sampaio De Simone Teixeira

Graduated in Civil Engineering at Pontifícia Universidade Católica do Rio de Janeiro (PUC-Rio) in 2013 and obtained his M.Sc. Degree in Civil Engineering from Pontifícia Universidade Católica do Rio de Janeiro (PUC-Rio) in 2016.

Bibliographic data

Teixeira, Marcelo Sampaio De Simone

Effects of CO_2 injection on mechanical properties of carbonate rocks / Marcelo Sampaio De Simone Teixeira; advisor: Deane de Mesquita Roehl; co-advisor: Lourdes Maria Silva de Souza. – 2022.
142 f. : il. color. ; 30 cm

Tese (doutorado) – Pontifícia Universidade Católica do Rio de Janeiro, Departamento de Engenharia Civil e Ambiental, 2022.
Inclui bibliografia

1. Engenharia Civil e Ambiental - Teses. 2. Rochas carbonáticas. 3. Solução de CO_2. 4. Análise experimental. 5. Método dos Elementos Discretos. I. Roehl, Deane de Mesquita. II. Souza, Lourdes Maria Silva de. III. Pontifícia Universidade Católica do Rio de Janeiro. Departamento de Engenharia Civil e Ambiental. IV. Título.

CDD: 624

To my family.

Acknowledgement

I would like to thank everyone who helped me during this PhD. Without them, it would not have been possible to finish it. I am especially grateful for my advisor, Professor Deane Roehl for all the guidance during my Masters and my PhD, and also for the opportunity to work in the project that this thesis was part of. I would also like to thank my co-advisor Dr. Lourdes Maria Souza for all the personal and technical discussions during this time. I am thankful to the Tecgraf team, that was always available for technical discussions. Among them, I thank Professor Fernanda Pereira for the ideas for DEM calibration, Nicole Vilar and Dr. Paola Manhães for the help with the graphic designs and image analysis, respectively, and, Hélvio Peixoto, for the discussions regarding the DEM theory. Also, in this topic I thank Dr. Krishna Kumar and Professor Giovanna Biscontin, who gave me ideas for the DEM study, and for all the help they gave me during my sandwich program at University of Cambridge. In the laboratory topic, I would like to thank everyone who made my experience inside the lab more positive. Among them, a special thanks to my co-advisor Dr. Lourdes, who helped me during all this experience, giving me confidence to work in a place (laboratory) that I have never stepped in before starting my PhD. In addition, I am thankful to all the LEM-DEC technicians: Bruno, Anderson, Rogério, Euclides, Jhansen, Marques and Zé for all the support during this time. I also thank Professor Leonardo Borghi and Marcelo Mendes, from UFRJ, for the coquina outcrop. I would like to thank Professor Sidnei Paciornik and Renata Lorenzoni for the Micro-CT scan at PUC-Rio, and Professor Janine Vieira for the Micro-CT scan at UFF. I thank Dr. Giancarlo Gonzales for helping me in the DIC procedure and analysis. In addition, I would like to thank Professor Raquel Velloso for all the help with the experimental tests in the MTS and GCTS triaxial systems, and also with the discussions regarding the DEM theory during her classes. At last, I thank my family for the support and patience during this period. My parents, Evandro and Celia, my brothers, Gustavo, Fernando and Felipe, my wife Yasmin and my son, Antônio. This study was financed in part by the Coordenação de Aperfeiçoamento de Pessoal de Nível Superior – Brasil (CAPES) – Finance Code 001. In addition, the sandwich program was financed by Conselho Nacional de Desenvolvimento Científico e Tecnológico (CNPq).

Abstract

Teixeira, Marcelo Sampaio De Simone; Roehl, Deane (Advisor); Souza, Lourdes Maria Silva (Co-advisor). **Effects of CO_2 injection on mechanical properties of carbonate rocks**. Rio de Janeiro, 2022. 142p. Tese de Doutorado - Departamento de Engenharia Civil, Pontifícia Universidade Católica do Rio de Janeiro.

CO_2 injection in depleted reservoirs has been largely employed over the past years as an effective process for oil and gas enhanced recovery. More recently, the injection of CO_2 in geological deposits is considered a viable alternative to reduce greenhouse gases in the atmosphere. In these two scenarios, the injected CO_2 interacts with the rock deposit altering some petrophysical and geomechanical properties. One of the main deposits is carbonate reservoirs.

The objective of this research is to improve the knowledge regarding the mechanical effects of CO_2 injection on carbonate rocks. Changes to the rock pore structure may change oil flow, cause reservoir compaction and containment issues. In order to improve the insight on the interaction between CO_2 and carbonate rocks, laboratory tests and numerical models were carried out in this study. For the laboratory tests, a solution of liquid CO_2 and deionized water was injected through Indiana Limestone and coquina samples. In addition, mechanical tests were executed before and after CO_2 injection, to evaluate the effects on the mechanical properties from the carbonate rocks. The mechanical characterization was conducted by performing uniaxial and triaxial compressive tests. From the laboratory results, significant reduction on the unconfined compressive strength and on Young's moduli from the coquina and Indiana Limestone samples when subjected to the CO_2 injection test was observed. In addition, an increase in porosity was also noted from MicroCT scans and porosimetry measurements on the coquina sample after the injection of CO_2 solution.

These results were used for the numerical model calibration and validation. Regarding the numerical model, the Discrete Element Method (DEM) was adopted. To accurately simulate the material behavior, a methodology encompassing the contact model, the sample generation and the calibration procedure is presented. The calibration of the DEM parameters used the results from the mechanical tests on the rocks prior and after the dissolution tests. The numerical model was able to

accurately simulate the uniaxial and triaxial tests on the Indiana Limestone and coquina samples. In addition, the methodology presented for the DEM model managed to accurately reproduce the mechanical degradation due to CO_2 injection on Indiana Limestone and to a lesser degree, on coquina samples.

Keywords

Carbonate rocks; CO_2 solution; Experimental analysis; Discrete Element Method.

Resumo

Teixeira, Marcelo Sampaio De Simone; Roehl, Deane; Souza, Lourdes Maria Silva. **Efeitos da injeção de CO_2 nas propriedades mecânicas de rochas carbonáticas**. Rio de Janeiro, 2022. 142p. Tese de Doutorado - Departamento de Engenharia Civil, Pontifícia Universidade Católica do Rio de Janeiro.

Injeção de CO_2 em reservatórios depletados tem ocorrido nos últimos anos como uma forma efetiva de recuperação avançada de óleo e gás. Mais recentemente, a injeção de CO_2 em depósitos geológicos vem sendo considerada uma alternativa viável para a redução da emissão de gases de efeito estufa na atmosfera. Nesses dois cenários, o CO_2 injetado reage com a rocha, alterando algumas de suas propriedades petrofísicas e geomecânicas. Um dos principais depósitos são os reservatórios carbonáticos.

O objetivo desta tese é aprimorar o entendimento em relação aos efeitos mecânicos da injeção de CO_2 em rochas carbonáticas. Esse tópico é de grande interesse para a indústria de óleo e gás, devido aos procedimentos de sequestro de CO_2 e recuperação avançada de óleo. Nesses dois cenários, o CO_2 é injetado em reservatórios carbonáticos, alterando algumas das propriedades petrofísicas e geomecânicas da rocha reservatório. Essas alterações podem aumentar os riscos relacionados à produção, uma vez que essas mudanças na estrutura porosa da rocha tendem a modificar o fluxo de óleo e também de provocar a compactação do reservatório. Com o objetivo de melhorar a compreensão da interação CO_2 e rochas carbonáticas, nesta tese foram feitos ensaios de laboratório e modelos numéricos. Para os ensaios de laboratório, uma solução de CO_2 e água deionizada foi injetada em amostras de Indiana Limestone e coquina. Também foram executados ensaios mecânicos antes e depois da injeção de CO_2, com o objetivo de avaliar os efeitos nas propriedades mecânicas das rochas carbonáticas. A caracterização mecânica foi realizada a partir de ensaios de compressão uniaxial e triaxial. Foram observadas consideráveis reduções nas resistências à compressão e nos módulos de Young das amostras de coquina e Indiana Limestone, quando submetidas ao ensaio de injeção de CO_2. Houve também um aumento na porosidade medida pelo MicroCT e pelo porosímetro na amostra de coquina sujeita a injeção de solução de CO_2.

Os resultados experimentais foram utilizados para calibração e validação dos modelos numéricos. Com relação aos modelos numéricos, o método dos elementos discretos (DEM) foi utilizado. Para simular de forma adequada o comportamento do material, uma metodologia, englobando o modelo de contato, a geração da amostra e o procedimento de calibração foi apresentada. A calibração dos parâmetros do DEM foi feita considerando os resultados dos ensaios mecânicos realizados antes e depois do ensaio de dissolução. O modelo numérico foi capaz de simular corretamente os ensaios uniaxiais e triaxiais realizados nas amostras de Indiana Limestone e coquina. Adicionalmente, a metodologia apresentada para o modelo em DEM conseguiu gerar bons resultados considerando a degradação pela injeção de CO_2 das propriedades mecânicas da Indiana Limestone, e resultados satisfatórios para a coquina.

Palavras-chave

Rochas carbonáticas; Solução de CO_2; Análise experimental; Método dos Elementos Discretos.

Content

List of Figures

List of Tables

1
Introduction

1.1.
Thesis background

There is an increasing interest from the oil and gas industry, and society in general, in understanding the interaction between CO_2 solution and reservoir rocks. This interest is mainly due to two main procedures, enhanced oil recovery (EOR), performed by the oil and gas industry and CO_2 sequestration, which recently has been considered a viable alternative to reduce greenhouse gases.

Several works investigate CO_2 sequestration as an option for reducing CO_2 emission into the atmosphere. The process of CO_2 capture and storage (CCS) is very complex, as it includes capture, transport and storage of CO_2. In Leung et al. (2014), all the steps of a CCS are described. Here, the main interest is on the storage step, where CO_2 is injected in depleted reservoirs or in deep saline aquifers.

As CO_2 injection occurs in a reservoir/aquifer, it is first trapped in a hydrogeological way. This trapping is due to geological barriers in the form of low permeability caprocks (e.g., shale or salt), avoiding CO_2 solution migration back to the atmosphere. Then, geochemical trapping occurs, as described in Gunter et al. (2004), which consists of a sequence of chemical interactions between CO_2, formation fluid and rock minerals. Those trapping mechanisms assure the safety of the storage procedure; therefore, they must be carefully studied in order to assure short- and long-term CO_2 containment.

The storage is usually carried out in sandstones and carbonate rocks, due to their porosity and permeability (Bachu, 2008). As reservoirs have maintained oil and gas securely trapped over a long period of time, they are good candidates for CO_2 sequestration. In addition, as oil and gas are depleted from those reservoirs, voids and low-pressure regions are formed, which can be filled with injected CO_2.

Another application is the injection of CO_2 in reservoirs to enhance oil recovery. The use of CO_2 as the injected gas is due to its low minimum miscible pressure over other gases (Gozalpour et al., 2005). Hence, CO_2 and hydrocarbon are completely miscible, forming a

unique fluid, eliminating capillary effects. In addition, miscibility reduces oil viscosity, increasing fluid mobility, and consequently, raising oil production.

EOR using CO_2 is an alternative to increase oil production, since conventional methods are not able to produce the totality of hydrocarbon from the reservoir. Another technique is to alternate between gas and water injection, known as WAG (Water-Alternating-Gas), in order to control oil fingering (Manrique et al., 1998).

When CO_2 mixes with formation water, an acid solution is formed. Therefore, it is crucial to understand better how the CO_2 acid reacts with reservoir rocks. Elastic and strength properties are altered during this reaction, which can increase risks for oil and gas production and for formation stability, by the occurrence of subsidence and reservoir compaction (Eide, 2012). Rock porosity and permeability are also affected, blocking flow pathways inside the rock, or enhancing CO_2 migration out of the storage volume, as presented by Rochelle et al. (2004) and Hawez and Ahmed (2014). The changes in rock structure are different according to mineralogy, flow rate, temperature, pressure, and some other parameters (Rochelle et al., 2004), making it more difficult to understand the interaction between CO_2 solutions and rocks.

Regarding the changes observed on the rock mechanical properties, only a few works investigate these changes on carbonate rocks. Sun et al. (2016) studied the variation of mechanical properties of Entrada sandstone and Summerville siltstone coming from the reaction with CO_2. In that work, the authors performed a scratch test on samples that were naturally altered by CO_2-charged brine. Four samples were considered in that study: unaltered and CO_2-altered Entrada sandstone and Summerville siltstone. The authors observed a decrease in the indentation hardness, Young's modulus, scratch hardness, and fracture toughness from 12% to 87% when comparing the original with the CO_2-altered rocks. Marble et al. (2013) also studied the changes in sandstone properties due to dissolution. In this case, the authors altered the sandstone samples by the reaction with pure super critical CO_2 inside an autoclave. Then, geochemical and geomechanical behavior were studied. The authors observed a decrease in the strength parameters, changes in elastic deformation and in effective porosity on the altered samples, when compared to unaltered sandstone samples.

Most Brazilian pre-salt reservoirs are carbonate rocks, which is particularly interesting when dealing with CO_2 injection due to rock complexity and heterogeneity. Carbonate reservoirs usually consist of carbonate rocks with formation water inside their pores. During its injection, CO_2 dissociates in the formation water, forming carbonic acid (H_2CO_3) in the subsurface. Then diffusive and convective processes are responsible for the acid transport through the reservoir. When this acid reaches the mineral surface, the reaction between the acid

and the mineral starts. Later, the product of the reaction is transported away from the reaction surface. This process is responsible for increasing or decreasing rock porosity and permeability, depending on the phenomenon. In the case of dissolution, rock porosity and permeability increase in the volume where the mineral is reacting with the acid. On the other hand, when precipitation occurs, rock porosity and permeability decrease due to the formation of calcium carbonate inside the pores, closing pores and some flow paths.

Due to the complexity of the interaction of CO_2 solution and carbonate rocks, more experimental and numerical studies should be carried out to better understand this interaction. In laboratory experiments, there are challenges when dealing with the CO_2-rock interaction, such as lack of adequate equipment, reduced number of available samples, among others. Therefore, numerical models are also used to improve the number of scenarios that can be studied. As such, some methods at grain-scale analyses are adopted in the literature. Molecular Dynamics, which is more often used to simulate atoms and molecules, is presented in Phillips et al. (2005). Another approach is the Material Point Method, which uses particles and a grid in the simulation (Sulsky et al., 1995). In this method, all the continuum information is carried in the numerical material points (particles), while the grid carries no permanent information. Monaghan (1994) presented the Smoothed Particle Hydrodynamics (SPH), which is a Lagrangian particle method and is used to simulate compressible and incompressible flow without a grid. Among the Meshless Finite Element Methods, Idelsohn et al. (2003) and Cante et al. (2009) present the Particle Finite Element Method (PFEM). In this method, the particles move according to the equations of motion, and the mesh needs to be rebuilt at the end of each time step. One of the most widely used methods to simulate the solid grain is the Discrete Element Method (DEM), developed by Cundall and Strack (1979). This method is based on Newton's second law and force displacement equations.

1.2. The Coupled Geomechanics project

The study presented here is part of a research project entitled "Coupled Geomechanics". This was a large project with different topics, as summarized by the workflow in Figure 1-1. The objective was to develop mathematical formulations and numerical codes to study geomechanical problems at multiple scales, by coupling different physics. For that, a multi-scale and multi-physics simulator was developed. Several researchers were part of this project, working on different topics. This thesis was part of the grain-fluid interaction topic, as shown in the blue boxes in Figure 1-1. The results from this work may contribute to the study of

wellbore and reservoir modelling, if an upscale technique is adopted. The use of the Discrete Element Method for the grain scale behavior can be used as a numerical laboratory to improve the modelling in different scales.

The multi-physics portal is a tool created to improve the collaboration among the researchers. In this portal, data and algorithms developed by the Tecgraf group can be shared with other researchers around the world.

In this project, a collaboration between PUC-Rio and University of Cambridge took place and part of this thesis was developed in a sandwich program at University of Cambridge for 6 months, under the supervision of Prof. Giovanna Biscontin and Dr. Krishna Kumar, both with expertise in numerical modelling.

Part of this thesis was developed during the Covid-19 pandemic. From March until July 2020, the Structures and Materials Laboratory of the Civil and Environmental Engineering Department at PUC-Rio was closed. Then, access was very limited, with interruption of operations whenever a Covid case occurred within the workers. Other university facilities and laboratories remained shut for the remainder of the pandemic period. Overall, such limitations posed extra challenges to the development of the experimental program.

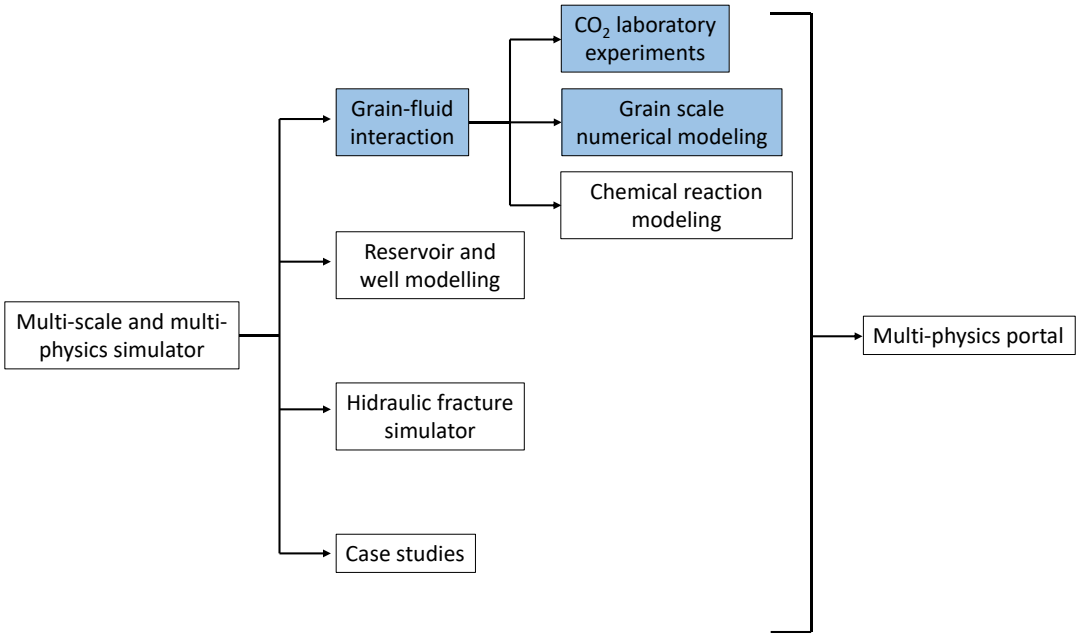

Figure 1-1 – Workflow for the Coupled Geomechanics project. The topics in the blue boxes were developed in this thesis.

1.3. Objectives of the thesis

The main goal of this thesis is to investigate the effects of CO_2 injection on the mechanical properties and microstructure of carbonate rocks, through numerical and experimental tests. This study is focused on carbonate rocks, as it is a very common rock in the Brazilian pre-salt fields. The methodology considered the development of numerical models while performing laboratory experiments for calibration and validation. For the numerical model, the Discrete Element Method (DEM) was adopted, as it can naturally represent rock failure, is easier to implement and is commonly used to study rock behavior when compared with other discrete models. On this front, this study aimed to develop a numerical methodology, by implementing a contact model, a sample preparation technique, and a calibration procedure. Regarding the laboratory work, the objective is to investigate the changes on the rock mechanical properties, such as uniaxial compressive strength, Young's modulus and Poisson's ratio and on the microstructure due to the injection of a CO_2 solution.

1.4. Outline of the thesis

This study investigates the effect of CO_2 solution injection on the mechanical properties of carbonate rocks. Numerical models and experimental tests were conducted to improve this understanding. In the next chapter, an overview of the interaction between CO_2 and carbonate rocks is presented, with a brief literature review on the carbonate dissolution process.

Then, Chapter 3 presents the numerical model with the DEM theory. Also, in Chapter 3, all the necessary steps for developing the DEM model are discussed, such as sample generation, definition of the contact model, and parameter calibration.

In Chapter 4, the experimental methods used in this thesis are described. In addition, the experimental tests for rock characterization and CO_2 injection on Indiana Limestone and coquina samples are presented.

Lastly, in Chapter 5, a comparison between numerical and laboratory results is carried out. In this comparison, uniaxial and triaxial test simulations in DEM are compared to the experimental results. Then, the strength values from the multi-stage triaxial tests in the laboratory are compared with the ones obtained from single triaxial test simulations in the DEM model for the samples before and after the CO_2 injection.

The thesis scheme is presented in Figure 1-2.

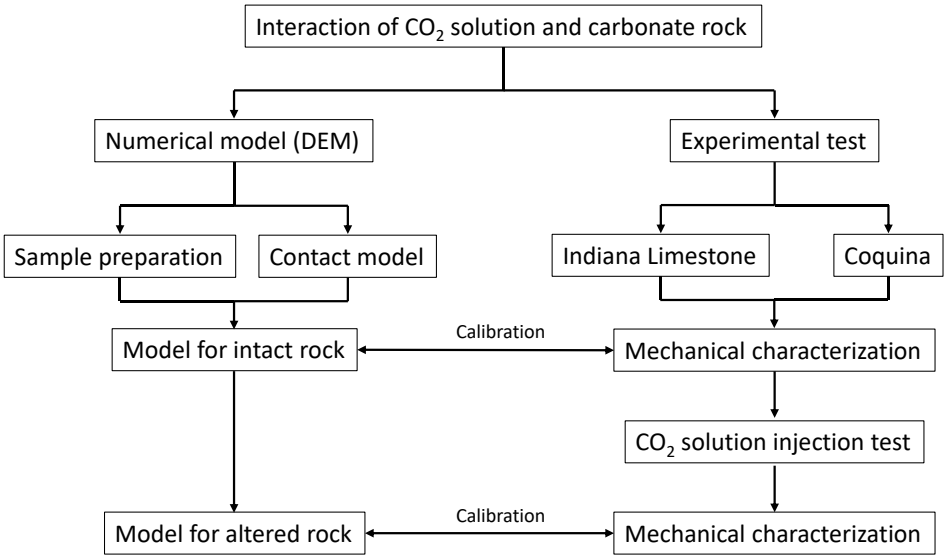

Figure 1-2 – Thesis outline with the main steps.

2
Interaction between CO_2 and carbonate rocks

This study focuses on the interaction between CO_2 and carbonate rocks, once they are very common as oil and gas reservoirs, especially in the Brazilian pre-salt fields. The main minerals forming those carbonate rocks are calcite ($CaCO_3$) and dolomite ($CaMg(CO_3)_2$). This thesis studies the mechanical alterations caused by CO_2 injection on rocks composed mostly by calcite. An important phenomenon responsible for this mechanical alteration is calcite dissolution. This process is described by a chemical reaction presented in equation (2.1), explained in Vaz (2017).

$$\begin{aligned} CO_2 + H_2O \leftrightarrow H_2CO_3 \leftrightarrow H^+ + HCO_3^- \\ H^+ + HCO_3^- + CaCO_3 \leftrightarrow Ca^{2+} + 2HCO_3^- \end{aligned} \tag{2.1}$$

This mineral dissolution is influenced by some factors, such as mineral surface area, solution concentration and temperature. These effects are considered when assessing the dissolution rate, as presented by Yasuda et al. (2018) and Noiriel et al. (2009). Noiriel et al. (2009) present the calcite dissolution rate in equation (2.2).

$$r = S_r \cdot k_c \cdot (1 - \Omega_{cal}) \tag{2.2}$$

where S_r is the reactive surface area of the mineral (specific surface area – normalized to a volume of water), k_c is the overall kinetic dissolution rate and Ω_{cal} is the calcite saturation index. The saturation index (Ω_{cal}) determines if the water is saturated, undersaturated or supersaturated concerning a specific mineral, depending on the ion activity product (IAP) as presented in equation (2.3).

$$\begin{aligned} \Omega_{cal} = 0 \rightarrow IAP = K_{calcite} \rightarrow \text{Saturated (in equilibrium)} \\ \Omega_{cal} < 0 \rightarrow IAP < K_{calcite} \rightarrow \text{Undersaturated} \\ \Omega_{cal} > 0 \rightarrow IAP > K_{calcite} \rightarrow \text{Supersaturated} \end{aligned} \tag{2.3}$$

In order to understand how this interaction between CO_2 and rocks affects the behavior of the rock, laboratory tests and numerical models have been carried out in the literature. Regarding the laboratory tests, Grgic (2011) presented a coupled test in which supercritical / gaseous CO_2 and CO_2 saturated aqueous solutions were injected in Lavoux Limestone samples. The procedure of fluid injection was carried out using an open (injected acid solution is continuously renewed) and a closed (aqueous fluid recirculation) system in a flow-through

triaxial cell. The dimensions of all samples were 38 mm in diameter and 76 mm in length. The samples were tested under reservoir conditions, with 20 MPa confining pressure and 70°C, simulating a depth of 800 m from the Paris basin. From the open system tests, it was noticed a significant dissolution of calcite at the sample/piston interface. This dissolution is mostly influenced by the flow rate of the injected solution. Compaction of the sample was observed under open conditions, mainly because of calcite dissolution (purely chemical effect).

Also using a triaxial cell, Le Guen et al. (2007) injected CO_2 rich fluid in four samples with diameter of 23 mm and length of 48 mm: one sample of Estaillades Limestone, two of Lavoux Limestones and one of Arkosic Sandstone. During the experiments, high and low partial pressure of carbon dioxide (P_{CO2}) fluids were injected in the samples during several days. The authors recorded the strain and the strain rate during each period of the test. In addition, the porosity distribution was evaluated using X-ray tomography images taken before and after the experiments. According to the authors, instantaneous compaction was induced mostly by a mechanical effect and secondly by chemical reactions. The long-term strain was controlled by some parameters discussed by the authors, such as the vertical effective stress, mineralogy, internal structure, fluid flow rate and fluid P_{CO2}.

Yu et al. (2019) studied the changes caused by the injection of a brine-CO_2 solution on a synthetic sandstone under high temperature and high pressure. They did not observe a significant change on sample porosities. The authors also noticed a dissolution on calcite and dolomite, but not on quartz, K-feldspar and albite. The small porosity change may be due to the mineral composition of the sample, which consists of 81.6% of quartz, K-feldspar and albite, while only 18.4% is calcite, kaolinite and dolomite.

Focusing on the changes in the reactive surface, Noiriel et al. (2009) presented a study of a limestone during dissolution. A flow-through experiment was carried out on an Upper Miocene limestone, injecting a solution with NaCl diluted in deionized water in equilibrium with CO_2. The authors observed a decrease in calcite mass and increase in pore volume, related to porosity increase. Luquot and Gouze (2009) performed a study considering different flow rates and CO_2 partial pressures. These two different flow rates mimic two scenarios: near and far the injection well. The authors performed four percolation tests injecting a solution of brine and CO_2, varying the partial pressure of CO_2, applying 10, 6, 2.5 and 0.75 MPa. The authors observed that higher values of P_{CO2} show non-uniform sample dissolution, governed by transport-controlled mass transfer. On the other hand, lower P_{CO2} causes more uniform degradation, related to reaction-controlled dissolution.

Lebedev et al. (2017) studied the influence of CO_2 solution on carbonate rocks, considering an oolitic limestone, using a solution with brine and CO_2. They concluded that the permeability and porosity of the rock significantly increased after dissolution, and the rock matrix weakened (around 47% in indentation modulus) after exposure to the solution. Eide (2012) performed a retarded acid (10% of retarded acid and 90% of tap water) treatment in stages in an Euville limestone and assessed the influence on the rock properties. The author observed a reduction on Young's Modulus and strength parameters mostly associated to porosity increase. Bemer et al. (2016) also conducted a retarded acid (acetic acid - injection test) to reach a more homogeneous rock dissolution. From their experiments, a reduction on the Euville Limestone stiffness was observed due to chemical alteration.

Focusing on coquina samples, Monte-Mor and Trevisan (2016), Filho (2017) and Yasuda et al. (2018) presented dissolution tests on samples from Morro do Chaves. Filho (2017) carried out the dissolution test in a close circuit system, injecting solutions with brine or water and CO_2 in the sample, inside a vessel for 240 hours under reservoir conditions (9000 psi and 64 ºC). The author observed an increase in the dissolution rate, when increasing sample initial porosity. Yasuda et al. (2018) performed a continuous injection of CO_2-brine solution in a coquina sample while performing computer tomography (CT) scans. From the scans, the authors noticed the formation of wormhole and preferred flow channels. Also using tomography, Monte-Mor and Trevisan (2016) focused on the effect of CO_2-brine solution on permeability and porosity applying different injection rates. They concluded that these rates caused different dissolution patterns, as low flow rates were not able to remove the loose particles, which had been previously dissolved.

Dissolution studies on Indiana Limestone plugs were also carried out in the literature. Zhou et al. (2009) studied the changes on the Mohr-Coulomb parameters of Indiana Limestone samples when performing a WAG (with brine and CO_2) injection. The authors performed the experiment at a temperature of around 57 ºC, injecting 6000 ml of fluid. Most of the samples showed a reduction on the Mohr-Coulomb parameters, as well as a decrease in the Young's modulus and the strain ratio (lateral / axial strains considering 5000 psi of confining pressure) when subjecting the sample to the injection experiment. Morschbacher et al. (2015) injected a solution with brine and CO_2 in an Indiana Limestone and Silurian Dolomite and observed an increase on the Indiana Limestone porosity from 16.7% to 19.0%, while for the Silurian Dolomite, this increase was more subtle, from 16.0% to 16.8%. In addition, compressional and shear wave velocities were obtained for samples before and after solution injection, with a reduction of approximately 5% on Indiana Limestone V_P and V_S.

In addition to Morschbacher et al. (2015), Vialle and Vanorio (2011) also studied the influence of CO_2 injection on compressional and shear wave velocities. Vialle and Vanorio (2011) injected a solution with CO_2 and water through different carbonate rocks, while measuring elastic and transport properties. The chalk samples presented higher variations on the elastic properties, reaching a decrease of 871 m/s in the compressional wave velocity and 443 m/s in the shear wave velocity. The authors also obtained higher reaction rates in calcite than in dolomites, which is also confirmed in other literature works, such as in Morschbacher et al. (2015). In addition, a characteristic observed by the authors in the chalks that may explain the higher variations on the elastic properties is the higher reactive surface area.

Considering synthetic carbonate rocks, Melo (2012) studied the changes on the material porosity and permeability due to the injection of a HCl solution. The results showed that the porosity increased around ten times the initial porosity for two of the tested samples, while this increase was one hundred times the initial porosity for the third tested sample. Oliveira (2016) carried out a similar study, but considering also the influence of the solution on the uniaxial compressive strength of the material. Regarding the porosity change observed in the synthetic rocks, Oliveira (2016) reached the same results as Melo (2012). For the material strength, Oliveira (2016) noticed a decrease on the uniaxial compressive strength from an average of 2 MPa to values around 0.2 MPa, depending on the pH of the adopted solution (pH of 2, 3 and 4).

Table 2-1 presents an overview of the main test parameters used in the laboratory for the dissolution studies discussed in this section. The major concern of previous laboratory studies was the pore structure alteration of the tested rocks, influencing porosity and permeability. In this thesis, the main focus is the investigation of the effects of injecting a CO_2 solution on the mechanical properties of carbonate rocks, by performing laboratory tests and numerical models. In the experimental study, the alterations on the pore structure will be assessed in a general aspect, while in the numerical study, only the variations on mechanical properties will be evaluated.

Table 2-1 – Main test parameters used in laboratory for the dissolution studies.

Study	Rock	Fluid	Flow rate	Pore pressure	P_{CO2}	Confining pressure	Temperature	Test duration
Grgic (2011)	Lavoux oolitic Limestone	CO_2 + Water	0.006 - 0.6 ml/min	4.5 - 10 MPa	4.5 - 10 MPa	15 - 20 MPa	30 – 70 ºC	18 - 79 days
Le Guen et al. (2007)	Estaillades and Lavoux Limestone / Arkosic Sandstone	CO_2 + Water / CO_2 + Brine	0.005 ml/min	5.9 - 8.3 MPa	$10^{-4.5}$ - 8.3 MPa	7.3 - 12 MPa	25 – 80 ºC	40 days - 6 months
Yu et al. (2009)	Synthetic Sandstone	CO_2 + Brine	-	48.45 MPa	48.45 MPa	60 MPa	150 ºC	4 - 16 days
Noiriel et al. (2009)	Miocene Limestone	CO_2 + Brine	1.67 ml/min	0.10 MPa	0.10 MPa	0.10 MPa	20 ºC	15 hours
Luquot and Gouze (2009)	Oolitic Limestone	CO_2 + Brine	0.6 – 1.14 ml/min	0.75 - 10 MPa	0.75 - 10 MPa	12 MPa	100 ºC	-
Lebedev et al. (2017)	Savonnières limestone	CO_2 + Brine	0.5 ml/min	10 MPa	10 MPa	15 MPa	50 ºC	360 PV injected
Eide (2012)	Euville carbonate	Retarded acid solution	0.05 - 0.4 ml/min	10 MPa	-	15 MPa	80 ºC	15 - 24 hours
Bemer et al. (2016)	Euville limestone	Acetic acid	-	0.4 MPa	-	3 MPa	60 ºC	1 day
Monte-Mohr and Trevisan (2016)	Coquina	CO_2 + Brine	0.05 - 0.5 ml/min	13.8 MPa	13.8 MPa	20.7 MPa	25 ºC	4 PV injected
Filho (2017)	Coquina / Silurian dolomite	CO_2 + Water / CO_2 + Brine	-	3.45 - 62 MPa	3.45 - 62 MPa	-	64 ºC	240 hours
Yasuda et al. (2018)	Coquina	CO_2 + Brine	0.5 - 2 ml/min	13.8 MPa	13.8 MPa	-	20 ºC	178 PV injected
Zhou et al. (2009)	Indiana Limestone	WAG	0.5 ml/min	-	-	-	58 ºC	6000 ml
Morschbacher et al. (2015)	Indiana Limestone and Silurian Dolomite	CO_2 + Brine	5 ml/min	-	-	-	-	-
Vialle and Vanorio (2011)	Carbonates	CO_2 + Water	4 - 8 ml/min	-	-	1.1 - 8 MPa	-	-
Oliveira (2016)	Synthetic Carbonates	HCl + Water	-	0.1 MPa	-	0.15 MPa	Room temperature	-
Melo (2012)	Synthetic Carbonates	HCl + Water	-	0.1 MPa	-	0.15 MPa	-	-

3
Numerical modeling – Discrete Element Method

In 1979, the Discrete Element Method (DEM) was developed by Cundall and Strack (1979) using sphere particles as bodies to study the behavior of granular assemblies. This method was used first to simulate the movement of granular material, such as sands. Then, other features were added to this method, so it could also simulate rock behavior. This approach has two assumptions for the contact behavior: hard sphere and soft sphere contacts. Hard sphere contact considers the interaction as instantaneous and the collisions are processed one by one. Consequently, this model is faster than the soft sphere assumption when simulating not too dense systems (Deen et al., 2007). On the other hand, the soft sphere model is able to simulate multi-particle contacts, and therefore is more often used in dense systems.

The discrete element method is widely used to understand qualitatively the behavior of different materials in different situations. An example is the work from Nwodo et al. (2016), who focused on sand production, using DEM and Darcy fluid flow.

An important characteristic of most of the DEM simulations in the literature, is the size of the particles adopted. Usually, there is a difference between the DEM particle size and the real material grain size. In this case, each DEM particle can be considered as a group of grains, and the DEM model considering this set of particles tries to reproduce the same behavior observed in the real material.

3.1.
Theory

3.1.1.
Discrete element method

Calculations in the discrete element method are based on Newton's second law and force-displacement law, as developed by Cundall and Strack (1979).

Particle movement is represented by Newton's law, in equation (3.1).

$$F = m \cdot \ddot{x} \tag{3.1}$$

where m and $\ddot{x}$ are the body mass and acceleration, respectively, and F is the force acting on the body. This approach considers soft particle contact, meaning that the particle is rigid, but the contact is not. This feature is simulated by an overlap between particles in contact, creating a force on each body related to the overlap, as presented in Figure 3-1.

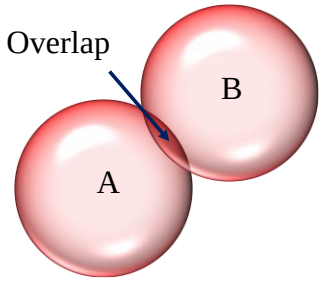

Figure 3-1 – A contact between two particles, considering the soft particle approach, used in this work.

This overlap between two contact spheres (sphere A and sphere B) is given by equation (3.2).

$$u_n = R_A + R_B - \|x_A - x_B\| \tag{3.2}$$

where u_n is the overlap, R_A and R_B are the body radii and x_A and x_B are the positions of the particle centers. Considering a force acting on a particle, it is possible to obtain the acceleration of this particle from equation (3.1). Therefore, the velocity is calculated by integrating the acceleration in time. Using the same procedure, the new position of the particle in the next time step can be approximated by integrating the velocity.

Two basic interaction forces need to be computed when dealing with the DEM: normal force and tangential force. DEM computes normal forces from the overlap between two spheres, while tangential forces are computed from the relative velocity between these two spheres. The simplest contact law used in DEM is the normal elastic force (F^n), which considers springs with normal stiffness (k_n) at the contact, as equation (3.3).

$$F_n = k_n \cdot u_n \tag{3.3}$$

It is possible to add a second term to equation (3.3) related to a dissipative coefficient (c). Therefore, equation (3.4) accounts for a conservative part and a dissipative one, as presented in Cundall and Strack (1979).

$$F_n = k_n \cdot u_n + c \cdot \frac{du}{dt_i} \tag{3.4}$$

Another approach considering the normal force is developed by Heinrich Hertz, presented by Poschel and Schwager (2005), equation (3.5).

$$F_n = \frac{2 \cdot Y \cdot \sqrt{R^{eff}}}{3 \cdot (1 - \nu^2)} \cdot \left(u_n^{\frac{3}{2}} + c \cdot \sqrt{u_n} \cdot \frac{du_n}{dt_i} \right) \tag{3.5}$$

with R^{eff} being the effective radius of the colliding spheres, c the dissipative constant (function of the material viscosity), Y Young's modulus and ν Poisson's ratio. Besides the normal force, the tangential force also acts at the contact between two spheres. According to Velloso (2010), equation (3.6) presents the increment of the tangential force (ΔF_s).

$$\Delta F_s = k_s \cdot v_c^s \cdot \Delta t_i \tag{3.6}$$

where k_s is the tangential stiffness and v_c^s is the relative tangential velocity at the contact. This force is limited by $F_s^{\max}$, presented in equation (3.7).

$$F_s^{max} = \mu \cdot |F_n| \tag{3.7}$$

Here, μ is the friction coefficient. When the tangential force exceeds the maximum tangential force ($F_s > F_s^{max}$), equation (3.8) must be used, maintaining the force sign.

$$F_s = sign(F_s) \cdot F_s^{max} \tag{3.8}$$

In order to integrate the accelerations and velocities correctly, the time step must be small enough to be able to capture any contact. Besides that, this time increment must be small enough to affect only the immediate neighbors, as explained by Cundall and Strack (1979). Therefore, the most used methods in the literature to solve these equations are the finite difference method and the predictor/corrector method (Gear's integration scheme). The finite difference method is based on the expansion of Taylor's series, using a second order approximation. This procedure is carried out to find the position according to the time increment, as equation (3.9).

$$x(t + \Delta t) = x(t) + v\left(t + \frac{\Delta t}{2}\right) \cdot \Delta t \tag{3.9}$$

The same applies to finding the velocities for the half of the time increment, as in equation (3.10).

$$v\left(t + \frac{\Delta t}{2}\right) = v\left(t - \frac{\Delta t}{2}\right) + a(t) \cdot \Delta t \tag{3.10}$$

The other method used in the literature is the predictor - corrector, presented by Poschel and Schwager (2005) as Gear's Integration Scheme. First, this method computes the positions and their time derivatives at time $t + \Delta t$ using a Taylor expansion (predictor). These values are

then used to calculate the forces, and with them, another acceleration can be computed (corrector). The next step is the calculation of the difference between the predictor and the corrector acceleration. This difference is used to compute the corrector value of the position and its time derivatives, as presented in equation (3.11).

$$
\begin{aligned}
x_i^{corr}(t+\Delta t) &= x_i^{pr}(t+\Delta t) + \mathrm{c}_0 \cdot \frac{\Delta t^2}{2} \cdot \Delta\ddot{x} \\
v_i^{corr}(t+\Delta t) &= v_i^{pr}(t+\Delta t) + \mathrm{c}_1 \cdot \frac{1}{\Delta \mathrm{t}} \cdot \frac{\Delta t^2}{2} \cdot \Delta\ddot{x} \\
\ddot{x}_i^{corr}(t+\Delta t) &= \ddot{x}_i^{pr}(t+\Delta t) + \mathrm{c}_2 \cdot \frac{2}{\Delta t^2} \cdot \frac{\Delta t^2}{2} \cdot \Delta\ddot{x} \\
\ddot{x}_i^{corr}(t+\Delta t) &= \ddot{x}_i^{pr}(t+\Delta t) + \mathrm{c}_2 \Delta\ddot{x}
\end{aligned}
\tag{3.11}
$$

The values of each constant $(c_0, c_1, c_2, \ldots)$ depend on the Gear algorithm order, as presented by Poschel and Schwager (2005). A comparison between these two integration methods is presented in Appendix B.

3.1.2. Mechanical bonded contact models

In the present work, DEM models were developed to simulate the rock mechanical behavior. In the discrete element method, the contact models can be considered as the constitutive laws, once they are responsible for representing the macro behavior observed in real materials. They can be divided into two groups: cohesive models and collision models. The former describes best rocks and cohesive materials, while the latter applies to soil simulations.

This study focuses on rock simulations, therefore cohesive contact models are discussed in this section. There are different contact models in the literature, and some variations of these models, as they are improved with time. One of the most used cohesive contact models is the Bonded Particle Model (BPM) developed by Potyondy and Cundall (2004) and implemented in the commercial software PFC. This model considers a cement beam connecting two particles in mechanical contact, transferring forces and moments from one particle to the other. Pure frictional contact also occurs, in parallel to the bonded one.

Scholtès and Donzé (2013) developed the Jointed Cohesive Frictional (JCF) model, available in the open software *Yade* (Šmilauer et al., 2021). JCF provides resistance to normal and shear stresses, and if the applied stress reaches the corresponding resistance, the bond breaks. In this model, the average number of bonds per particle can be controlled by allowing

near neighbor interactions, which can help controlling the sample interlocking. In addition, it enables modeling of pre-existing fractures by the use of joints in the simulation.

In this section, two bonded contact models are explained in detail, as both of them are used in this thesis: the JCF and the BPM. The JCF contact model is used for sample preparation and parameter calibration studies, as it requires the definition of less parameters. A modified version of the BPM contact model is used for the comparison between numerical and experimental results.

3.1.2.1. Bonded Particle Model

The bonded particle model is widely used as a contact model for bonded particles in discrete element simulations. The BPM consists of two particles joined by a cement bond, as presented in Figure 3-2, for the three-dimensional case. The equations are presented below for the two and three-dimensional cases.

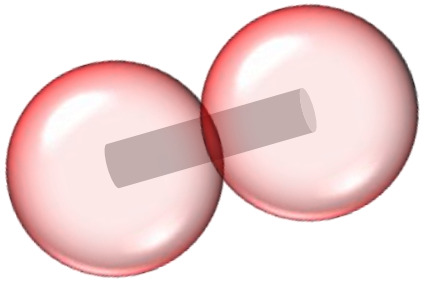

Figure 3-2 – Two particles with the BPM contact (3D).

When two particles overlap and the bond between them is considered, the grain-grain and the grain-cement behaviors must be assessed. First, the force from the overlap, considering only the grain-grain contact is evaluated according to equation (3.12).

$$F = F_n \cdot n_i + F_s \cdot s_i$$
$$F_n = k_n \cdot u_n \tag{3.12}$$
$$F_s = \{F_s\}_{updated} + \Delta F_s \text{ where } \Delta F_s = -k_s \cdot \Delta u_s \text{ and } \Delta u_s = v_c^s \cdot \Delta t$$

In equation (3.12), F is the total force on one particle, F_s and F_n are the shear and normal components, respectively; n_i and s_i are the normal and tangential directions. The normal and shear stiffnesses are k_n and k_s, u_n is the overlap, v_c^s is the relative tangential velocity at the contact, and Δu_s and ΔF_s are the increments of shear displacement and shear force, respectively, for a time increment Δt_i.

The tangential force is limited by $F_s^{\max}$ as presented in equation (3.13).

$$F_s^{max} = \tan(\phi) \cdot |F_n| \tag{3.13}$$

Here, ϕ is the friction angle. In the case the tangential force exceeds the maximum force ($F_s > F_s^{max}$), equation (3.14) must be used.

$$F_s = sign(F_s) \cdot F_s^{max} \tag{3.14}$$

Additionally, the bond part (beam connecting the particle centers) is assessed. The bond radius ($\bar{R}$) depends on the value of the beam radius coefficient ($\bar{\lambda}$), particle A radius (R_A) and particle B radius (R_B) and is presented in equation (3.15).

$$\begin{gathered} \bar{R} = \bar{\lambda} \cdot \min(R_A, R_B) \\ 0.0 \leq \bar{\lambda} \leq 1.0 \end{gathered} \tag{3.15}$$

The bond forces and moments are set to zero when creating the bonded contact. Then, force and moment increments are evaluated at each time step and are added with the ones from the previous step. The force and moment increments are presented in equation (3.16).

$$\begin{aligned} \Delta\bar{F}_n &= \bar{k}_n \cdot \bar{A} \cdot \Delta u_n \\ \Delta\bar{F}_s &= -\bar{k}_s \cdot \bar{A} \cdot \Delta u_s \\ \Delta\bar{M}_n &= -\bar{k}_s \cdot \bar{J} \cdot \Delta\theta_n \\ \Delta\bar{M}_s &= -\bar{k}_n \cdot \bar{I} \cdot \Delta\theta_s \end{aligned} \tag{3.16}$$

Here, A, J and I are the area, polar moment of inertia and the moment of inertia of the bond cross section, respectively. The superscript $\overline{[x]}$ indicates bond properties. The geometric properties ($\bar{A}$, $\bar{J}$ and $\bar{I}$) are evaluated according to equation (3.17).

$$\begin{aligned} \bar{\mathrm{A}} &= \begin{cases} 2 \cdot \bar{R} \cdot l \ , l = 1 & (2D) \\ \pi \cdot \bar{R} & (3D) \end{cases} \\ \bar{\mathrm{J}} &= \begin{cases} NA & (2D) \\ \dfrac{1}{2} \cdot \pi \cdot \bar{R}^4 & (3D) \end{cases} \\ \bar{\mathrm{I}} &= \begin{cases} \dfrac{2}{3} \cdot \bar{R}^3 \cdot l \ , l = 1 & (2D) \\ \dfrac{1}{4} \cdot \pi \cdot \bar{R}^4 & (3D) \end{cases} \end{aligned} \tag{3.17}$$

In order to assess bond integrity, the maximum normal and shear stresses are calculated according to equation (3.18).

$$\bar{\sigma}^{\max} = -\frac{\bar{F}_n}{\bar{A}} + \frac{|\bar{M}_s| \cdot \bar{R}}{\bar{I}} < \overline{\sigma_C} \tag{3.18}$$

$$\bar{\tau}^{\max} = \frac{|\bar{F}_s|}{\bar{A}} + \frac{|\bar{M}_n| \cdot \bar{R}}{\bar{J}} < \overline{\tau_C}$$

If the maximum tensile stress reaches the tensile strength ($\bar{\sigma}_c$) or if the maximum shear stress equals the shear strength ($\bar{\tau}_c$), the parallel bond breaks. After bond breakage, the forces acting on the pair of particles are only those from grain-grain contact.

3.1.2.2. Jointed Cohesive Frictional

In the *Yade* user's community, the most used contact model to simulate rock behavior is the jointed cohesive frictional model (JCF). Its formulation is presented below (Scholtès and Donzé, 2013). The normal force (F_n) is

$$F_n = k_n \cdot u_n \tag{3.19}$$

The maximum tensile force (F_n^{max}) is defined in equation (3.20), where t is the tensile strength and A_{int} is the contact surface, defined as $A_{int} = \pi \cdot (\min(R_A, R_B))^2$.

$$F_n^{max} = -t \cdot A_{int} \tag{3.20}$$

Equation (3.21) presents the shear force, where k_s is the shear stiffness and Δu_s is the tangential displacement increment.

$$F_s = \{F_s\}_{updated} + k_s \cdot \Delta u_s \tag{3.21}$$

Using the Mohr-Coulomb model to represent the material behavior, the maximum shear bond force (F_s^{max}) is related to the normal force (F_n), the cohesion (c) and the friction angle (ϕ), as presented in equation (3.22).

$$F_s^{max} = F_n \cdot \tan(\phi) + c \cdot A_{int} \tag{3.22}$$

When the shear contact force is equal to maximum shear force ($F_s = F_s^{max}$) between two particles, shear rupture occurs. Therefore, the contact between those particles becomes only frictional. The maximum shear force in a purely frictional behavior is calculated according to equation (3.23).

$$F_s^{max} = F_n \cdot \tan(\phi) \tag{3.23}$$

3.1.3. Sample preparation

An important step when using the discrete element method is sample generation, to enable accurate simulation of real granular materials. For this step, there are two considerations: the definition of the model resolution (ratio of sample smallest dimension to average particle size) and the procedure to assemble the particles. Brugada et al. (2010) described some of the approaches commonly used in the literature for the assembly of granular arrangements. They are usually divided into two groups: dynamic and static. The dynamic category includes the methods that need a prior DEM simulation to generate the sample, while the static ones are usually based on geometric algorithms. This step is important for the DEM simulations as it has a considerable effect on the macroscopic results, as discussed in Ding et al. (2014). The authors noticed the reduction of the coefficients of variation (COVs) of the macro properties obtained by the DEM simulations with the increase on the model resolution. The COVs are assessed by comparing the results of 20 different particle assemblies. On the other hand, if model resolution is too high, more computational effort will be required. In addition, more challenges are faced when varying the size distribution of the particles, as explained in Berger and Hrenya (2014).

In order to assess the DEM microstructure obtained from sample generation, different techniques are compared in this work. Aiming at the study of rocks, only sample generation schemes applied to rocks are further discussed. One approach is pluviation of particles under gravity (Liu et al., 2008). In this case, particles are generated at a specific height and equilibrium under gravity load is established. Then, the bond between particles is added to all contacts. In another approach, particles are generated with smaller initial radii than the final ones. Particle radii are then increased to reach the final size, ensuring that particles do not overlap (Brugada et al., 2010). An alternative method for sample generation is multi-layer compaction (Jiang et al., 2003). In this approach, a layer is created by placing the particles inside a given volume. Then, the top wall moves down, compressing this layer. The top wall moves up and another group of particles is placed, repeating the previous procedure. Using a static approach, Lozano et al. (2016) present an algorithm developed to place sphere particles of different sizes in volumes of arbitrary shape generating dense arrangements.

3.1.4.
Calibration of DEM parameters

The DEM modeling approaches can be quite different. These differences are in the model initialization, model structure (clumps) or in the particle shapes. Each of these features can modify the results of the models. Besides that, the model parameters must be carefully chosen in order to accurately simulate the rock behavior.

3.1.4.1.
Ratio of compressive to tensile strength

The calibration procedure is important and complex during DEM modeling, as presented by Fakhimi and Villegas (2007). The authors presented some of the calibration problems, such as the difference between the ratio of compressive to tensile strength from the experimental and numerical simulations.

These problems are basically derived from the absence of grain interlocking in DEM (spherical particles), as discussed by Scholtès and Donzé (2013). To compensate this absence, some DEM parameters are over-estimated to better represent the material compressive strength experimentally observed. On the other hand, when subjecting this same material with over-estimated parameters to tensile tests, it presents a different behavior when compared to the laboratory results (Cho et al., 2007). To overcome this problem and be able to simulate the macroscopic behavior (in compressive and tensile tests), other features, such as particles with irregular shapes, must be added.

Some authors suggest different modeling techniques to overcome the problem of the incorrect ratio between compressive and tensile strengths. Cho et al. (2007) presented a strategy that considers clumped particles, as Figure 3-3. This approach is based on the assumption that each particle clump behaves as a material grain or mineral. Therefore, the bond connecting each particle of the same clump has a much higher strength than the classical particles, avoiding breaking. Thus, each clump can reproduce a different shape, helping to increase the grain interlocking value.

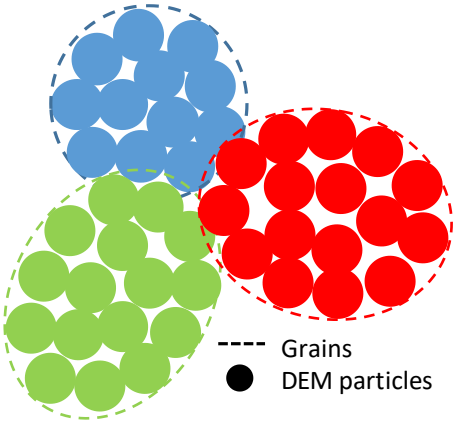

Figure 3-3 – Example of clumped model in DEM.

Also, Kazerani and Zhao (2010) modelled the sample with non-circular shape particles, changing model geometry, Figure 3-4. In this strategy, the geometry of the particles increases the grain interlocking and can represent the experimental results. On the other hand, this approach increases model complexity, due to the complex contact search and contact force laws.

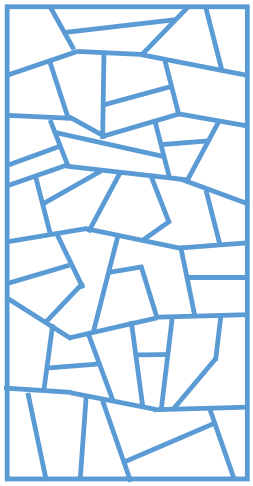

Figure 3-4 – Non-circular shape particles (based on Kazerani and Zhao (2010)).

Without altering the geometry of the particles, Scholtès and Donzé (2013) presented an alternative. The authors changed the coordination number of the model in order to keep each particle together with the highest number of particles possible (Figure 3-5). This procedure was carried out by defining an interaction range, which is used to bond neighboring particles that are not directly in contact. As this technique requires less computational effort, it is the one used in this thesis.

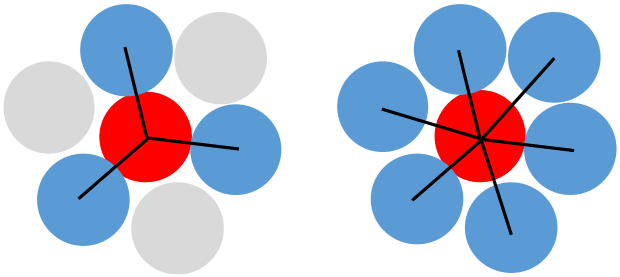

a) b)

Figure 3-5 – a) Without defining the interaction range and b) with the definition of the interaction range (based on Scholtès and Donzé (2013)).

3.1.4.2. Calibration techniques

Different calibration techniques are used when modeling with DEM. The most used approach is the trial and error method, in which several models with different values for the DEM parameters are carried out in order to match numerical and experimental results. This approach is very time consuming because it requires running a great number of models until the results agree with the laboratory measurements.

As an alternative, Yoon (2007) adopted the design of experiments (DOE) to calibrate the contact bonded model in the commercial software PFC. The first procedure was to assess the ranges of Young's Modulus, Poisson's ratio and Uniaxial Compressive Strength (UCS) for common rocks. Then a sensitivity analysis was performed to find the range of values from the model parameters that corresponded to the range of the macro-properties. The author used the Plackett-Burman design method to understand how the model parameters influenced the macroscopic responses. Then, the author selected two model parameters that had the highest impact and, with these, used a Central Composite design to run a response surface analysis and estimate the non-linear relation between the two most influential model parameters and the macroscopic results. After obtaining the relation between the model parameters and the macro properties, an optimization procedure was performed to calculate the model parameters that provided the smallest difference from the simulation results and the laboratory test. The authors have concluded that this calibration procedure achieves good results; however, when the values from the model parameters are close to the range limit, the results are no longer satisfactory.

Chehreghani et al. (2017) also used DOE for parameter calibration, using the response surface method. Using the bonded particle model from Potyondy and Cundall (2004), the authors simulated the uniaxial compressive test and calibrated the model parameters by

comparing the numerical with the laboratory results. In addition, this approach allowed investigating the influence of each model parameter in the macro response.

3.1.5. Chemical effects on mechanical parameters

In order to carry out a mechanical model, with rock dissolution, the chemical influence on mechanical parameters must be considered. Cha et al. (2016) studied the dissolution process in a quartzitic-carbonate sandy rock with 52% calcite and 47% quartz. The authors performed a laboratory experiment where a sample was subjected to an injection of an acetic acid solution. In addition, numerical models using the discrete element method were simulated. In those numerical analyses, the procedure adopted to simulate the dissolution process was to decrease the particle size over time at a constant rate. The authors compared the results of porosity from the laboratory with the ones from DEM, finding good agreement between them.

Another approach was implemented by Sun et al. (2017), who performed a micro-scratch test on Entrada sandstone samples. This same test was carried out using DEM. The authors first calibrated the unaltered Entrada sandstone. Next, the authors presented a DEM modeling of the micro-scratch test considering CO_2 altered and unaltered Entrada sandstone. To compute the influence of CO_2 over rock behavior, the authors reduced the bond radius between particles. A calibration procedure was performed using a uniaxial compressive test, and the model parameters found by the calibration were used in the micro-scratch test. The authors found good agreement between the calibrated micro-scratch model and the laboratory results. Then, the bond radii were reduced until good agreement between DEM and experimental tests was reached for the altered sandstone.

In Panthi and Lu (2014), a coupling technique was presented to consider the chemical effect together with the discrete element method. The authors examined the chemical dissolution effect on the soil weakening using a contact model with a degradation term. The procedure adopted by the authors consisted in changing normal and shear contact stiffness to account for chemical dissolution.

3.2. Workflow and results

For the DEM model, a workflow is presented in this section to accurately simulate rock behavior. First, the modified BPM contact model was implemented in the open source code *Yade*. Second, a sample preparation study was performed to select the best methodology for creating the DEM sample. Then, a parametric study was carried out to understand the effect of

each contact model parameter on the macro properties. The last step was to perform a calibration procedure to estimate the contact model parameters that represent the desired macro behavior observed in laboratory.

3.2.1. Modified BPM

As discussed in Wu and Xu (2016), there are three main problems when adopting the BPM cohesive contact model for rock simulation. The first problem is the low ratio unconfined compressive strength to tensile strength. To reach a more realistic ratio, Scholtès and Donzé (2013) proposed increasing the interaction range, which consequently raises the coordination number. Therefore, in the first time step, when the detection algorithm searches for particle contacts, particles can interact between each other even if they are not in contact. A parameter, called interaction range coefficient, defines the maximum distance between particles so the bonded interaction can exist. After this initial time step, this coefficient is set to one, which means that new interactions are created only when particles are in contact. The second problem of the standard BPM is the low internal friction angle, when compared to laboratory results. The internal friction angle can be increased by considering a pressure-dependent shear strength, as described in Wu and Xu (2016). The final issue of the BPM model is the linear strength envelope, where normally, intact rocks have nonlinear envelopes. To overcome the linear strength envelope, authors have adopted the clump strategy (explained in Section 3.1.4.1) in their simulations (Cho et al., 2007; Zhang et al., 2015).

In this study, the interaction range coefficient and the pressure-dependent shear strength were implemented in the standard BPM. The interaction range γ was added during the first step of contact search, creating interactions when $\gamma \cdot (R_A + R_B) > D$, where D is the distance between particles centers. This coefficient is always higher than 1.0, and must be chosen carefully according to the size distribution of particles (Scholtès and Donzé, 2013). The pressure dependent solution was added by changing the shear strength according to the normal forces, as presented in equation (3.24), where $\bar{\phi}$ is the friction angle from the bonded contact and $\bar{c}$ is the material cohesion.

$$\bar{\tau}_c = \frac{\bar{F}_n}{\bar{A}} \cdot \tan(\bar{\phi}) + \bar{c} \tag{3.24}$$

In addition, a term suggested in Potyondy (2011) was added in order to change the effect of torsion and bending moments on bond integrity. Therefore, β was added in equation (3.18), as presented in equation (3.25).

$$\bar{\sigma}^{\max} = -\frac{\bar{F}_n}{\bar{A}} + \beta \cdot \frac{|\bar{M}_s| \cdot \bar{R}}{\bar{I}} < \overline{\sigma_C}$$
$$\bar{\tau}^{\max} = \frac{|\bar{F}_s|}{\bar{A}} + \beta \cdot \frac{|\bar{M}_n| \cdot \bar{R}}{\bar{J}} < \overline{\tau_C} \quad (3.25)$$

3.2.2. Sample preparation

In this work, three sample generation procedures were applied and compared: i) the static approach (using Packgen algorithm), as presented by Lozano et al. (2016); ii) a combination between the static and the pluviation of particles; and iii) a combination of the static and the multi-layer compaction. In this case, instead of compacting each layer individually, the procedure consists on compacting the entire sample at once. For comparison, ten realizations were generated for all three methods. These ten realizations were subjected to uniaxial compressive tests (UCT) and the coefficients of variation (COVs) for the macroscopic results (Young's modulus, uniaxial compressive strength and Poisson's ratio) were compared. Among the three procedures to generate the sample, the one combining the static approach and the compaction showed lower COVs for the macroscopic properties when considering all ten realizations, with COVs lower than 2 %. Therefore, this procedure was the one adopted for all the following studies.

A representative scheme for the method that delivered the best results, which is the combination of Packgen and compaction is presented in Figure 3-6.

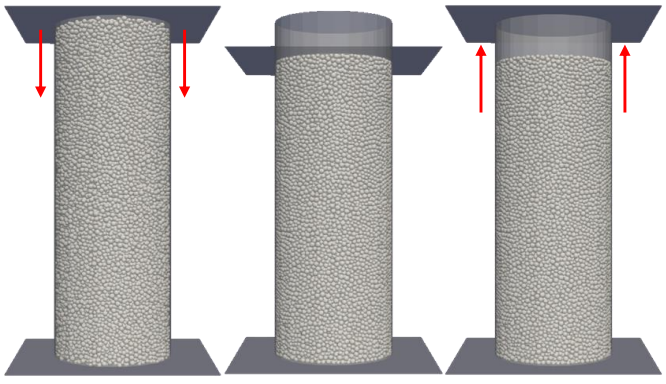

a) b) c)

Figure 3-6 – Sample generation scheme using the technique combining Packgen and compaction.

In addition to sample assembly, a proper model resolution for the uniaxial compressive test needed to be defined. For that, two different model resolutions (the ratio of sample smallest dimension to average particle size) were compared: 10.50 and 26.25. Ten realizations were performed considering these two model resolutions, and they were all subjected to uniaxial

compressive test simulations. The COVs from the macroscopic parameters (Young's modulus, uniaxial compressive strength and Poisson's ratio) were assessed in order to choose the best resolution. The results showed that the model resolution of 26.25 presented lower COVs (lower than 2 %) for all the properties. Therefore, a model resolution around 26.25 (average particle radii of 0.8 mm in a sample with 21 mm in radius and 84 mm in height) must be considered when carrying out uniaxial compressive tests. Detailed results considering the uniaxial compressive tests for the model resolution and for the particle assembly are summarized in a paper entitled "The influence of sample generation and model resolution on mechanical properties obtained from DEM simulations", which is under submission process.

A study regarding the definition of a proper model resolution is carried out in this section for the Brazilian splitting test. Here, samples were built with particles of different sizes. The effect of model resolution was investigated by adopting average particle radii of 0.4 mm (BS04), 0.6 mm (BS06) and 0.8 mm (BS08) with $d_{max}/d_{min} = 1.67$, where d_{max} is the particles maximum diameter and d_{min} is the particle minimum diameter. All samples in this study had 42 mm in diameter and 19 mm in thickness. The cohesive contact model adopted for this comparison is the Jointed Cohesive Frictional, with the adopted DEM parameters presented in Table 3-1. The timestep adopted is 10^{-8}, with a plate velocity of 0.007 m/s, meaning that to achieve a displacement of 1.0 mm, it requires more than 14,000,000 steps. For the Brazilian splitting test simulation, facets were used to compress the sample diametrically, as shown in Figure 3-7.

Table 3-1 – DEM parameters used in the simulations for the comparison among the sample generation methods.

Contact parameters	Y (GPa)	55.00
	$micro\_\nu$	0.60
	ϕ (radians)	0.44
	c (MPa)	20.00
	t (MPa)	28.00
DEM parameters	Numerical damping	0.4
	Gravity (m/s²)	10.0
	Enlarge Factor	1.5

For the Brazilian test, Table 3-2 presents the information about the samples for each model resolution.

Table 3-2 – DEM input parameters and number of realizations from the sample generation study.

Sample Number	Model resolution	Particle average radii (mm)	r_{max} / r_{min}	Number of Realizations
BS04	23.75	0.4	1.67	10
BS06	15.83	0.6	1.67	10
BS08	11.88	0.8	1.67	10

Table 3-3 presents the average, the standard deviation, and the coefficient of variation (COV) for the geometric parameters and Brazilian Tensile Strength (BTS) for samples BS04. For the geometric parameters, the COVs were less than 1%, while for the BTS, it was around 3.5 %.

Table 3-3 – DEM geometric parameters and tensile strength for sample BS04.

	Void ratio	Porosity	Number of Particles	Coord. Number	BTS
Average	0.636	0.389	62462	14.298	10.10 MPa
Stand Dev.	0.0051	0.0019	108	0.011	0.371 MPa
COV	0.800 %	0.491 %	0.173 %	0.079 %	3.677 %

Table 3-4 presents the average, the standard deviation, and the COVs for void ratio, porosity, number of particles, coordination number, and Brazilian tensile strength for samples BS06. The COVs for the geometric parameters were lower than 1.2 %, while the COV for the tensile strength was around 6.5 %.

Table 3-4 – DEM geometric parameters and tensile strength for sample BS06.

	Void ratio	Porosity	Number of Particles	Coord. Number	BTS
Average	0.679	0.404	18312	13.957	11.57 MPa
Stand Dev.	0.0079	0.0028	57	0.009	0.751 MPa
COV	1.156 %	0.684 %	0.308 %	0.066 %	6.493 %

Table 3-5 presents the same geometric parameters and the BTS for samples BS08. The geometric parameters had COVs lower than 1.3 %, while for the indirect tensile strength, COV was 9.3 %.

Table 3-5 – DEM geometric parameters and tensile strength results for sample BS08.

	Void ratio	Porosity	Number of Particles	Coord. Number	BTS
Average	0.730	0.422	7678	13.611	12.12 MPa
Stand Dev.	0.0093	0.0031	49	0.022	1.131 MPa
COV	1.268 %	0.734 %	0.638 %	0.162 %	9.327 %

Initially, the same average particle radii (0.8 mm) from the Uniaxial Compressive Test (UCT) study was used in the Brazilian Splitting Test (BST). By assessing the results from 10 realizations, high COVs (around 10 %) were observed. Therefore, models with two other resolutions with average particle radii of 0.4 mm and 0.6 mm were developed. A difference between the results from the UCT and BST variations using average particle radii of 0.8 mm was observed. In UCT, the COVs were around 2%, while in BST, those values were close to 10 %. This difference in the mechanical properties was mainly due to the contact between the plates and particles. In UCT, more particles were in contact with the plate, which helps to maintain similar behavior among realizations. On the other hand, for BTS, a small number of particles was in contact with the plate. Hence, any change in particle distribution have a higher effect on sample behavior. It is worth mentioning that even if the average particle size of the BST and UCT was the same, model resolution was not. For UCT, the smallest dimension was the diameter, while for the BST, it was the thickness, and in both cases, the plate was in contact with the smallest dimension. Therefore, the sample with average particle radii of 0.8 mm had a model resolution of 15.83 for the BST, while for UCT sample, it was 26.25.

The BST results obtained in this work after creating ten realizations for each model resolution described a similar trend as the results from the UCT. As model resolution increased, the COV of tensile strength decreased. The COV of the Brazilian tensile strength for average particle radii of 0.4 mm (resolution of 23.75) was around 3.5 %. In comparison, for radii of 0.6 mm (resolution of 15.83) COV was close to 6.5 %, and for 0.8 mm (resolution of 11.88), it was almost 9.5 %. Therefore, in this case, samples with a model resolution of 23.75 and 15.83 were almost independent on particle distribution, while samples with a resolution of 11.88 were still very dependent on particle assembly.

Figure 3-7 presents a comparison between the three model resolutions used for the Brazilian splitting test. The difference in particle sizes among these three samples is clear. This comparison makes it easier to assess the number of particles in contact with the top and bottom plates.

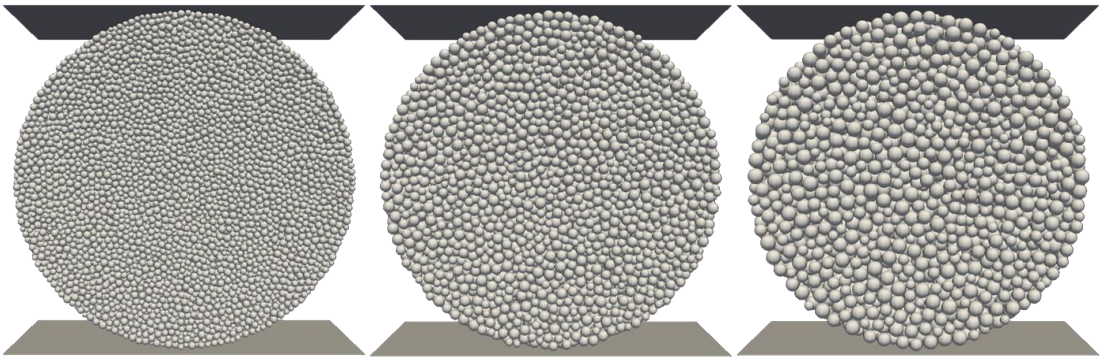

a) b) c)

Figure 3-7 – DEM Sample structure for the Brazilian splitting test with model resolution of a) 23.75, b) 15.83 and c) 11.88.

During this study, it was observed that the results obtained for these 10 realizations for the Brazilian Splitting test showed a high variability. Hence, in Section 5, a direct tensile test was modelled for comparison with the laboratory results from the Brazilian Splitting test. The indirect tensile strength obtained from the Brazilian Splitting test are not necessarily the same obtained from the direct tensile test (Li and Wong, 2013), but it can be an estimative of the magnitude order of the material tensile strength. In this work, the indirect tensile strength obtained in the laboratory is used only as an estimative for the tensile strength when calibrating the DEM parameters.

3.2.3. Parametric study for the modified BPM contact model

To better understand the influence of each modified BPM contact model parameter, a parametric study was performed in this section. Therefore, for each parameter, three models were run to investigate their influence on the simulation result. The model adopted in this section was a cylinder with 54 mm in diameter and 108 mm in height. The default parameters for the contact model adopted in this parametric study are presented in Table 3-6, while sample structure and simulation parameters are in Table 3-7.

Table 3-6 – The default parameters used in the DEM parametric study.

$\bar{\lambda}$	E (GPa)	$\bar{E}$ (GPa)	ν	$\bar{\nu}$	ϕ (degrees)	$\bar{\phi}$ (degrees)	$\overline{\sigma_C}$ (MPa)	$\overline{\tau_C}$ (MPa)
1.0	5.0	12.0	2.0	1.85	85.0	15.0	2.0	5.2

Table 3-7 – Sample structure and simulation parameters used in the DEM parametric study.

R_{max} (mm)	R_{min} (mm)	Numerical damping	Gravity (m/s^2)	Enlarge Factor	Number of particles
1.0	0.6	0.4	10.0	1.5	70,848

Here, E, ν and ϕ are the DEM Young's modulus, DEM Poisson's ratio and DEM friction angle, respectively, while the parameters with $\overline{[x]}$ represent the bonded parameters. The names of these parameters are set according to their influence on the properties which they are named after.

The first parameter studied here is the non-bonded Young's modulus (E) and the second one is the bonded Young's modulus ($\bar{E}$). These parameters depend on the normal stiffness (k_n) and on the bonded normal stiffness ($\overline{k_n}$), respectively. The non-bonded Young's modulus is evaluated from the normal stiffness and particle radii according to equation (3.26).

$$\begin{aligned} k_{nA} &= E_A \cdot 4 \cdot R_A \\ k_{nB} &= E_B \cdot 4 \cdot R_B \\ k_n &= \frac{2 \cdot k_{nA} \cdot k_{nB}}{k_{nA} + k_{nB}} \end{aligned} \tag{3.26}$$

Here, A and B are the reference to the two particles in contact. The same calculations are required for the bonded Young's modulus ($\bar{E}$), as presented in equation (3.27).

$$\begin{aligned} \overline{k_{nA}} &= \frac{\overline{E_A}}{2 \cdot R_A} \\ \overline{k_{nB}} &= \frac{\overline{E_B}}{2 \cdot R_B} \\ \overline{k_n} &= \frac{2 \cdot \overline{k_{nA}} \cdot \overline{k_{nB}}}{\overline{k_{nA}} + \overline{k_{nB}}} \end{aligned} \tag{3.27}$$

In this parametric study, the values for E were 3.5 GPa, 5.0 GPa and 6.5 GPa, and the results for this comparison is presented in Figure 3-8. From the results obtained here, the parameter E changed the material elastic modulus (from 28.8 GPa to 33.3 GPa), the peak axial stress (34.7 MPa to 37 MPa) and also Poisson's ratio (from 0.131 to 0.140). When increasing E, the material elastic modulus, the peak axial stress and Poisson's ratio also increased.

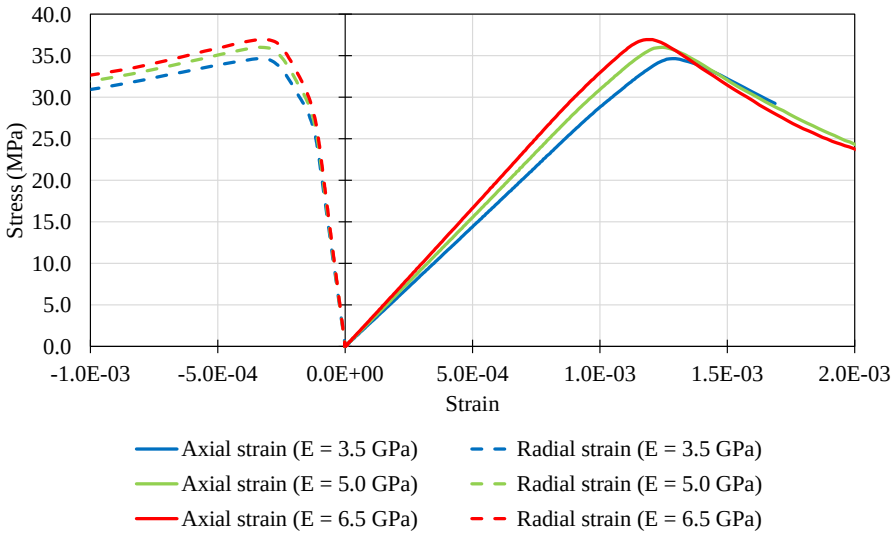

Figure 3-8 – Axial and radial strains after changing the non-bonded Young's modulus parameter in a parametric study considering the uniaxial compressive test in DEM.

For $\bar{E}$, the values adopted were 10.5 GPa, 12 GPa and 13.5 GPa, and the results are presented in Figure 3-9. It is possible to note a great influence on the material elastic modulus (from 28.1 GPa to 34.0 GPa), but a very small change on the peak axial stress (36.6 MPa to 35.5 MPa) and on Poisson's ratio (from 0.137 to 0.134). As $\bar{E}$ increased, the material elastic modulus also increased.

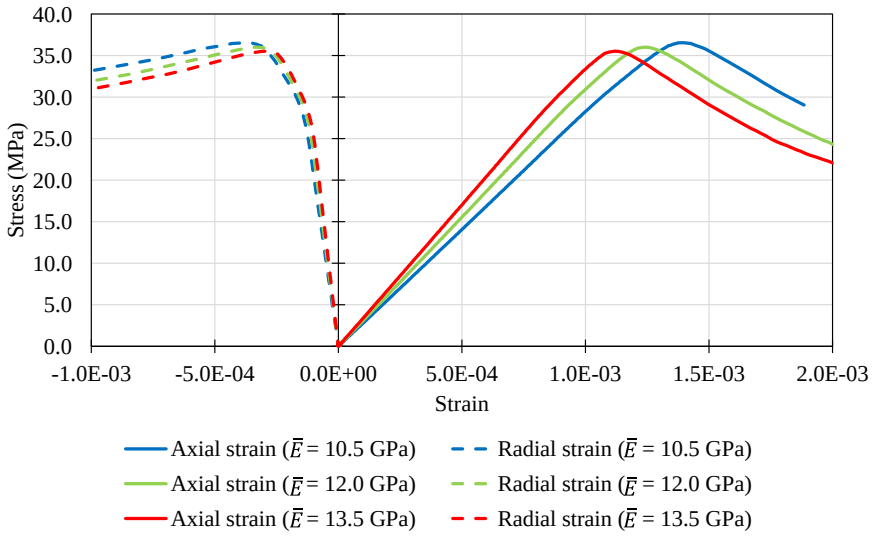

Figure 3-9 – Axial and radial strains after changing the bonded Young's modulus parameter in a parametric study considering the uniaxial compressive test in DEM.

Following, the non-bonded Poisson's ratio (ν) and the bonded Poisson's ratio ($\bar{\nu}$) were analyzed. From k_n (previously calculated) and ν, the BPM algorithm evaluates the shear stiffness (k_s).

$$k_{sA} = \frac{k_{nA}}{\nu_A}$$
$$k_{sB} = \frac{k_{nB}}{\nu_B} \tag{3.28}$$
$$k_s = \frac{2 \cdot k_{sA} \cdot k_{sB}}{k_{sA} + k_{sB}}$$

Equation (3.28) describes these calculations for the non-bonded contacts and equation (3.29) for the bonded contact.

$$\overline{k_{sA}} = \frac{\overline{k_{nA}}}{\overline{\nu_A}}$$
$$\overline{k_{sB}} = \frac{\overline{k_{nB}}}{\overline{\nu_B}} \tag{3.29}$$
$$\overline{k_s} = \frac{2 \cdot \overline{k_{sA}} \cdot \overline{k_{sB}}}{\overline{k_{sA}} + \overline{k_{sB}}}$$

Here, ν was considered as 1.5, 2.0 and 2.5. The comparison among these three simulations is presented in Figure 3-10. There was a small variation on the material elastic modulus (from 31.9 GPa to 30.6 GPa), Poisson's ratio (from 0.125 to 0.142) and peak axial stress (from 37.9 MPa to 34.7 MPa). Higher values of ν reduced the peak axial stress and the material elastic modulus, while increased the material Poisson's ratio.

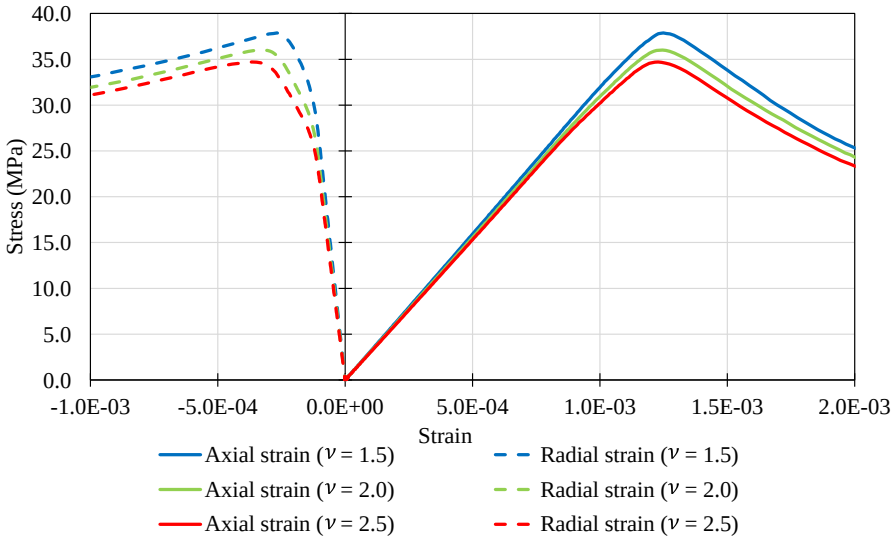

Figure 3-10 – Axial and radial strains after changing the non-bonded Poisson's ratio parameter in a parametric study considering the uniaxial compressive test in DEM.

The values of 1.35, 1.85 and 2.35 were adopted for the bonded Poisson's ratio ($\bar{\nu}$) with the results shown in Figure 3-11. This parameter affected the post peak behavior, and also changed the trend from the axial strain and radial strain curves. When using higher values, for

example, 2.35, the curve inclination changed between 20.0 and 25.0 MPa of axial stress. In addition, this parameter influences the material elastic modulus (from 33.9 GPa to 29.4 GPa), Poisson's ratio (from 0.098 to 0.159) and leads to small changes to UCS (from 35.2 MPa to 35.3 MPa).

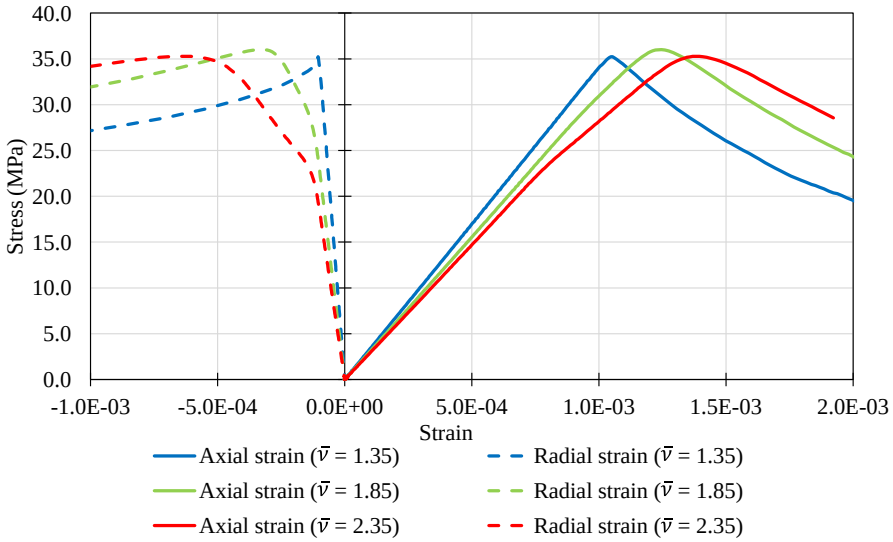

Figure 3-11 – Axial and radial strains after changing the bonded Poisson's coefficient parameter in a parametric study considering the uniaxial compressive test in DEM.

The values adopted for ϕ were 65°, 75° and 85°, and the results are presented in Figure 3-12. This parameter had no effect on the material elastic modulus, which was constant at 31.1 GPa. The material UCS and Poisson's ratio presented small variations, from 35.4 MPa to 36.0 MPa and from 0.137 to 0.135, respectively. Only a slight change on the post-peak behavior was noted. From other tests, especially when applying a confining pressure, it was observed that higher values of ϕ produced higher change on the post-peak behavior.

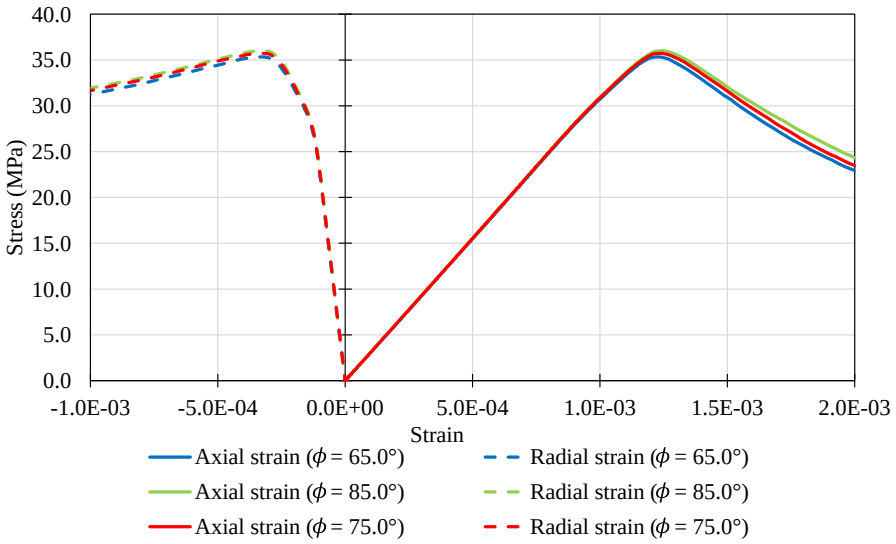

Figure 3-12 – Axial and radial strains after changing the non-bonded friction angle parameter in a parametric study considering the uniaxial compressive test in DEM.

Here, the values of $\bar{\phi}$ used were 10.0°, 15.0° and 20.0°, and the comparison is presented in Figure 3-13, showing a great influence on the peak axial stress. When increasing $\bar{\phi}$, the peak axial stress also increased from 33.9 MPa to 37.7 MPa, while the elastic modulus and Poisson's ratio maintained at 31.1 GPa and 0.135.

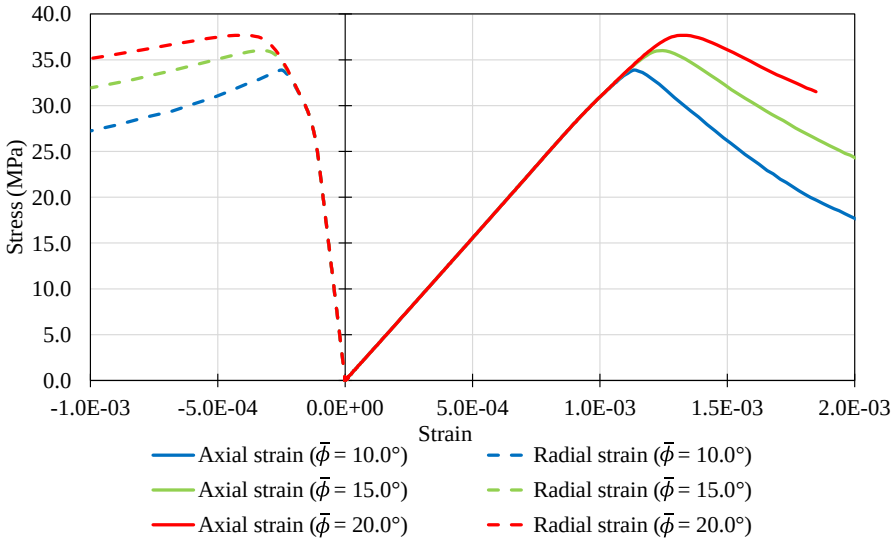

Figure 3-13 – Axial and radial strains after changing the bonded friction angle parameter in a parametric study considering the uniaxial compressive test in DEM.

The strength parameters were also evaluated in this parametric study. The values used for the tensile strength $\overline{\sigma_c}$ were 1.5 MPa, 2.0 MPa and 2.5 MPa and the results are in Figure 3-14. This parameter had influence on the peak axial stress and on the trend of the axial strain and radial strain curves. When increasing the tensile strength from 1.5 to 2.5 MPa, the peak axial stress also increased from 33.6 MPa to 38.8 MPa, and no variation was observed for the

elastic modulus and Poisson's ratio. In addition, increasing $\overline{\sigma_C}$, or setting it closer to the shear strength ($\overline{\tau_C}$) reduced the change on the axial curve and radial curve inclinations. The curve inclinations were affected by the tensile and shear breaks occurring on each contact between particles. The moment in which the curve trend changes was when the tensile breaks were higher. Then, the breaks due to shear increased fast, until rupture. When the ratio between shear and tensile strengths is close to 1.0, the curve follows the same pattern (elastic modulus) until rupture. As this ratio ($\overline{\sigma_C}/\overline{\tau_C}$) increases, the curve inclination changes under smaller strains.

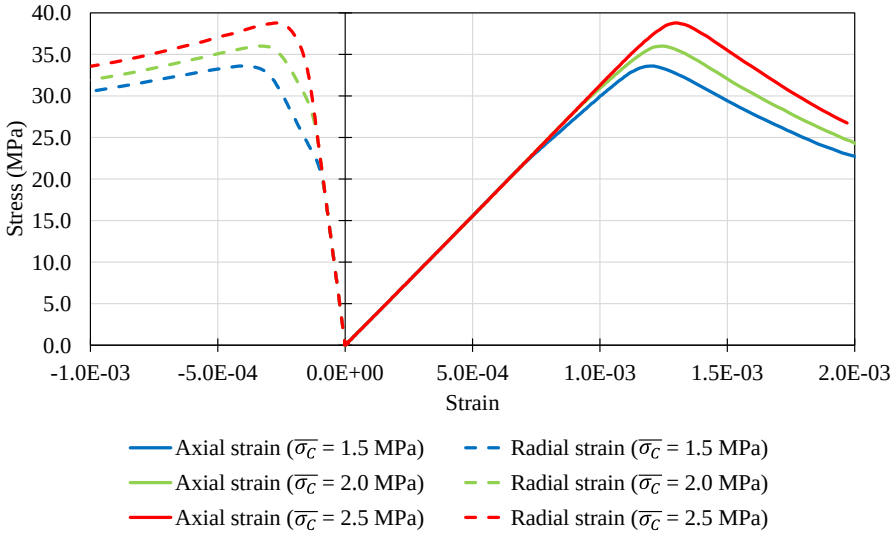

Figure 3-14 – Axial and radial strains after changing the tensile strength parameter in a parametric study considering the uniaxial compressive test in DEM.

The other strength parameter is the shear strength $\overline{\tau_C}$, which was considered with 4.7 MPa, 5.2 MPa and 5.7 MPa. The comparison for the shear strength is presented in Figure 3-15, showing that this parameter only affected the peak axial stress, changing it from 33.6 MPa to 38.5 MPa. High values of shear strength produced high peak axial stresses.

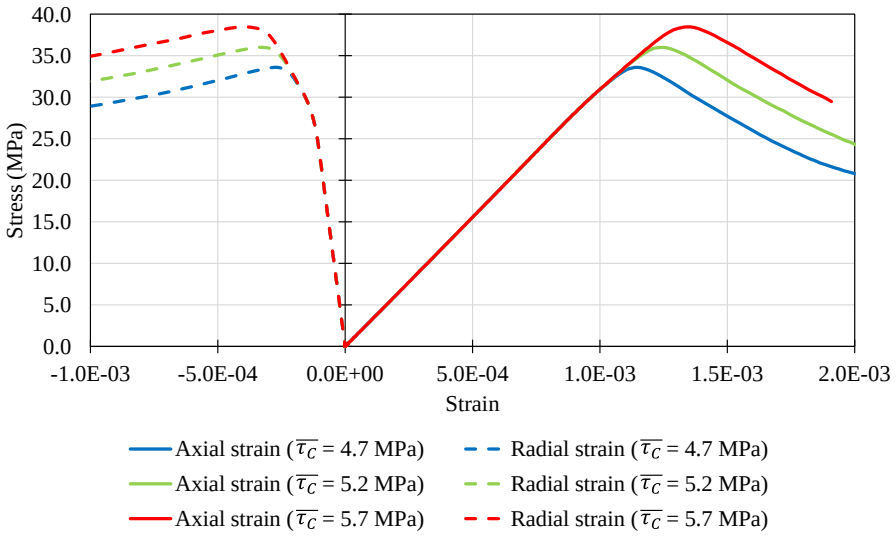

Figure 3-15 – Axial and radial strains after changing the shear strength parameter in a parametric study considering the uniaxial compressive test in DEM.

Regarding the influence of the dissolution on the material mechanical properties, a similar approach from Sun et al. (2017) was adopted in this thesis, but using the BPM contact model. The change on the mechanical properties due to CO_2 dissolution was considered by altering the bond radius coefficient, $\bar{\lambda}$. This coefficient defines the diameter of the cohesive beam that connects two particles. Changing this parameter is similar to changing the size (radius) of the bond in the material. From a parametric study performed with the modified BPM considering $\bar{\lambda}$ = 0.8, 0.9 and 1.0 in Figure 3-16, changes on the UCS, E and Poisson's ratio from 29.4 MPa to 36.0 MPa, 26.6 GPa to 31.1 GPa and 0.139 to 0.135, respectively, was observed. The results are in agreement with other works in the literature, such as Marbler et al. (2013), who observed a reduction on the rock strength, when testing rock samples altered by CO_2 and unaltered.

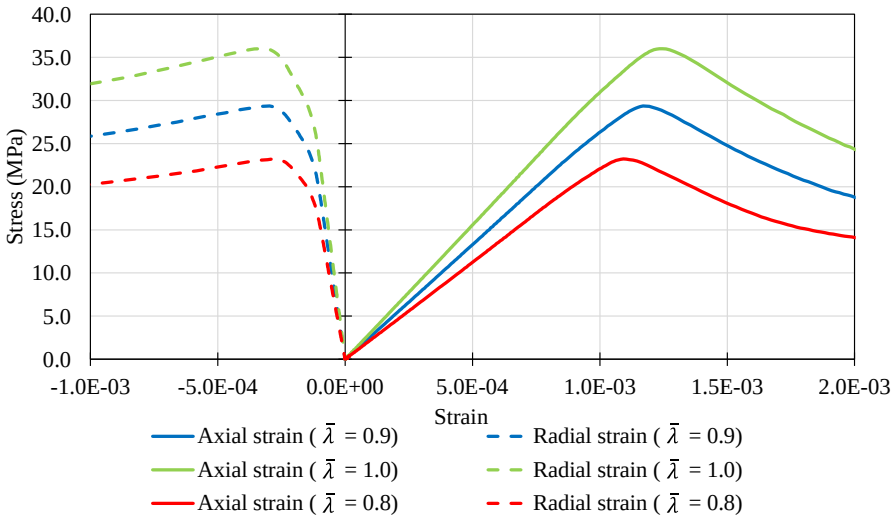

Figure 3-16 – Axial strain and radial strain curves after changing $\bar{\lambda}$ parameter in a parametric study considering the uniaxial compressive test in DEM.

From Figure 3-16, the values of E and UCS decreased considerably when $\bar{\lambda}$ decreased. The next step of this work is to validate this model by performing laboratory tests on carbonate rocks and comparing their results with the DEM models.

3.2.4. Parameter calibration

In addition to a proper sample generation, DEM modeling requires calibration of the model parameters. In this section, a procedure that combines genetic programming (GP) and optimization with internal points is proposed for parameter calibration. GP is a valuable tool to establish relationships between data points. GP is based on natural genetic operations (crossover, mutation and reproduction), following the Darwinian principle of reproduction and survival (Koza, 1994). According to Koolivand-Salooki et al. (2017), this method needs fewer data than other artificial intelligence methods. For comparison, this section also brings the calibration of rocks using Design of Experiments combined with optimization, as in (Yoon, 2007) and Deng et al. (2017).

In GP, firstly, a population of individuals is randomly generated. Each individual is represented by a tree, which consists of two kinds of nodes. Figure 3-17 presents an example of an individual computer program. The first group of nodes is based on primitive functions (arithmetic operations, mathematical functions), while the second group are the terminal nodes (input values and numerical constants).

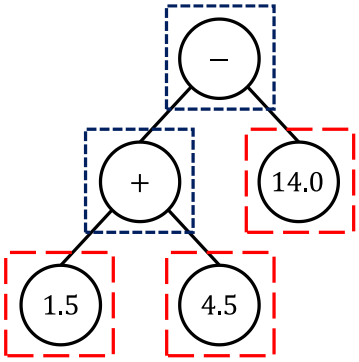

Figure 3-17 – Individual computer program with primitive nodes (blue) and terminal nodes (red) used in the Genetic Programming (based on De Simone et al. (2019)).

Each individual computer program from the first generation is assessed, and its output is compared with the correct result. This difference is the error of this particular individual. Therefore, the computer programs with smallest errors are selected for further analysis. In this step, reproduction and crossover procedures are carried out over the current generation. The reproduction procedure follows by selecting the best fit (with smallest error) individuals and copying them to the next generation. On the other hand, the crossover allows the random combination of two individuals from the previous generation (parental individuals) in order to create new individuals for the next generation.

This procedure goes on for several generations. The GP output is the individual computer program that has the best fit among all generations. The objective of GP in this work is to obtain functions for material properties with the DEM parameters as inputs.

To perform the DEM calibration using GP, a workflow presented in Figure 3-18 was followed. First, the lower and upper bounds were set for each DEM parameter (called microparameter in the workflow). Then, several DEM models were generated with random sets of parameters inside these pre-defined bounds. These DEM models were subjected to a uniaxial compressive test, and the macro properties (uniaxial compressive strength - UCS and Young's modulus - E) were obtained for each set of DEM parameter. These results were input for the GP analysis, which related the DEM parameters with the macro properties (UCS and E). Then, an optimization step was performed to define the set of model parameters to reach the desired macro properties. For comparison, this study was carried out considering two number of DEM parameter sets: 30 and 100.

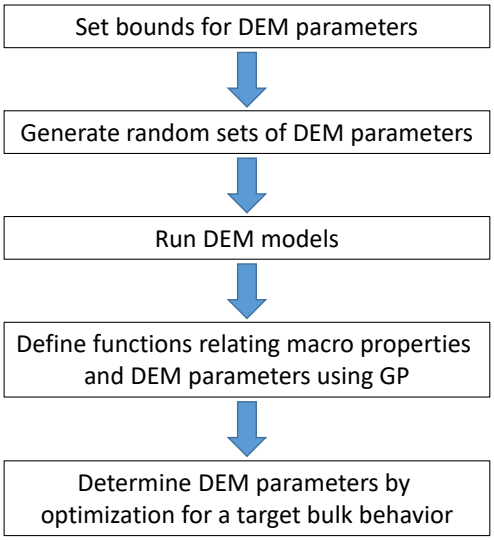

Figure 3-18 – Workflow used for the calibration using the genetic programming procedure (based on De Simone et al. (2019)).

To validate this procedure, the accuracy of the GP calibration was tested. From a target value of UCS and Young's modulus, the DEM parameters were obtained using the workflow in Figure 3-18. Using these model parameters obtained from the optimization, a uniaxial compressive test was simulated in DEM, and the obtained macro properties (UCS and E) were compared with the target ones. This comparison was carried out for six target values considering 30 and 100 data sets.

The results obtained considering both data sets (30 data sets and 100 data sets) showed very good results. The errors when comparing the macro properties obtained from the DEM simulations with the target properties were low, except when considering parameter values close to the pre-defined bounds (first step on the workflow from Figure 3-18). As expected, the errors from the 100 data sets were lower than the 30 data sets. On the other hand, the computational effort is much higher for the 100 data sets. Therefore, it was possible to reach a good tradeoff between low error and computational costs with the 30 data sets calibration using genetic programming. The detailed procedure and results for this calibration study using GP and DOE are described in De Simone et al. (2019).

4
Laboratory tests

Laboratory tests were important in this study in order to calibrate and validate numerical models, while giving more insight to the studied problems. There were two groups of tests carried out in this thesis: characterization tests, which were purely mechanical and coupled tests, where CO_2 was injected through the rock. The tests were conducted on two carbonate rocks: Indiana Limestone and coquinas from the Morro do Chaves.

Various mechanical tests were performed with different objectives in this study. Uniaxial, single triaxial and Brazilian splitting tests were performed to characterize the Indiana Limestone rock used here, and the results from these tests were used to validate the modified BPM implemented in *Yade*. Multi-stage triaxial tests were used to characterize the material before and after CO_2 injection tests. In addition, the peak deviator stress for each stage and Young's modulus and Poisson's ratio from the first stage were used to calibrate the DEM model. Figure 4-1 presents the proposed laboratory workflow for Indiana Limestone samples and Figure 4-2 the workflow for coquina samples.

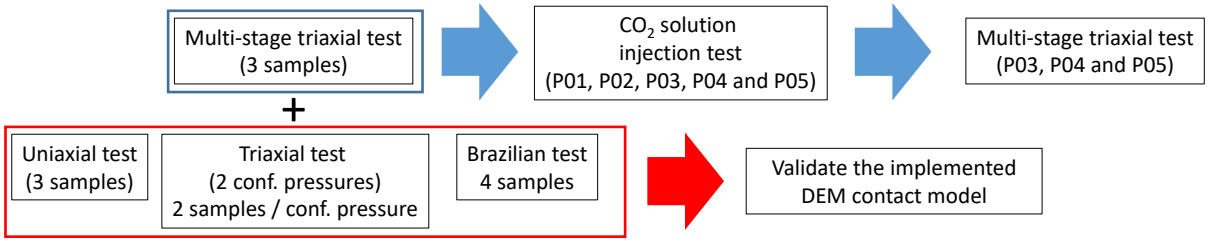

Figure 4-1 – Workflow for the tests performed on Indiana Limestone samples in this thesis.

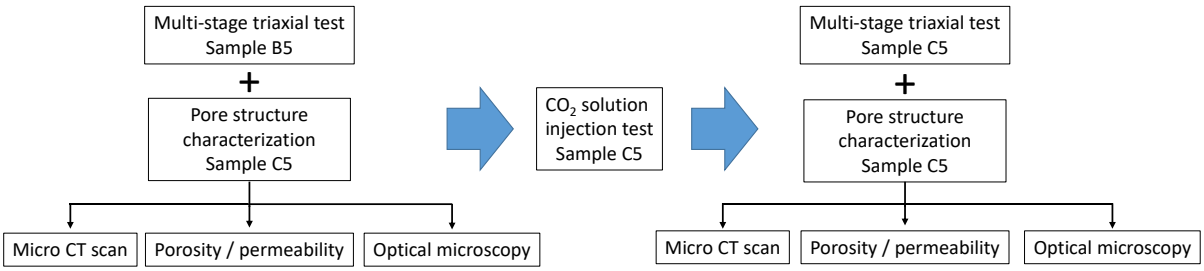

Figure 4-2 – Workflow for the tests performed on coquina samples in this thesis.

4.1. Indiana Limestone

Laboratory tests were carried out using Indiana Limestone samples acquired from Kocurek Industries, USA. Information on porosity and permeability were provided by the supplier, with permeability between 2 and 9 mD and sample porosity of 19%. The choice of this material was due to its characteristics, as it is generally considered a more homogeneous carbonate rock. The experimental results were used for calibration and validation of the numerical models, as it will be presented further.

Two sets of samples were obtained, one with diameter of 42 mm and height of 84 mm, and a second with diameter of 54 mm and height of 108 mm, maintaining the diameter to height ratio of 2.0. For the dissolution tests, because of the size of the test set-up available for the injection tests, 54 mm-diameter plugs had their dimensions altered to 50 mm diameter and 100 mm height. Table 4-1 presents a summary with the size of the samples used in each test.

Table 4-1 – Size of Indiana Limestone samples used for each laboratory test.

Plug diameter	Performed tests	Aims
42 mm	Single triaxial tests	Calibration and validation of DEM implementations
50 mm	CO_2 injection test and Multi-stage triaxial test after CO_2 injection	Observing injection effects on porosity and mechanical properties Providing data for DEM model
54 mm	Multi-stage triaxial test on intact samples and Brazilian splitting test	Establishing intact mechanical properties and calibration and validation of DEM implementations

4.1.1. Methods

4.1.1.1. Mechanical characterization

Triaxial compressive tests

Initially, triaxial compressive tests were performed on Indiana Limestone samples using a GCTS triaxial system model RTX-1500 (Figure 4-3a), without confining pressure (uniaxial test) and under confining pressures of 2 and 5 MPa. The confining pressures were applied with a rate of 0.5 MPa / min while a radial strain rate of 0.007 %/min was set for the axial stress loading. Throughout this thesis, the uniaxial and triaxial compressive tests were performed considering a load rate controlled by radial strain. The radial strain control allows a slow test when approaching the peak stress, which enables a better monitoring of the post-peak behavior.

The plugs had 42 mm in diameter and 84 mm in height and two replicates per condition were evaluated, with the exception of the uniaxial tests, where three replicates were tested. For these tests, two LVDTs (linear variable differential transducers) positioned diametrically opposed recorded the axial strain, while one LVDT recorded the radial strain (highlighted in red in Figure 4-3b). The setup is presented in Figure 4-3b.

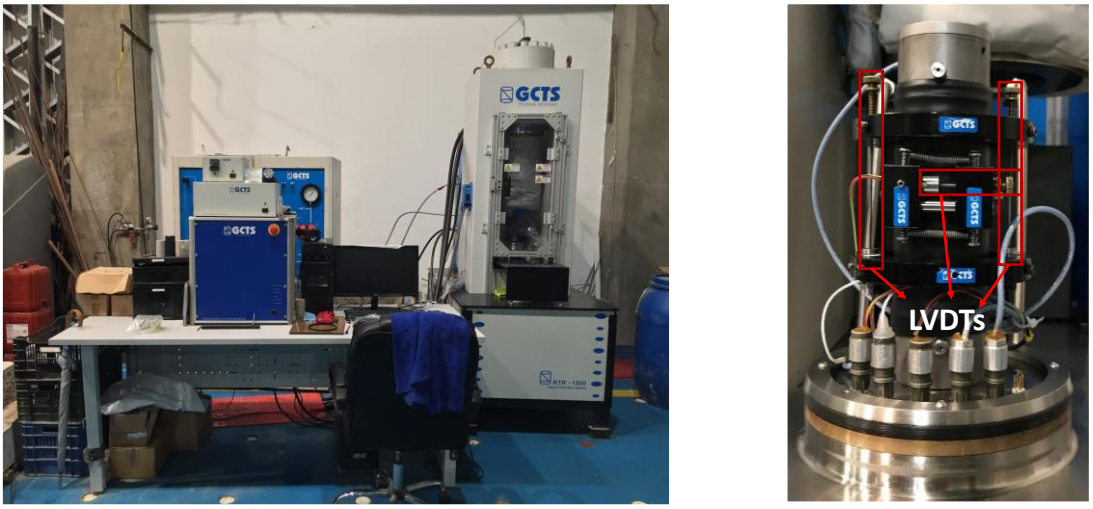

a) b)

Figure 4-3 – a) GCTS triaxial system used for the uniaxial and triaxial compressive tests performed on Indiana Limestone samples with 42 mm in diameter and b) Indiana Limestone 42 mm sample prepared for the triaxial compressive test in the GCTS triaxial system.

Multi-stage triaxial compressive tests

Due to the small number of samples available for this study, multi-stage triaxial compressive tests (ISRM, 1983) were performed to mechanically characterize the Indiana Limestone samples. These tests were carried out in order to compare the material mechanical properties before and after dissolution. Pre-dissolution mechanical characterization tests were performed on plugs with 54 mm in diameter and 108 mm in height. For reliability purposes, three samples were tested. This size was selected due to the fact that the GCTS creep system only allows tests with samples with diameters of 25 mm, 38 mm and 50 mm. Therefore, the dissolution tests and post-dissolution mechanical characterization tests were carried out on plugs with diameter of 50 mm and 100 mm in height.

There are several procedures for the multi-stage triaxial test, as presented in Aghababaei et al. (2019). First, there is the method initially suggested by ISRM (1983), where the axial stress is continually increased, as confining pressure increases. Aghababaei et al. (2019) on the other hand, presented a modified version, where after each deviator stress loading step, there

is also an unloading one. The authors also mentioned different criteria for determining the imminent failure point, before starting the unloading step, such as, deviator stress - axial strain, deviator stress - radial strain, deviator stress - volumetric strain or secant Young's modulus - axial strain curves. Among these possible criteria, the one considering the deviator stress - radial strain curve, developed by Youn and Tonon (2010) presented similar results when compared to single triaxial compressive tests. These tests were carried out using radial strain control to apply deviator stress, as brittle rocks tend to fragment more suddenly. Therefore, in this thesis, the multi-stage triaxial compressive test was carried out using the modified version, with radial strain control, and determining the imminent failure point by the deviator stress - radial strain curve, in order to damage the material as little as possible during each loading step.

These multi-stage triaxial tests were performed in an MTS triaxial system model 815 Rock System (Figure 4-4). During the test, three confining pressures were applied 0.0, 2.0 and 5.0 MPa. The adopted procedure is described below, and a representative curve is presented in Figure 4-5:

- Start applying the deviator load (axial load in this stage) with a radial strain rate of 0.006 mm/min until near rupture (close to horizontal curve on the axial stress - radial strain plot);
- Unload the deviator load to a value of 2.0 kN (to ensure the piston is still in contact with the sample) with a radial strain rate of 0.006 mm/min;
- The confining pressure of 2.0 MPa is applied with a loading rate of 0.5 MPa/min;
- Apply the deviator load with a radial strain rate of 0.006 mm/min until near rupture (close to horizontal curve on the axial stress - radial strain plot);
- Unload the deviator load to a value of 2.0 kN with a radial strain rate of 0.006 mm/min;
- Apply a confining pressure of 5.0 MPa with a loading rate of 0.5 MPa/min;
- Apply the deviator load with a radial strain rate of 0.006 mm/min until rupture.

Figure 4-4 – MTS triaxial system used for the multi-stage triaxial compressive tests.

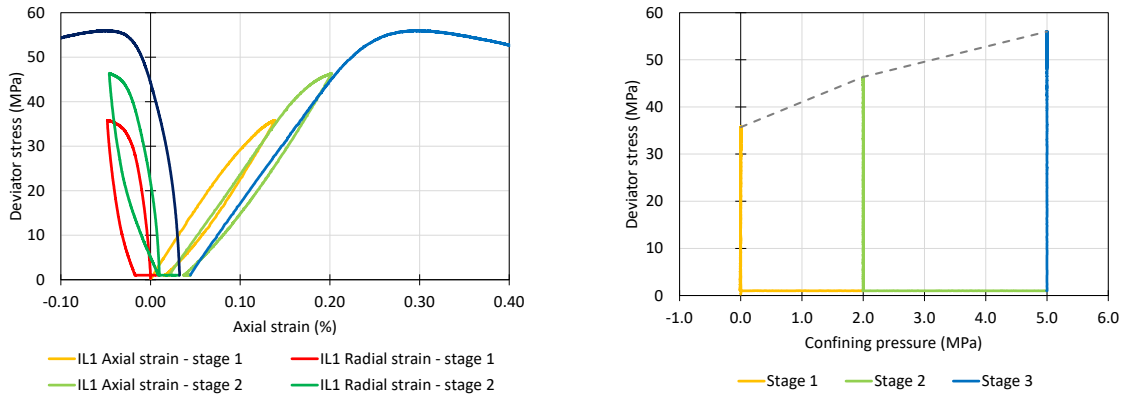

a) b)

Figure 4-5 – Representative curves of the multi-stage triaxial compressive test performed in this thesis, with different colors for each stage, considering a) the axial and radial strains and b) the confining pressures.

From Figure 4-5, it is noticed that after the unloading step, when the confining pressure is raised, the radial strain and the axial strain increase. These strains increase is due to the confining pressure increase, which induces compaction on the sample (positive values for the axial and radial strains).

Brazilian splitting tests

For the Brazilian splitting test, a 54-mm plug was cut into four disks with 25 mm in thickness each. The tests were carried out on an MTS testing machine (Figure 4-6a), model 810 with load capacity of 250 kN, under actuator displacement control at a rate of 0.02 mm/min. The specimens were placed directly onto the machine platens. While the tests were

running, photographs were taken, in order to perform Digital Correlation Analysis (DIC), to investigate the crack initiation and propagation on the sample surface.

a)

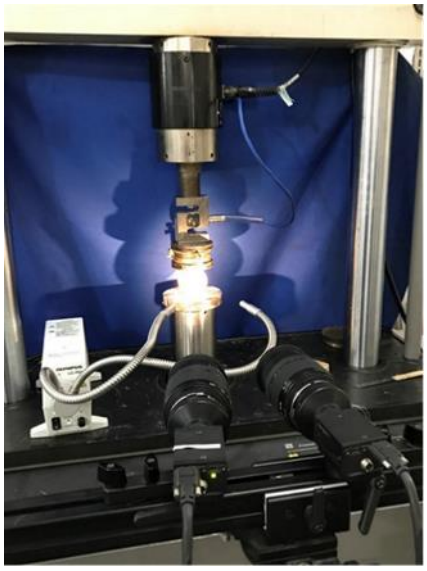

b)

c)

Figure 4-6 – (a) MTS 810 – 500 testing machine used for the Brazilian splitting tests; (b) Cameras and illumination system used for the DIC and (c) an Indiana Limestone disk specimen painted white with black speckles used on the Brazilian splitting test with DIC analysis.

DIC is a non-contact method which allows to follow the development of strains on the surface of a specimen during a test. It was proposed by Sutton et al. (1983) in the beginning of the 1980s. The method is based on taking pictures of the sample during the test, and then comparing those pictures with the initial one (without deformation). The samples are usually painted white with randomly spread black speckles. This speckled pattern enables the system to track groups of speckles to define a displacement field over the sample surface. Knowing the displacement, the system also evaluates the strain field. In this thesis, two CCD cameras (Figure 4-6b) with 5MP (Point Grey GRAS-50S5M), with resolution of 2448 x 2028 pixels and high-resolution lenses type Tamron A031 (AF28-200mm F/3.8-5.6) were used and the photographs were taken at the rate of 1 frame per second. The software VIC SNAP and VIC-

3D 2010, both from Correlated Solutions Inc., were used for image acquisition and processing. All samples were painted white with black speckles for the DIC, as presented in Figure 4-6c.

The splitting tensile strength was calculated by equation (4.1), according to ASTM D3967-16 (ASTM, 2008):

$$\sigma_t = \frac{2\,P}{\pi\,t\,D} \tag{4.1}$$

where σ_t is the splitting tensile strength, P is the maximum applied load, t and D are the thickness and diameter of the specimen, respectively.

4.1.1.2. CO_2 injection test

The CO_2 solution injection test was carried out using a GCTS creep system, model RCT 1000 with CO_2 solution injection, as shown in Figure 4-7.

a)

b)

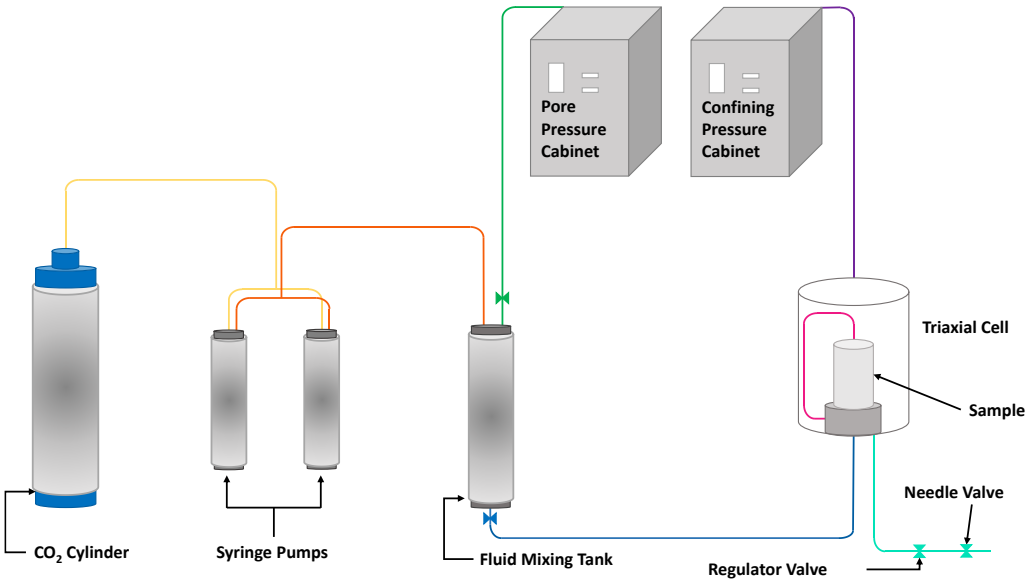

c)

Figure 4-7 – GCTS Rock creep system – RCT 1000, with injection of CO_2 solution. Picture from the entire system in (a); in (b), a picture of the triaxial cell opened and the end of the flow line with the regulator valve. In (c), the scheme with the main components of the system.

This GCTS system has a triaxial cell, with axial load capacity of 1000kN and maximum confining of 70 MPa, a fluid mixing tank with maximum pressure of 3000 psi, two ISCO syringe pumps from Teledyne with a controller and three cabinets to control the confining pressure, axial load and pore pressure manually. The system also has an ultrasonic module (ULT-2000) with transmitter and receiver sensors which allow the continuous monitoring of

compressional and shear wave velocities (V_P and V_S). From these results, an estimative for the dynamic Young's modulus (E_{dyn}) and dynamic Poisson's ratio (ν_{dyn}) are performed according to equation (4.2). Here, V_P and V_S are the P and S-wave velocities, respectively, while ρ is the material density.

$$\nu_{dyn} = \frac{V_P^2 - 2 \cdot V_S^2}{2 \cdot (V_P^2 - V_S^2)}$$
$$E_{dyn} = 2 \cdot \rho \cdot V_S^2 \cdot (1 + \nu_{dyn}) \quad (4.2)$$

LVDTs allow monitoring the axial and radial strains during tests with samples of 25, 38 and 50 mm diameter. Therefore, it was necessary to reduce the size of the Indiana Limestone samples with original diameter of 54 mm and height of 108 mm. In order to allow injection tests with continuous flow, a flow line was installed after the triaxial test, together with a regulator valve, to maintain the pressure in the system. In addition, a needle valve to control the fluid outlet from the system was installed. The fluid mixing tank receives deionized water from the pore pressure cabinet, and the pressure is set by the liquid CO_2 (99.9% of purity) from the syringe pumps. Hence, a CO_2 and deionized water solution is injected in the sample. The system also allows temperature control of the triaxial cell and mixing tank. In addition, micrographs obtained with a Nikon stereo microscope, model SMZ800N were used to compare the surfaces of the sample before and after the CO_2 solution injection test.

Implementing the CO_2 injection test in the PUC-Rio Laboratory for Mechanical Tests

Five samples were tested. The implemented procedure for the injection test is described here. First, each sample was positioned between two steel caps. These caps are designed to conduct fluid inside them while measuring compressional (Vp) and shear velocities (Vs). In order to improve wave propagation, a viscous fluid (honey) was applied between the ends of the sample and the caps, reducing the voids in these contacts. Then, the samples were encapsulated with two layers of heat-shrinking tubing - one of fluorinated ethylene propylene (FEP) and the other of polyolefin, to avoid contamination by the confining fluid. Then, three LVDTs were positioned with two rings and one chain. Two of these LVDTs measure the axial strain while the other measures the radial strain during the experiment. Figure 4-8 presents the final set up before positioning the sample inside the triaxial cell.

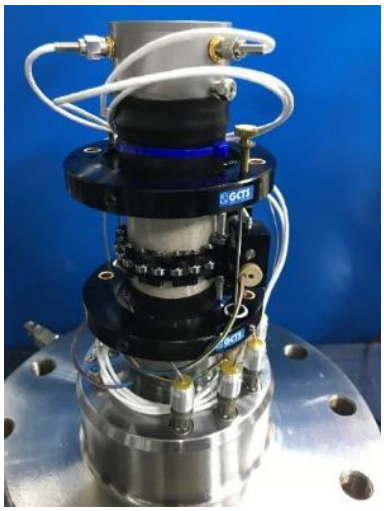

Figure 4-8 – Final set up for Indiana Limestone sample before closing the triaxial cell from the GCTS creep system. There are two rings for positioning the axial LVDTs, and a chain for the radial LVDT.

In order to prepare the CO_2-water solution, the pore pressure cabinet injected deionized water into the fluid mixing tank (FMT), until it was completely filled. Then, the ISCO pumps started injecting the liquid CO_2 into the FMT at a specific pressure (injection pressure shown in Table 4-2). Meanwhile, the FMT was rotated until the pressure inside the fluid mixing tank was constant, and no CO_2 flow rate was observed at the ISCO pumps. It took some hours, and after that, the solution was assumed to be in equilibrium, and ready to be injected through the sample. It is important to highlight that, in this system, the injection pressure is the same as the CO_2 partial pressure and the flow is controlled by this pressure.

Before the test, the confining pressure cabinet injected inert silicone fluid into the triaxial cell. Then, the confining pressure was set manually in the cabinet to the desired value (confining pressure shown in Table 4-2). When the confining pressure was relatively stable, the valve from the FMT was opened and the CO_2 solution flowed in the direction of the sample.

The main test parameters for each sample are presented in Table 4-2. Here, sample P01 was tested in a closed system, where a CO_2 solution was injected and maintained inside the sample until the end of the test. This was carried out mainly for system testing and little or no dissolution was observed, as predicted. Similar results were obtained by Grgic (2011). The CO_2 solution is quickly neutralized by the calcite from the rock and, as it is not refreshed, the reaction is very limited.

In addition, P02 was subjected to two testing conditions, also with the purpose of testing the system. Therefore, only samples P03, P04 and P05 are presented and studied here.

Table 4-2 – Main test parameters used on the injection tests for each Indiana Limestone sample.

Sample	Confining pressure (MPa)	Injection pressure (MPa)	Temperature (ºC)	Injection period (h)
P01	12	6	22	27.3
P02	15	7	22	4.4
P03	18	10	22	17.2
P02	18	10	22	6.4
P04	18	10	22	17.4
P05	18	10	22	54.6

The values of injection pressure and confining pressure were selected according to similar works from literature, where 10 MPa of injection pressure was chosen for Limestone samples, as presented by Eide (2012), Menke et al. (2015) and Lebedev et al. (2017). Menke et al. (2015) and Lebedev et al. (2017) applied a flow of 0.5 ml/min in their experiments, as they were able to control the solution flow. As previously mentioned, in this work, the setup only allows controlling the injection pressure. In addition, the confining pressure of 18 MPa is close to the pressure adopted by references (around 15 MPa). A higher value of confining pressure was adopted due to the system limitation regarding pressure oscillation, as it is manually controlled and depends on the cycles of a hydraulic pump. Therefore, to avoid the confining pressure dropping below the injection pressure, and consequently contaminating the confining fluid with CO_2 solution, the confining pressure was set higher than the injection pressure, as recommended by the system manufacturer.

This system does not allow pH monitoring of the CO_2 solution under test conditions (pressure and temperature). Therefore, only an estimate of the solution pH can be considered, based on studies from the literature, such as in Peng et al. (2013), Haghi et al. (2017) and Schaef et al. (2005). According to these authors, the CO_2-water solution under the conditions presented in Table 4-2 would have a pH around 3.0.

4.1.2. Results

4.1.2.1. Mechanical characterization before acid injection

Brazilian splitting tests

The Indiana Limestone specimens had average splitting strength of 1.43 ± 0.12 MPa. After the sample fails under tensile stress, a crack propagates in the middle of the sample in the direction of the applied load. The stress curve of the representative sample is presented in Figure 4-9. Figure 4-10 presents the sample under the BST right after failure, with the crack in

the middle of the sample surface. The picture of the moment just before failure was used to get the strain field on the sample surface from DIC. Figure 4-11a presents the horizontal strain field while Figure 4-11b presents the vertical strain field on one of the Indiana Limestone samples.

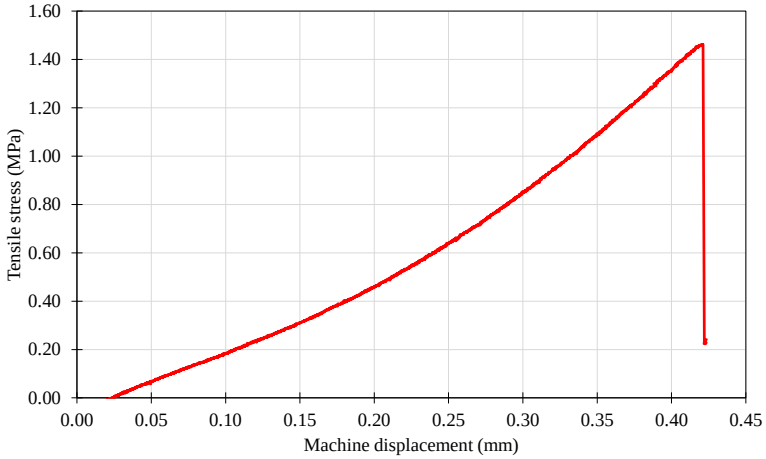

Figure 4-9 – Representative tensile stress x machine displacement curve for the Indiana Limestone obtained in the laboratory.

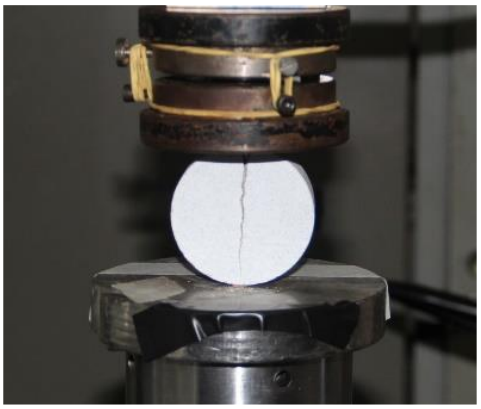

Figure 4-10 – Brazilian test system after sample failure with a crack in the middle of sample surface.

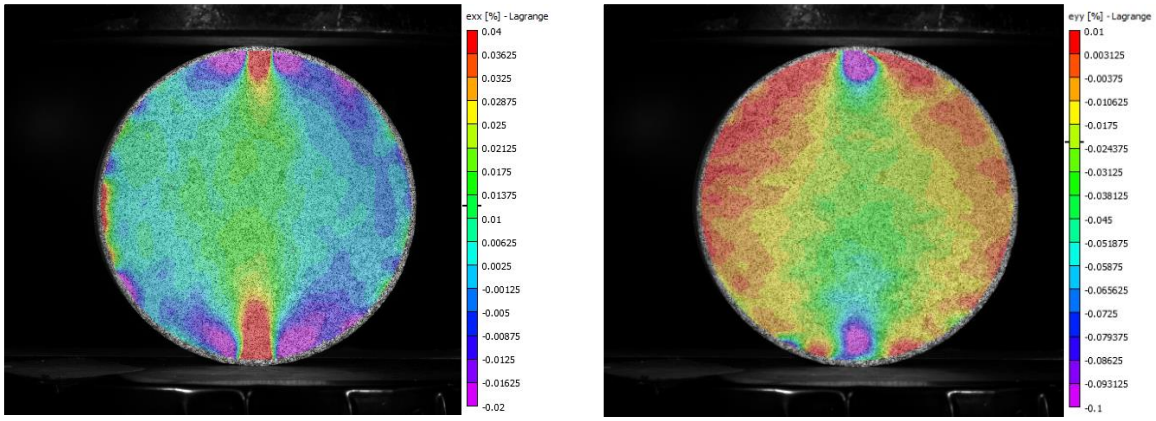

a) b)

Figure 4-11 – Strain field in a) horizontal direction and b) vertical direction of one Indiana Limestone sample obtained by the DIC analysis.

It is possible to note that the crack initiated at the load points and propagated towards the center of the specimens. This behavior does not follow Griffith theory (Fairhurst, 1964), which predicts that, when a disk is submitted to diametrically opposed loads, the center of the disk would fail under tensile stresses which correspond to the strength of the material. Therefore, as the crack did not initiate in the center of the disks, Griffith theory cannot be used. Hence, the values obtained in this study will be used only as an estimative of the Indiana Limestone tensile strength. Li and Wong (2013) presents an interesting review of the Brazilian splitting test, presenting the background and the assumptions, discussing the test validity and also the crack initiation points. Test validity and the crack initiation points are also discussed in other works in the literature (Fairhurst, 1964; Lin et al., 2014).

Triaxial compressive tests

Uniaxial and triaxial compressive tests were performed to assess the Young's modulus, the uniaxial compressive strength (USC) and the Poisson's ratio of the material. In addition, the triaxial compressive test can provide some strength properties, such as cohesion and friction angle.

Figure 4-12 and Figure 4-13 show the curves of axial stress versus axial strain and radial strain, respectively. The axial strain and the radial strain curves from the unconfined sample CP2 shows a unexpected behavior, oscillating and reducing the measured axial strain, due to readings problem with the LVDTs. The samples subjected to the unconfined test presented UCS, Young's modulus and Poisson's ratio of 21.4 $\pm$ 0.44 MPa, 23.46 $\pm$ 0.98 GPa and 0.24 $\pm$ 0.08, respectively. The peak stress from the 2 MPa confining pressure triaxial tests was 30.22 $\pm$ 0.34 MPa and from the 5 MPa confining pressure was 40.66 $\pm$ 0.85 MPa. Also, besides

using only a few replica for each condition, a small variance on the results were observed. Also, the same behavior observed in Walton et al. (2015) was noticed here. The Indiana limestone presented a brittle failure under uniaxial conditions, and a ductile failure when subjected to triaxial tests.

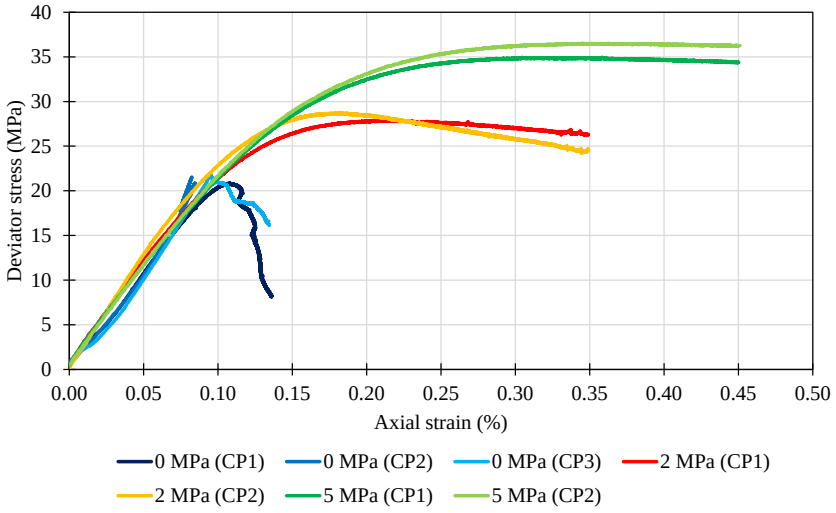

Figure 4-12 – Axial strain results for uniaxial (0 MPa confining pressure) and triaxial (2 MPa and 5 MPa confining pressure) compressive tests on Indiana Limestone samples with 42 mm in diameter and 84 mm in height.

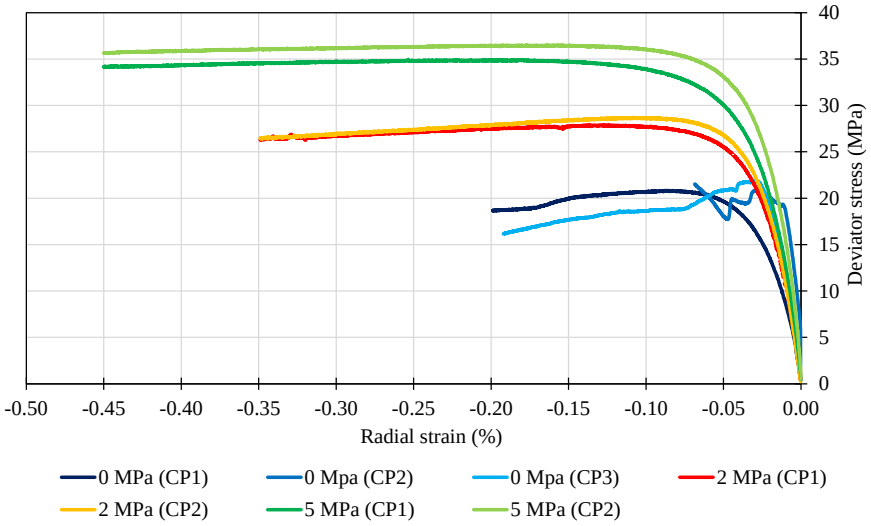

Figure 4-13 – Radial strain results for uniaxial (0 MPa confining pressure) and triaxial (2 MPa and 5 MPa confining pressure) compressive tests on Indiana Limestone samples with 42 mm in diameter and 84 mm in height.

Multi-stage triaxial compressive tests

The results obtained from the multi-stage triaxial compressive tests for the intact samples (not subjected to dissolution process) are presented in Table 4-3.

Table 4-3 – Results from the multi-stage triaxial test on intact Indiana Limestone 54-mm diameter samples.

		Average	Stand Dev.
Uniaxial	UCS (MPa)	32.90	3.22
	E (GPa)	30.87	1.31
	ν	0.15	0.01
2 MPa confining pressure	Peak deviator stress (MPa)	45.08	1.52
5 MPa confining pressure	Peak deviator stress (MPa)	55.63	1.80
Strength	c (MPa)	7.8	-
	ϕ (º)	44.2	-

There is a difference in the values of the mechanical properties obtained from the single triaxial tests (Figure 4-12 and Figure 4-13) when compared with the values from the multi-stage triaxial tests (Table 4-3). This difference is most likely due to the radial strain rates adopted, with 0.00147 mm/min for the single triaxial tests, and 0.006 mm/min for the multi-stage triaxial tests. One other possibility is that different testing systems were used, with different frame stiffnesses. Above all, the samples used in these two tests were purchased from different batches which could have different properties.

The deviator stress versus axial strain and radial strain curves from the multi-stage triaxial tests on samples IL1, IL2 and IL3 are presented in Figure 4-14. The results obtained by the three multi-stage triaxial tests showed small variance, when comparing some curve parameters, all having coefficient of variance (COV) under 10%. In addition, the behaviors from the axial strain and radial strain curves from these three tests were very similar. Therefore, this characterization will be used for comparison with the samples subjected to CO_2 solution injection.

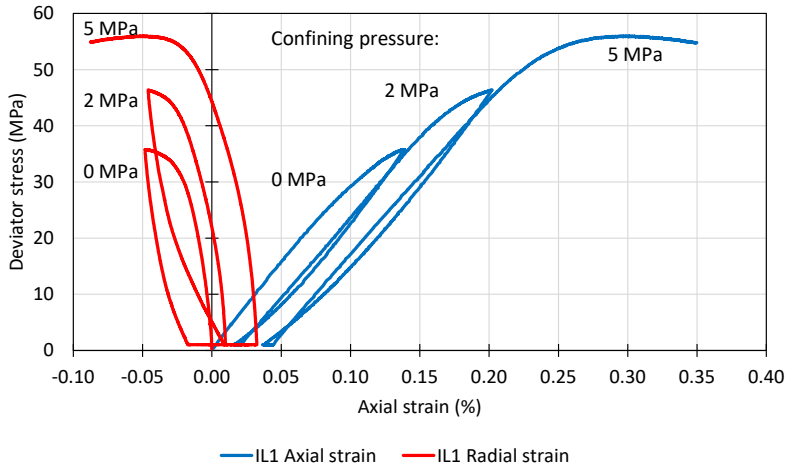

a)

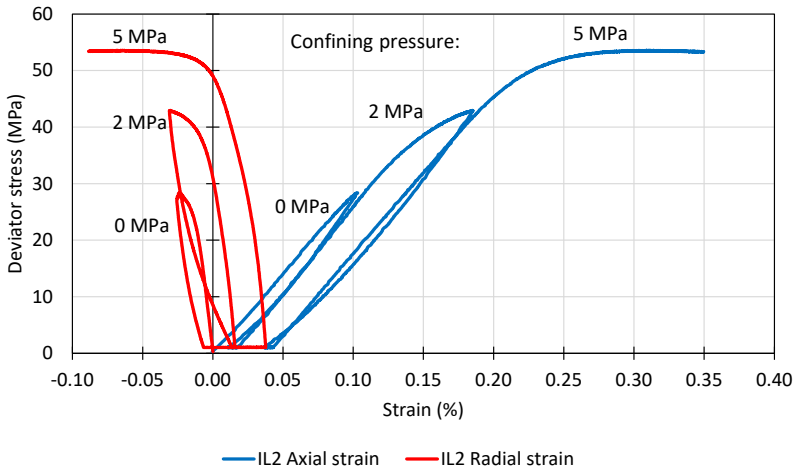

b)

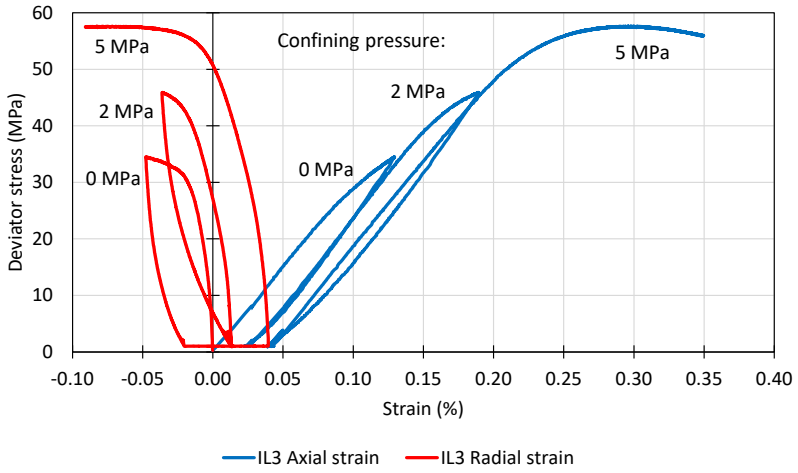

c)

Figure 4-14 – The multi-stage triaxial tests (0 MPa, 2 MPa and 5 MPa confining pressures) on the intact Indiana Limestone samples a) IL1; b) IL2 and c) IL3.

4.1.2.2. CO_2 solution injection

For samples P03, P04 and P05, optical micrographs were obtained from both sample ends, top and bottom, before and after the injection test. The bottom end corresponds to the solution injection surface. The top of P03 before and after the injection test is shown in Figure 4-15, while the bottom of P03 is presented in Figure 4-16. Comparing the images from before and after the injection test, surface porosity changes are not visually observed in sample P03. On the other hand, sample P04 presents a clear porosity increase on the surfaces of the sample. Figure 4-17 presents the top of sample P04 and Figure 4-18 the bottom of P04 before and after the injection of CO_2 solution. Similarly, sample P05 presents a large increase in surface porosity at the top and bottom ends. Figure 4-19 shows the top surface of sample P05, while

Figure 4-20 the bottom surface. The bottom surface (CO_2 solution entrance) presents more considerable porosity changes when compared to the top surface.

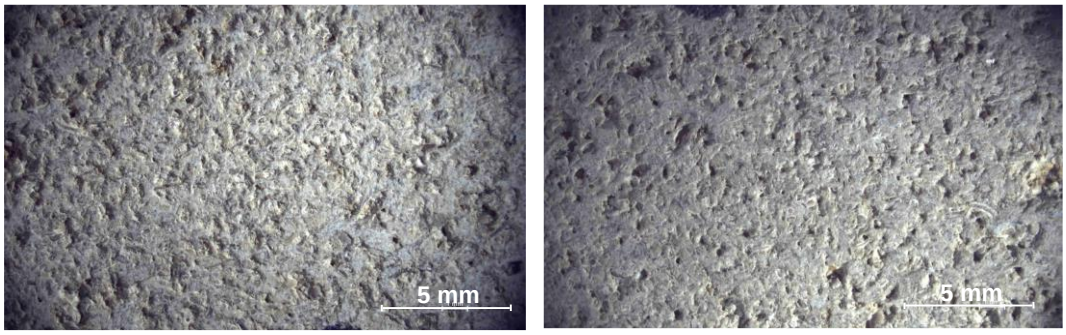

a) b)

Figure 4-15 – Micrograph (1x) of Indiana Limestone sample P03 top a) before and b) after the CO_2 solution injection test.

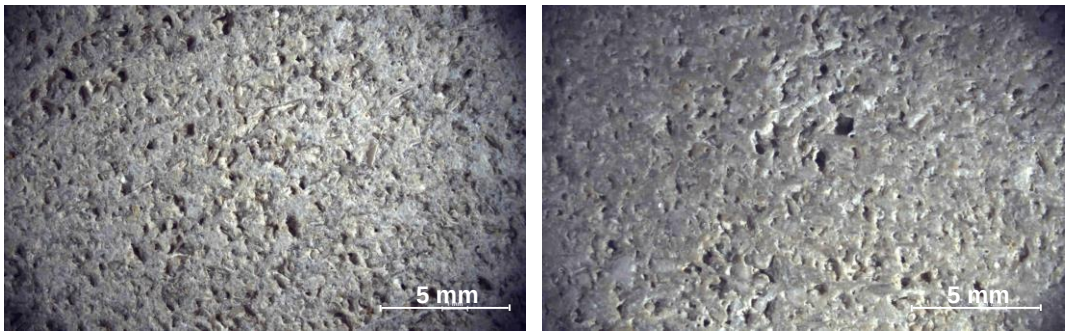

a) b)

Figure 4-16 – Micrograph (1x) of Indiana Limestone sample P03 bottom a) before and b) after the CO_2 solution injection test.

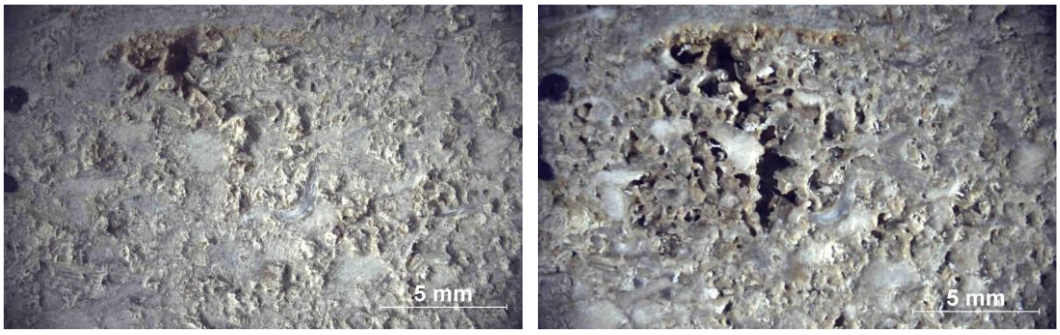

a) b)

Figure 4-17 – Micrograph (1x) of Indiana Limestone sample P04 top a) before and b) after the CO_2 solution injection test.

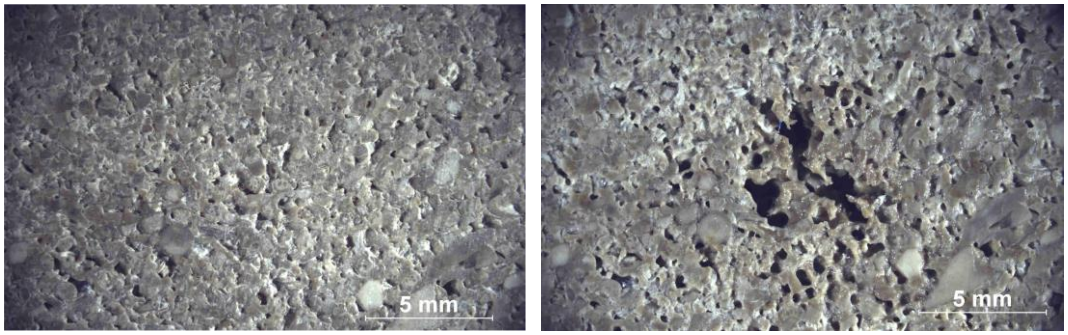

a) b)

Figure 4-18 – Micrograph (1x) of Indiana Limestone sample P04 bottom a) before and b) after the CO_2 solution injection test.

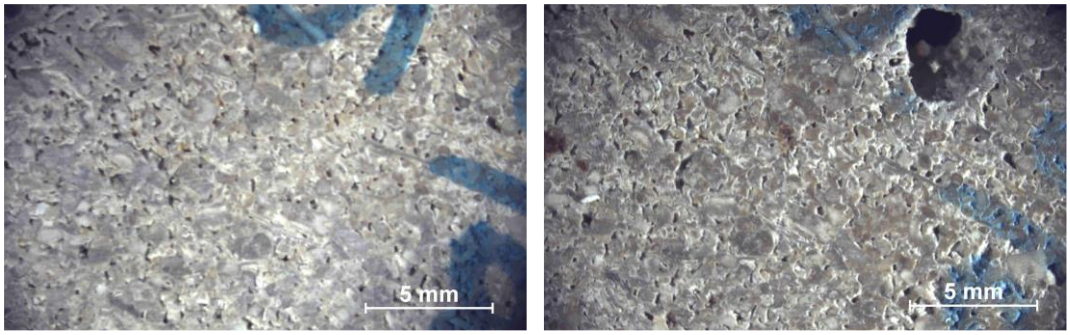

a) b)

Figure 4-19 – Micrograph (1x) of Indiana Limestone sample P05 top a) before and b) after the CO_2 solution injection test.

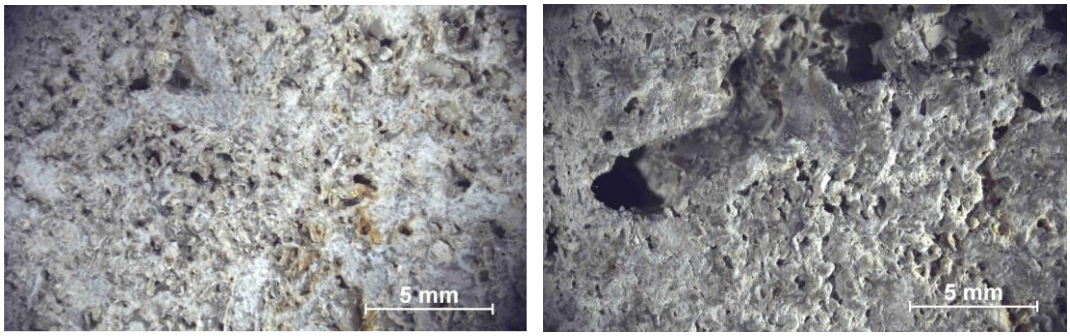

a) b)

Figure 4-20 – Micrograph (1x) of Indiana Limestone sample P05 bottom a) before and b) after the CO_2 solution injection test.

As P05 was the sample that clearly went through most alterations on its surface and was subjected longest to the acid, its test results are presented here with more detail, as all samples were subjected to similar conditions during the injection test. The results from samples P03 and P04 are presented in Appendix A. Figure 4-21 presents the confining pressure and the injection (FMT) pressure during the test in P05. The confining pressure oscillated during the test due to the nature of the system, which works with a hydraulic pump under manual control,

as explained in Section 4.1.1.2. The fluid mixing tank (FMT) pressure also oscillated, although less than the confining pressure, mostly due to the behavior of the system. As the injection valve was open, the fluid from the FMT flowed in the direction of the sample, therefore, reducing the FMT pressure. In order to compensate this reduction, the ISCO pumps worked more frequently in the beginning of the test. In Figure 4-21 it is possible to notice the time when the injection valve was opened and the CO_2 solution started to flow to the sample, which was around 2.4 hours. After 57 hours of testing, the fluid injection stopped, as the ISCO pumps were not able to maintain the continuous flow - one of the pumps became empty while the other one was still under the refill process, therefore, the ISCO pump system stopped.

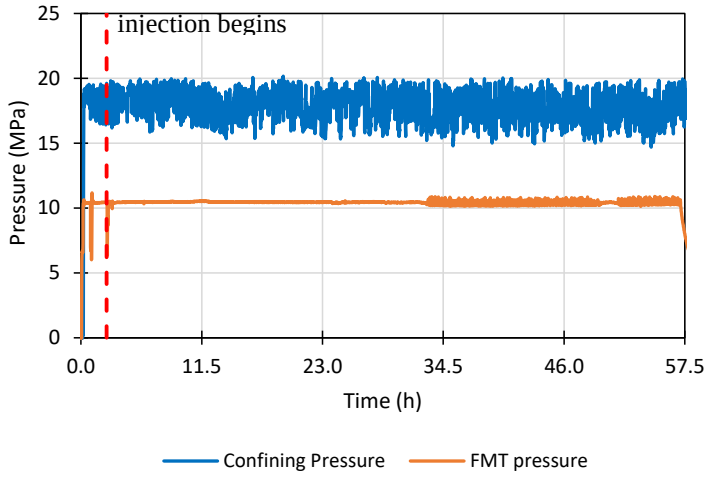

Figure 4-21 – Confining pressure and injection (FMT) pressure during the CO_2 injection test on Indiana Limestone sample P05.

The system is not able to directly monitor the injection flow. Instead, it monitors the flow of the ISCO pumps, which are responsible for injecting liquid CO_2 into the fluid mixing tank and maintaining the set pressure in the FMT (in this case, a pressure of 10 MPa). Figure 4-22 presents the flow from the ISCO pumps A and B during the entire test, with a zoom in the flow rates until 10 ml/min, for better visualization. In the continuous flow mode, both pumps work intercalating, in order to always provide liquid CO_2 for the FMT. To automatize the process, the auto-refill mode was used, in which the pumps refill automatically. The top and bottom values of flow (50 ml/min and -40 ml/min) represent the refill cycle of each pump. During refill, the pump closes the valve that connects the pump to the FMT, and receives the liquid CO_2 at a pressure of 6 MPa (pressure from the CO_2 cylinder) at a flow of -40 ml/min, while the other pump keeps pressurizing the system. Then, the pump in the refill cycle has to reach the same pressure of the FMT (in this case, 10 MPa), which requires moving the pump piston with a flow of 50 ml/min. Afterwards, the CO_2 solution injection from this particular pump restarts.

Figure 4-22a presents the flow from pumps A and B during the first part of the test (until 32 hours of testing). Overall, the flow was close to 1.0 ml/min during the first 9.5 hours of test. We adjusted the needle valve at the outlet so that the flow would be around 1-2 ml/min. However, after around 11.5 h of testing the flow decreased to values below 0.1 ml/min. The valve was again adjusted after 25 h and the flow of around 1-2 ml/min was reestablished. Figure 4-22b presents the flow from pumps A and B from 32 hours to 42 hours of testing. It is noticed that the average flow was around 1 ml/min during this period. After 42 hours, the flow trend decreased a little, to average values below 1 ml/min, until 48 hours, when it increased again, to an average value of 2 ml/min, as presented in Figure 4-22c. The pump flow during the last hours of the test is presented in Figure 4-22d. The flow average value kept oscillating around 4 ml/min until the end of the test, reaching higher values (as high as 7 ml/min). We can observe that, with the higher flow, the pumps had to be refilled more often.

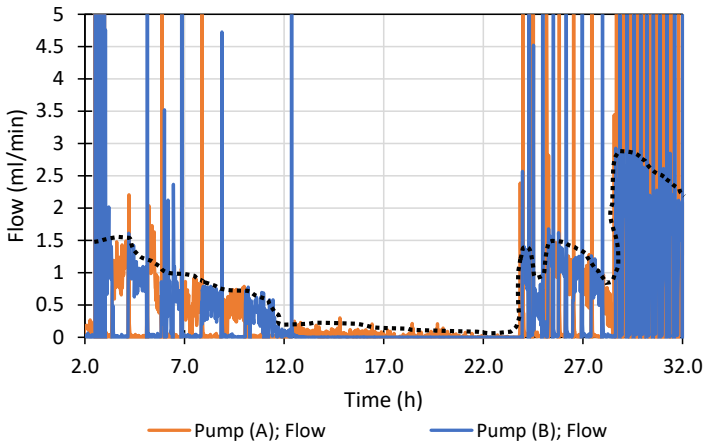

a)

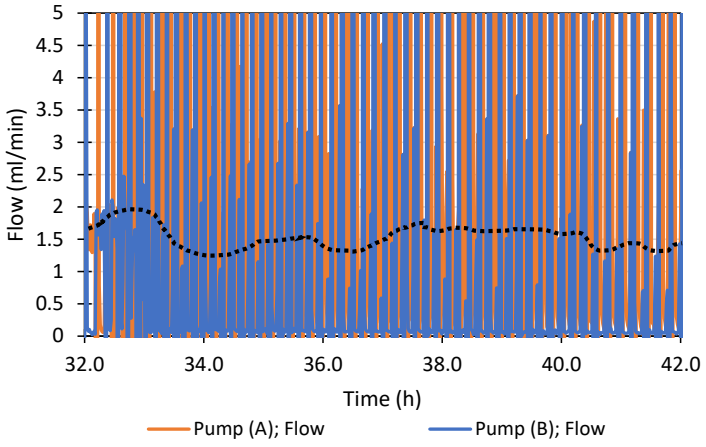

b)

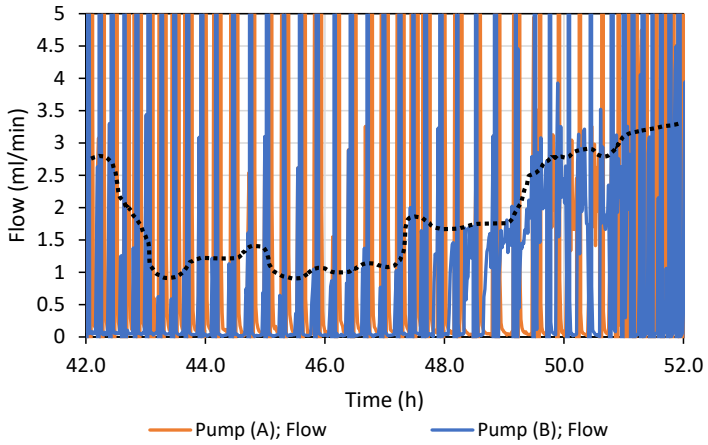

c)

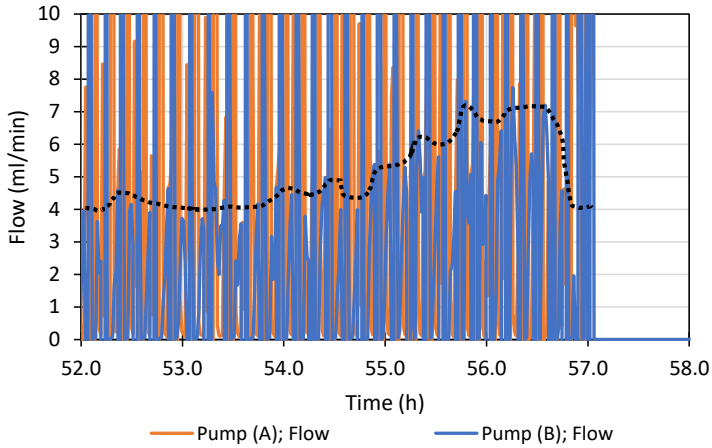

d)

Figure 4-22 – ISCO pumps A and B flow in sample P05 a) until 32 hours; b) from 32 to 42 hours; c) from 42 to 52 hours and d) from 52 to 58 hours of CO_2 injection testing on Indiana Limestone sample P05. The black traced lines are the approximately average flow rate observed.

The temperatures at the triaxial cell wall (TRX wall temperature), at the inner triaxial cell (TRX inner temperature) and inside the FMT (FMT inner temperature) were monitored during the test and are presented in Figure 4-23. These temperatures decreased until around 10 hours of testing, and then maintained almost constant, following the variations from the room temperature. It is important to observe that the room is not temperature controlled, therefore, variations are expected.

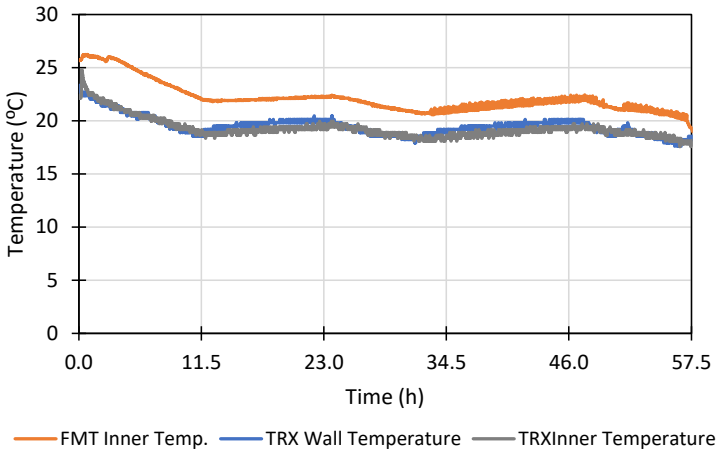

Figure 4-23 – Temperature at triaxial cell (TRX) and at the fluid mixing tank (FMT) during the CO_2 injection test on Indiana Limestone sample P05.

Finally, the axial strain, the radial strain and the volumetric strain during the experiment were recorded and are presented in Figure 4-24 for the entire test. For the axial strain, the average readings from both LVDTs were used. Regarding the observed strains, when the confining pressure was applied, all strains increased and, when the injection started, they decreased, as effective stress was reduced from 18 MPa to 8 MPa (effective stress is the difference between confining pressure and injection pressure).

After about 15 h of test, the axial strain increased, which could indicate that compaction took place. However, it decreased after 25 h and increased again after about 35 hours. There is no clear explanation for this strain behavior. It may be due to the CO_2 solution flow pattern, as it can increase or decrease the pore pressure in the sample, which could explain the changes on the recorded strains.

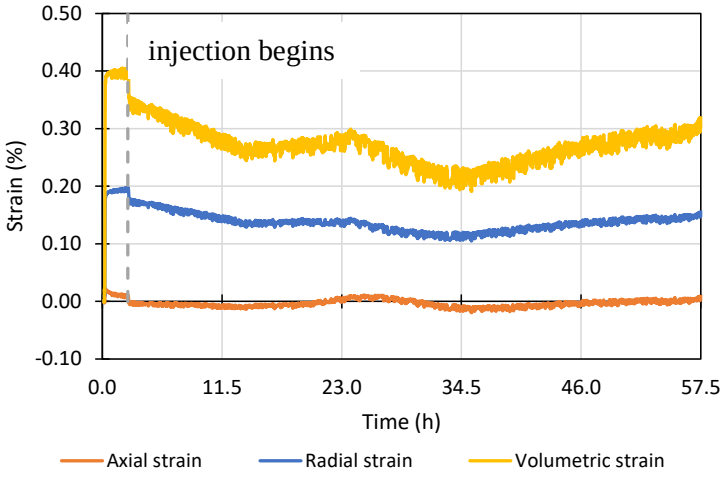

Figure 4-24 – Axial strain, radial strain and volumetric strain on Indiana Limestone sample P05 during the entire CO_2 injection test.

During the CO_2 solution injection test, compressional (P) and shear (S) waves were monitored. The P and S waves were measured once every 30 min during the experiment. In Figure 4-25a and Figure 4-25b, the comparison among the ultrasonic P and S waves, respectively, before (pre-dissolution) and after (post-dissolution) the CO_2 injection test is presented. In both scenarios, the confining pressure was 18 MPa, and no injection pressure was applied. A decrease in P and S-wave amplitudes through the test was clear, while the velocity change was subtle. The increase on sample porosity may have influence on the amplitudes, as presented by Boadu (1997), and Tompkins and Christensen (2001).

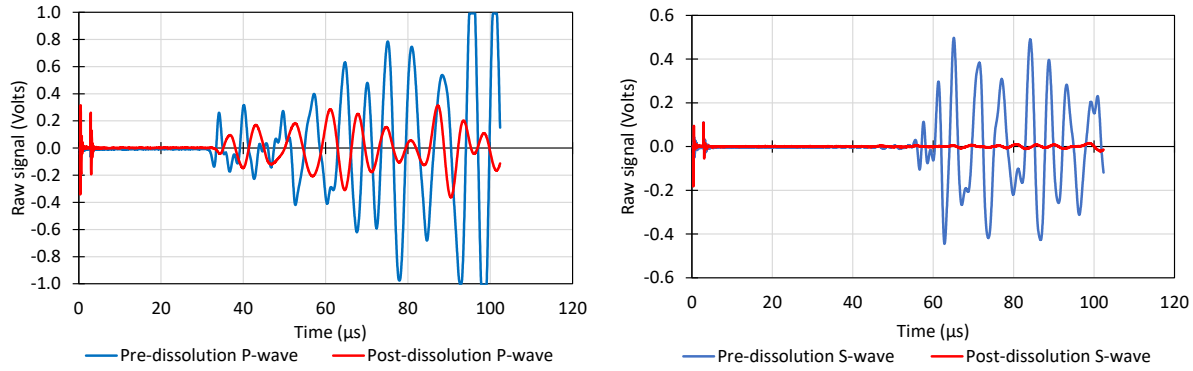

a) b)

Figure 4-25 – Ultrasonic waves before and after the CO_2 solution injection on Indiana Limestone sample P05 under confining pressure of 18 MPa. In (a) P-waves, in (b) S-waves.

4.1.2.3. Mechanical characterization after acid injection

In order to assess the changes to the rock mechanical properties due to dissolution, a multi-stage triaxial compressive test was carried out, according to procedure described in Section 4.1.1.1. As the dissolution process is different for each sample, this methodology gives the possibility of studying a higher number of mechanical parameters from a single dissolution process. A comparison among the results from the intact Indiana Limestone samples and the results from the Indiana Limestone samples subjected to the CO_2 solution injection is presented in Table 4-4. Here, the reference values are the average and the standard deviation from tests with the intact Indiana Limestone samples (Table 4-3).

Table 4-4 – Comparison among intact Indiana Limestone samples (reference) and Indiana Limestone samples P03, P04 and P05 after the CO_2 solution injection.

		Reference	P03	P04	P05
Uniaxial	Strength (MPa)	32.90 ± 3.22	26.81	19.86	24.16
	E (GPa)	30.87 ± 1.31	25.65	22.28	24.48
	ν	0.152 ± 0.01	0.125	0.104	0.151
2 MPa confining pressure	Peak deviator stress (MPa)	45.08 ± 1.52	38.28	33.38	35.71
5 MPa confining pressure	Peak deviator stress (MPa)	55.63 ± 1.80	45.99	40.66	43.87
Strength	c (MPa)	7.8	7.0	5.5	6.4
	ϕ (º)	44.2	40.9	42.0	41.6
CO_2 injection	Test duration (h)	-	17.2	17.4	54.6

From Table 4-4, the material strength and stiffness have reduced when compared to the values obtained on the intact samples. This properties reduction is expected mainly due to calcite dissolution. It is interesting to observe that although the Indiana Limestone is considered a fairly homogeneous carbonate rock, the dissolution process does not change the mechanical properties with the same proportion for all samples. P03, P04 and P05 samples were subjected to a similar dissolution condition, showing a similar trend of changes in properties, but with different values. The multi-stage triaxial test results for samples P03, P04 and P05 are shown in Figure 4-26. The behaviors observed from the axial strain and the radial strain curves in all the tested samples were very similar. The first stage of the test on sample P05 showed a deviator stress decrease during the loading step, around 9 MPa of deviator stress. This decrease probably occurred due to sample compaction, as it was observed a significant increase on sample porosity from Figure 4-19 and Figure 4-20. After this variation, the deviator stress increased, until the end of this first stage (deviator peak stress of 24.2 MPa).

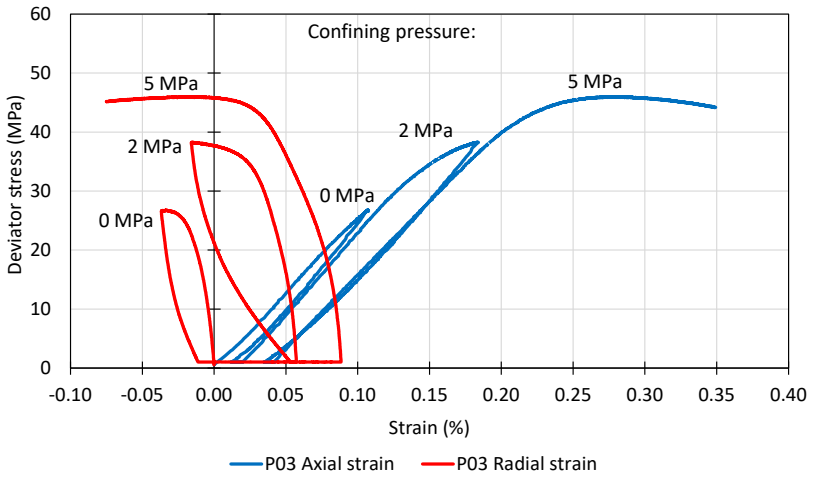

a)

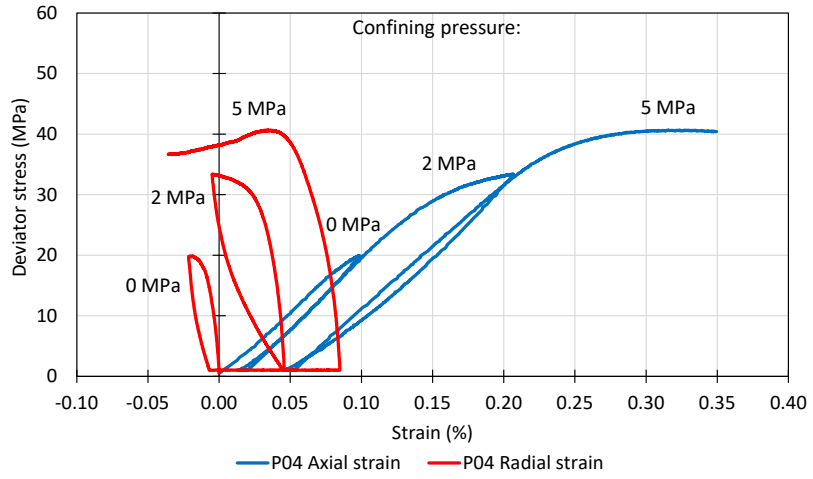

b)

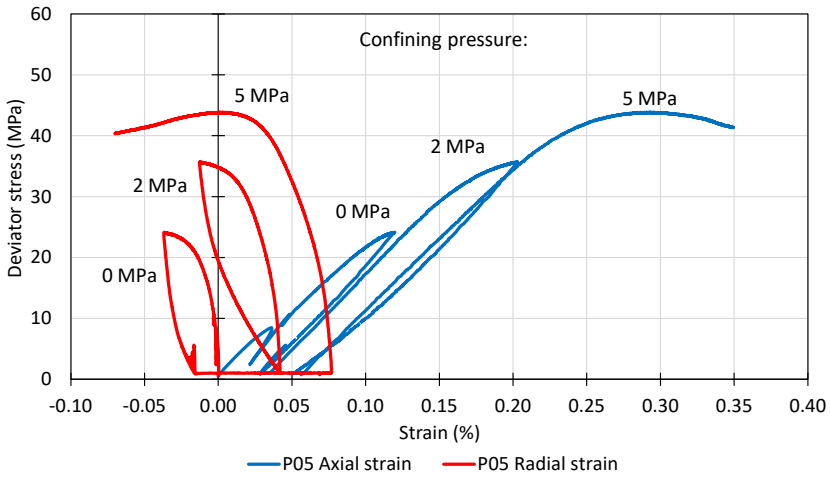

c)

Figure 4-26 – Laboratory multi-stage triaxial compressive test (0 MPa, 2 MPa and 5 MPa confining pressures) results for sample a) P03, b) P04 and c) P05 after CO_2 solution injection test.

The results from Table 4-4 are also presented as percentage variation related to the reference values in Figure 4-27 for the peak deviator stress changes, in Figure 4-28 for the Young's modulus change and in Figure 4-29 for Poisson's ratio variations.

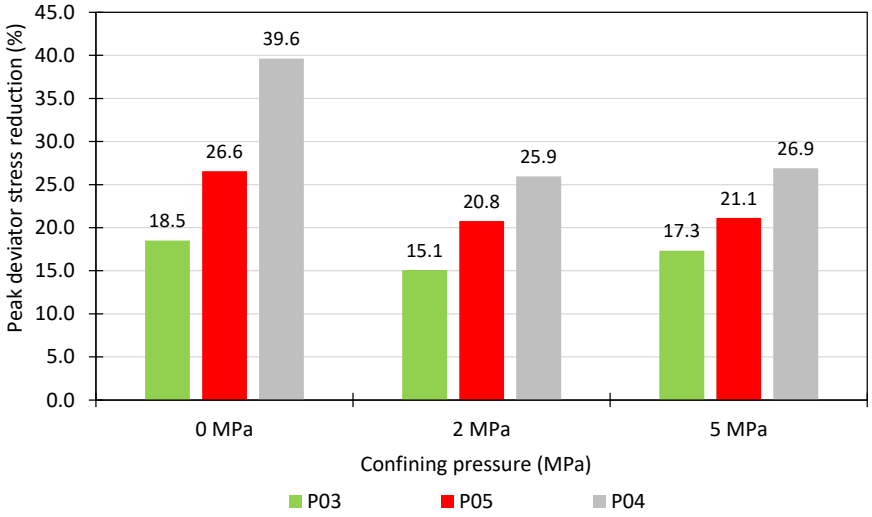

Figure 4-27 – Peak deviator stress reduction for each stage for the altered Indiana Limestone samples P03, P04 and P05 related to the intact (reference) samples.

The peak stresses from samples P03, P04 and P05 considering all the different stages of confining pressure are below the peak stress obtained from the reference samples. This indicates that all the samples subjected to CO_2 solution injection had a reduction on their peak stress. Sample P03 is the one with the lower peak stress reduction, followed by sample P05, and then, by sample P04, with the highest reduction on the peak stress.

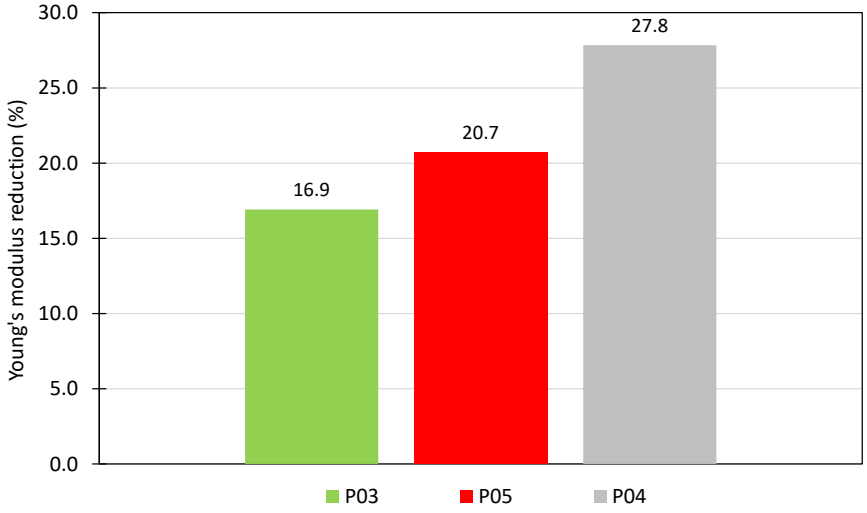

Figure 4-28 – Young's modulus reduction for the altered Indiana Limestone samples P03, P04 and P05 related to the intact (reference) samples.

The same trend observed on the reduction of the peak stress on samples subjected to CO_2 solution injection is also observed when evaluating the Young's modulus.

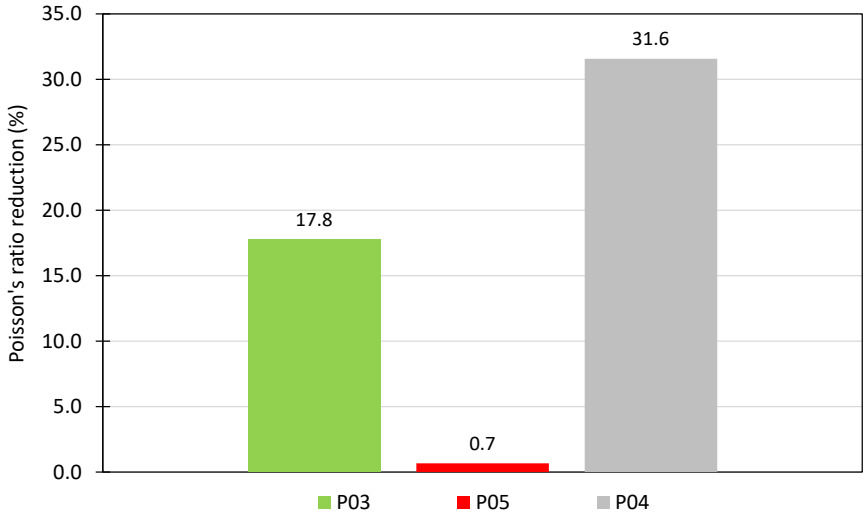

Figure 4-29 – Poisson's ratio reduction for the altered Indiana Limestone samples P03, P04 and P05 related to the intact (reference) samples.

The Poisson's ratio from sample P05 did not change when compared to the reference samples, considering the reference standard deviation. This behavior may be due to sample compaction observed in the beginning of the first stage of the test. Therefore, it was very difficult to define an elastic region (straight line) on the radial strain curve for the evaluation of the Poisson's ratio. On the other hand, the Poisson's ratios from P03 and P04 were 17.8% and 31.6% below the reference value, respectively.

Regarding the P and S-wave results, V_P and V_S before and after the solution injection for each sample are presented in Figure 4-30. The results for the E_{dyn} before and after the solution injection are presented in Figure 4-31 for samples P04 and P05.

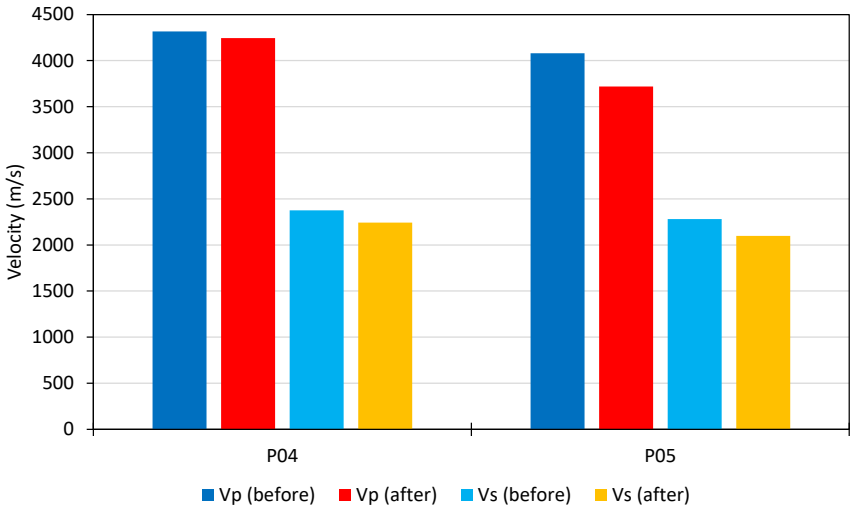

Figure 4-30 – P- and S-wave results for Indiana Limestone samples P03, P04 and P05 before and after the CO_2 solution injection test.

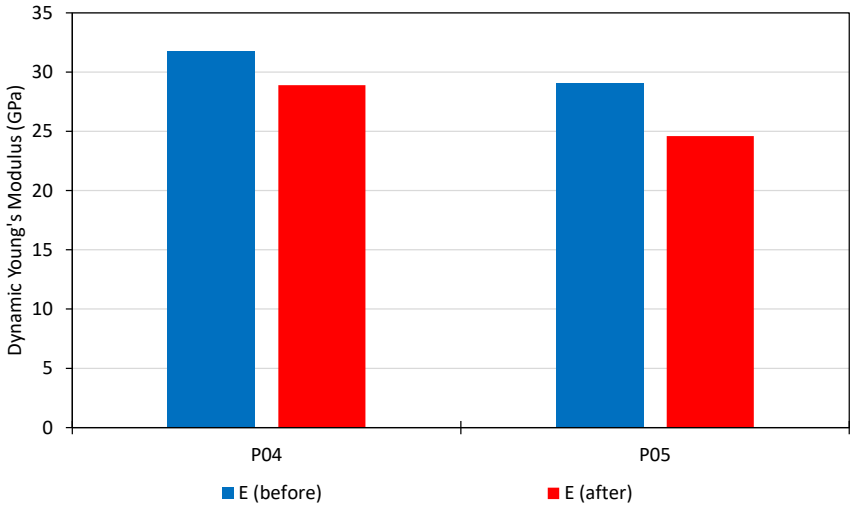

Figure 4-31 – Dynamic Young's modulus before and after the CO_2 solution injection test for Indiana Limestone samples P03, P04 and P05.

As expected, V_P and V_S decreased after the CO_2 solution injection in samples P04 and P05, and as a consequence, the dynamic Young's modulus also decreased. It indicates a change on the pore structure of samples P04 and P05 due to the injection of CO_2 solution.

4.2. Coquina

In addition to the Indiana Limestone samples, coquina samples from Morro do Chaves were also tested. These samples were plugged from an outcrop coquina block at Solintec with a diameter of 25 mm (Figure 4-32), and trimmed to have 50 mm in height. Samples were cleaned with toluene and methanol to remove oil and salt, respectively, and were subjected to porosity

and permeability measurements (Table 4-5). Cleaning followed item 3.6 (core cleaning) from the API RP 40 (1998) procedure.

Table 4-5 – Porosity and permeability measurements on coquina samples performed by Solintec.

Sample	Permeability (mD)		Porosity	Pore Volume (cm^3)	Solid Volume (cm^3)	Height (cm)	Diameter (cm)	Weight (g)
	Air	Klinkenberg						
B5	7.504	6.658	10.31	2.56	22.28	4.97	2.54	60.50
C5	14.477	12.911	11.04	2.76	22.24	4.99	2.54	60.32

The nomenclature for each sample was determined according to the position of the sample. The letter represents the hole from which the sample was plugged, and the number identifies the “depth”. Figure 4-32a shows the coquina block and the position of each hole. In addition, Figure 4-32b and Figure 4-32c present the image of coquina samples C5 and B5, respectively.

a)

b)

c)

Figure 4-32 – a) Picture from the coquina block with the hole positions and the letters assigned to each hole after Solintec plugging procedure, and pictures of samples b) C5 and c) B5 before subjected to the tests.

From all the plugged samples, sample C5 was selected for further analyses, such as optical microscopy, CO_2 solution injection and micro CT scans, as it presents the higher value of permeability among all plugged samples. For the optical microscopy, thin sections were prepared and analyzed by Solintec, using the software Petroledge. The sample was characterized as a bivalve Rudstone, solid, well selected, composed by mosaic calcite and macrocrystalline filling interparticle pore. The porosity was estimated to be around 11%, consisting of fracture, moldic, intraparticle and interparticle pores, according to the carbonate rocks classification from Chorquette and Pray (1970).

4.2.1.Methods

4.2.1.1. Mechanical characterization

Multi-stage triaxial compressive test

For the multi-stage triaxial compressive tests performed before and after the CO_2 injection, a procedure similar to the one presented in Section 4.1.1.1 was followed. The only difference is that the radial strain rate adopted for the coquina samples was 0.005 mm/min for loading and unloading deviator stress.

4.2.1.2. Pore structure characterization

Micro CT scan

In order to investigate the changes on the pore structure of the coquina samples, micro computer tomography (micro CT) scans were obtained before and after the CO_2 injection test. The scans were performed in two micro CT equipment of the same model: Xradia 510 Versa, from Zeiss, with a resolution of 14 μm. The initial scan was performed at PUC-Rio while the second was performed at Universidade Federal Fluminense (UFF). The scans were processed using the free software ImageJ for segmentation and analysis of each slice, as well as for the reconstruction of the 3D pore structure.

Porosimetry

The coquina samples were subjected to a porosity and permeability measurement in Solintec before and after the injection of CO_2 solution. The procedures followed API RP 40 (1998), with the porosity being measured by a gas porosimeter (Boyle law).

Optical microscopy

The porosity change on the surface of the plug was qualitatively evaluated by visually observing the top and bottom of the plug under a stereo microscope from Nikon, model SMZ800N.

4.2.1.3. CO_2 injection test

In order to carry out the CO_2 solution (CO_2 and deionized water) injection test on coquina sample C5, the procedure described in Section 4.1.1.2 was adopted. Figure 4-33 presents the final set up before closing the triaxial cell.

Figure 4-33 – Final set up for C5 sample before closing the triaxial cell from the GCTS creep system used for CO_2 injection test.

4.2.2. Results

4.2.2.1. Characterization before acid injection

Figure 4-34a presents a slice image from the CT scan carried out on sample C5 without any image processing, while Figure 4-34b presents the same slice as a binary image before injecting the CO_2 solution. Figure 4-34c shows a 3D image of the pore structure of sample C5 before the injection of CO_2 solution obtained from the micro CT scan and Figure 4-35 shows the porosity along sample C5 before the CO_2 injection, with 0 mm being the top sample, and 50 mm, the bottom end. The sample had a micro CT average porosity of 9%, which is lower than the value measured by the porosimeter (11%). This was expected, once the pores smaller than 14 μm were not computed due to the CT scan resolution.

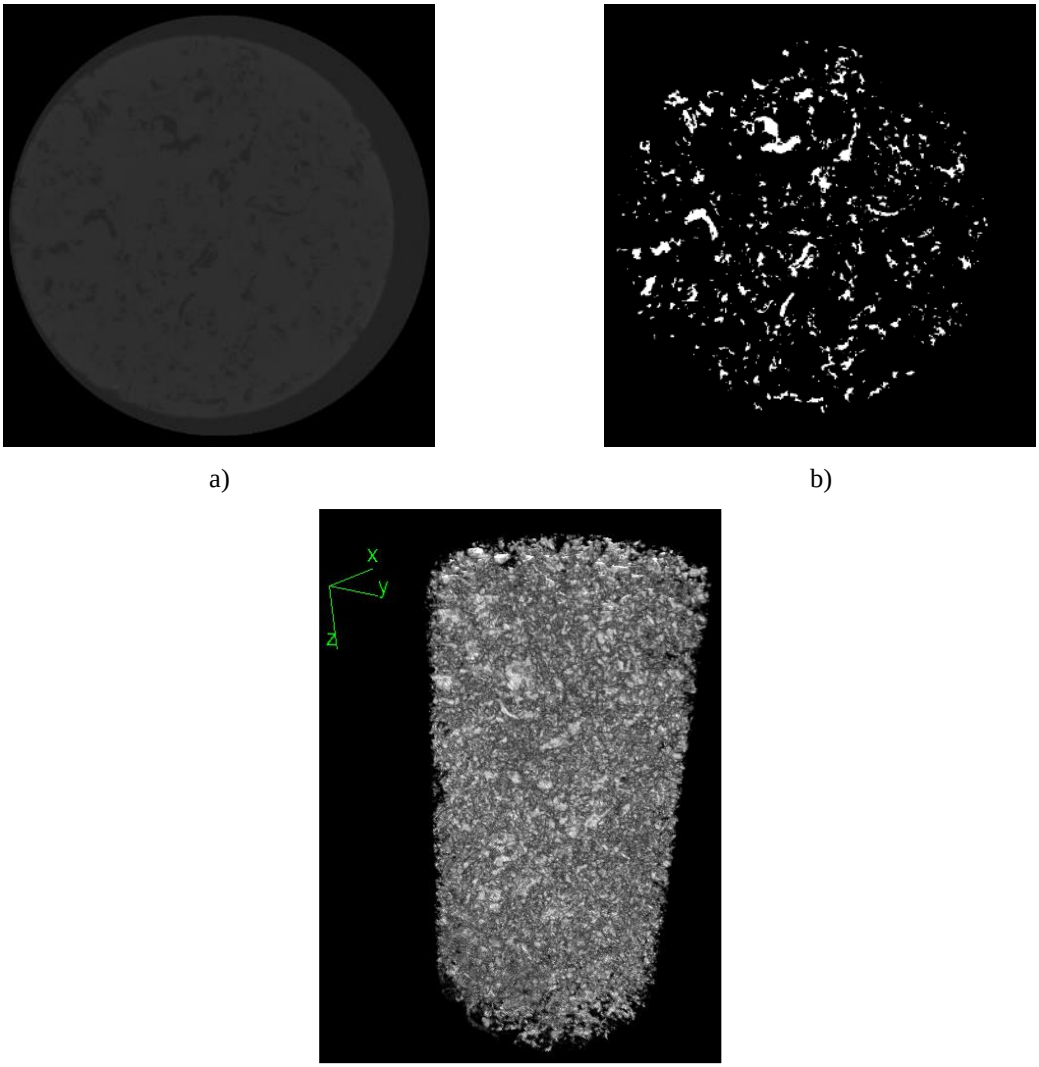

a) b)

c)

Figure 4-34 – CT scan slice on coquina sample C5 a) without any image processing and b) as binary image before CO_2 injection, showing only pores and c) 3D image of the pore structure of coquina sample C5 obtained from micro CT scan before acid injection.

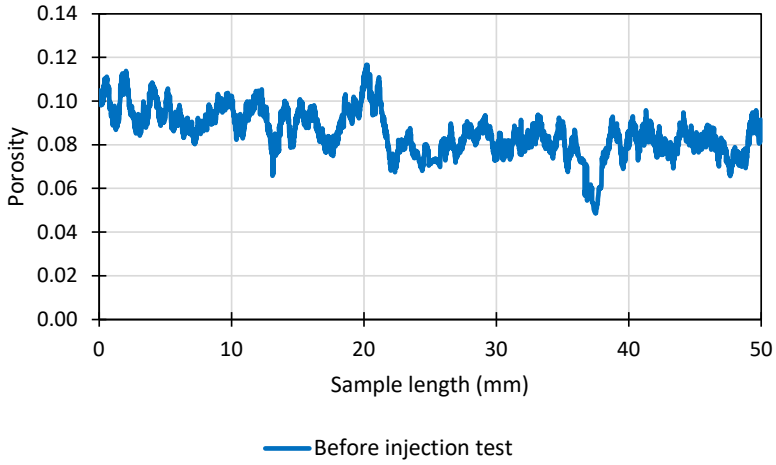

Figure 4-35 – Porosity from the CT scan before CO_2 injection test along coquina sample C5. The left (0 mm) is the top of the sample, while the right (50 mm) is the bottom end.

In order to obtain the mechanical properties of an intact coquina, it was assumed that the mineralogical variations in the block was depth dependent, and, therefore, porosity would play a major role on the mechanical properties. As such, a sample with porosity close to plug C5 was selected. According to Figure 4-32 and Table 4-5, sample B5 was close to sample C5 in the block, and at the same depth as C5. Figure 4-36 presents the results of the multi-stage triaxial tests performed on sample B5.

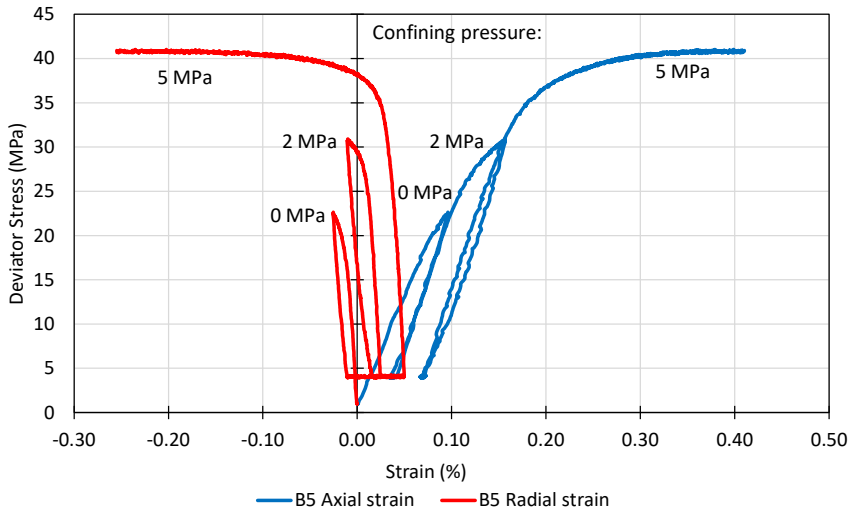

Figure 4-36 – Axial strain and radial strain curves obtained from the laboratory multi-stage triaxial test (0 MPa, 2 MPa and 5 MPa confining pressures) on intact coquina sample B5 (unaltered sample).

The deviator stress for the unaltered coquina sample reached 22.62 MPa in the first stage, with Young´s modulus of 28.63 and Poisson's coefficient of 0.161. During the second stage, with 2.0 MPa confining pressure, the deviator stress reached 30.92 MPa while for the last stage,

with 5.0 MPa confining pressure, the peak deviator stress was 41.04 MPa. Regarding the Mohr Coulomb parameters, the cohesion is 5.5 MPa and the friction angle is 40.36º.

4.2.2.2. CO_2 solution injection

Optical micrographs were obtained on both C5 sample ends, top and bottom, before and after the injection test. The top of C5 before and after the injection test is shown in Figure 4-37, while the bottom is presented in Figure 4-38. Comparing the images from C5 surfaces before and after the injection of CO_2 solution, a considerable increase on porosity is observed.

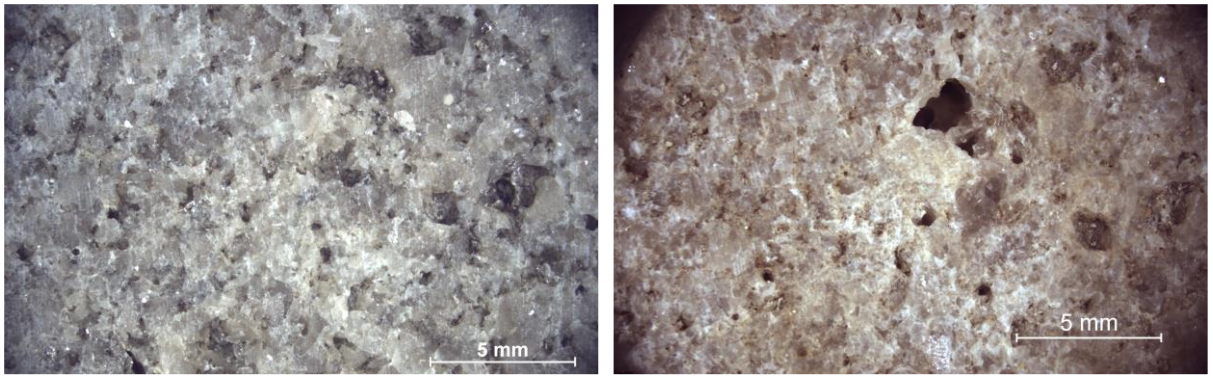

a) b)

Figure 4-37 – Bottom of sample C5 a) before CO_2 injection test, with only small pores on the surface and b) after CO_2 injection test with larger pores.

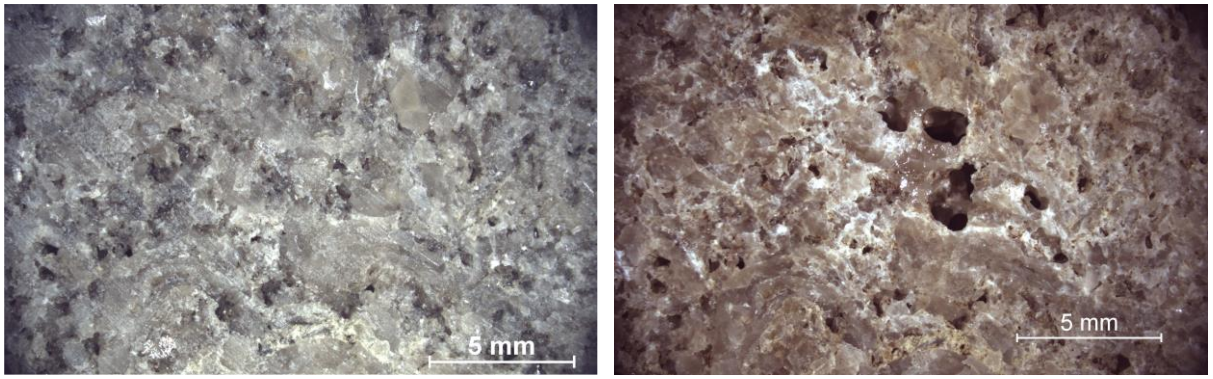

a) b)

Figure 4-38 – Top of sample C5 a) before CO_2 injection test, with only small pores on the surface and b) after CO_2 injection test with larger pores.

The pressures applied to plug C5 during the injection test are shown in Figure 4-39. The confining pressure oscillated around 18 MPa, which is an expected behavior since the system is manually controlled. On the other hand, the injection pressure was more stable at 10 MPa up to 3.0 hours. After that, a small oscillation can be noticed, and after 5.7 hours, the injection pressure dropped. Figure 4-40 shows the flow of the ISCO pumps and it is possible to note that,

after 5.7 h, they stopped working because the flow increased during the test and the ISCO pumps were not able to maintain the pressure. After around 2 hours of testing, the pumps were demanded too much. It is possible to observe an increase in the number of refill cycles requested by the ISCO pumps (large increase in flow). Therefore, it is likely that the permeability of the specimen increased, maybe associated to wormhole formation, when the test reached 2 hours. The initial flow rate was around 1.0 ml/min, but after 2 hours the flow rate increased, reaching around 6.0 ml/min. It is interesting to recall that the system is controlled by injection pressure, with the possibility of controlling a needle valve at the end of the system to avoid higher flow rate. As previously explained, when one of the pumps empties while the other is not yet refilled, the whole system stops operating. This happened after 5.7 hours of testing.

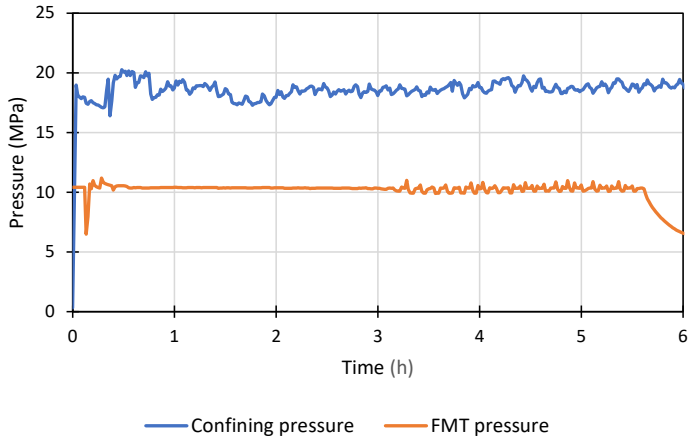

Figure 4-39 – Confining pressure and injection pressure (FMT pressure) during the CO_2 injection test on coquina sample C5.

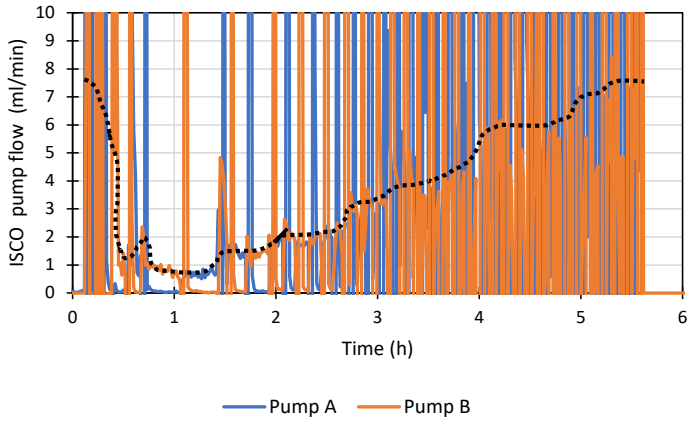

Figure 4-40 – ISCO pumps flow from 0 to 6 hours of the CO_2 injection test on coquina sample C5. The black line is the approximately average flow rate observed.

Figure 4-41 presents the temperature inside and outside the triaxial cell during the test. The temperature seems to follow the room temperature, which is not controlled.

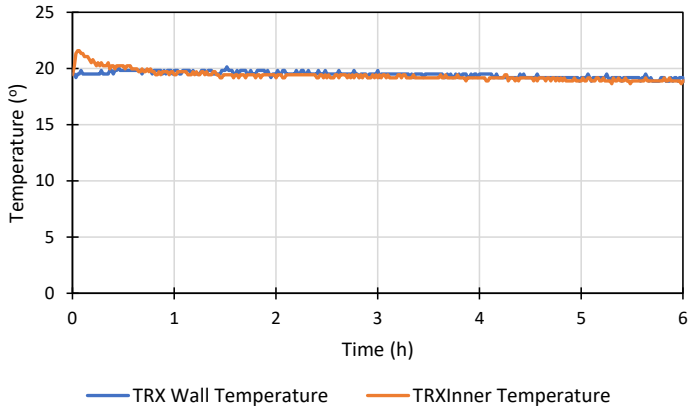

Figure 4-41 – Temperature inside and outside the triaxial cell during the CO_2 injection test on coquina sample.

Axial and radial strains during the first hour of test are presented in Figure 4-42. As expected, when the confining pressure was applied, the axial and radial strains increased and, at around 0.47 h, both strains reduced as a result of the decrease in effective stress. This indicates that 0.47 h was the required time for the solution to penetrate the sample, inducing pore pressure.

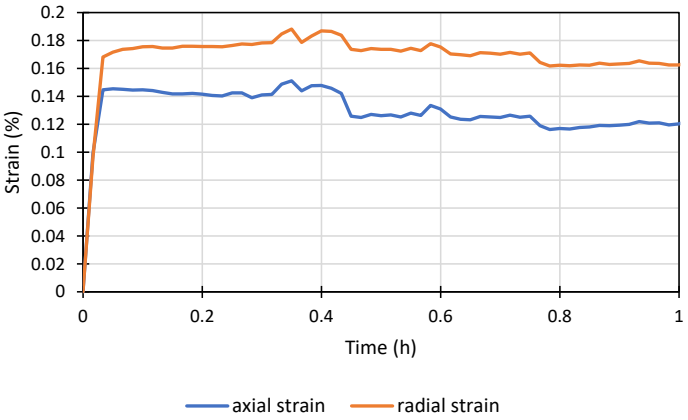

Figure 4-42 – Axial and radial strains during the first hour of CO_2 injection test on coquina sample C5.

Figure 4-43 presents the radial and axial strains, together with the effective stress during the test. The effective stress used in this work is the difference between the confining pressure and the injection pressure. It is important to understand that the injection pressure is the reading of the pressure inside the fluid mixing tank. Therefore, it is not necessarily exactly the pore pressure inside the sample. For instance, at the beginning of the test, when the injection started, the pressure inside the tank was 10 MPa and the confining pressure was 18 MPa, but the actual

effective stress was around 18 MPa, as the solution took time to percolate the sample and induce pore pressure.

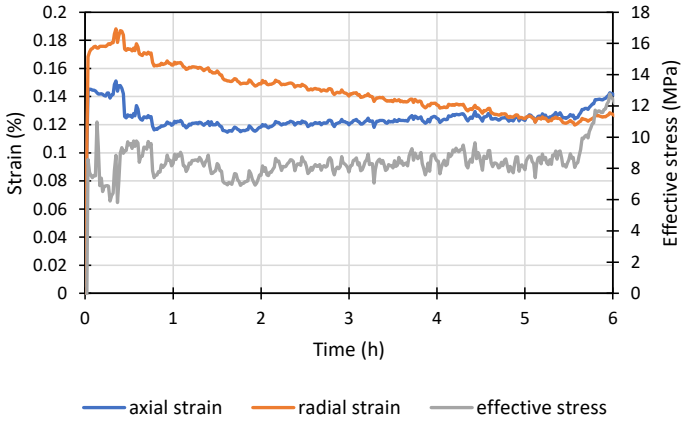

Figure 4-43 – Axial and radial strains together with the effective stress (difference between the confining and the injection pressures) during the CO_2 injection test on coquina sample C5.

From Figure 4-43, it is possible to observe the decrease in the radial strain, while axial strain increases, up to 5.7 hours of testing. At this moment, the injection pressure dropped, increasing the effective stress, and consequently, increasing axial and radial strains.

In addition, compressional and shear wave velocities were also measured in C5 sample. The P and S-wave velocities were measured once every 5 min during the experiment and the results are presented after 0.08, 0.5 and 18 hours of testing. In 0.08 hours, no fluid was percolating the sample, while in 0.5 hours, the CO_2 solution was already flowing through the sample. After 18 hours, the sample was still under CO_2 solution flow, but with a higher porosity due to CO_2 – carbonate rock reaction.

Figure 4-44a presents the P-wave (compressional wave) at 0.08 hours (5 minutes), when only a confining pressure of 18 MPa was applied. Figure 4-44b shows the P-wave at 0.5 hours (30 minutes), when the sample was subjected to 18 MPa of confining pressure and an injection pressure of 10 MPa, and Figure 4-44c presents the P-wave at 18 hours, with confining and injection pressures of 18 MPa and 10 MPa, respectively. In addition, Figure 4-44d shows a zoom on the region of the P-wave curves near the first peak. There was only a small change regarding the arrival time, but a higher variation on the curve amplitudes from the P-waves during the experiment. The highest amplitude reduction is observed from 0.08 hours to 0.5 hours of testing, which indicates that the amplitude was more influenced by sample saturation than by porosity change (from 0.5 hours to 18 hours of testing). This reduction on the amplitudes due to different pore fluids is in accordance with the literature, as shown in Agofack et al. (2018).

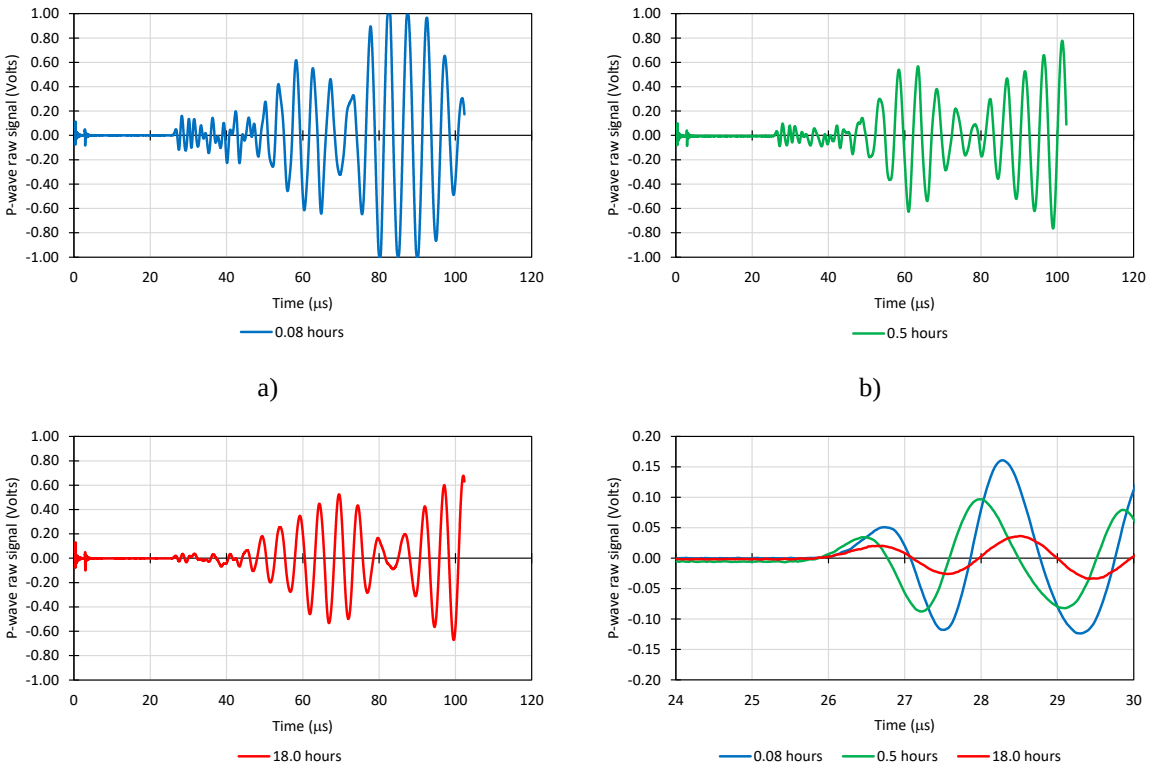

Figure 4-44 – P-wave a) at 0.08 hours, b) 0.5 hours, c) 18 hours of CO_2 injection testing, and d) a zoom in the first peak of these three P waves on coquina sample C5.

The same comparison for the S-wave (shear wave) is shown in Figure 4-45. For the shear wave, it is difficult to obtain the arrival time due to the lower amplitude, and it is harder to get the shear arrival time from the post-dissolution curve as its amplitude gets even lower, almost at the same level as the noise (Figure 4-45d). The same behavior from the P-wave analysis was observed in the S-wave, with lower amplitudes.

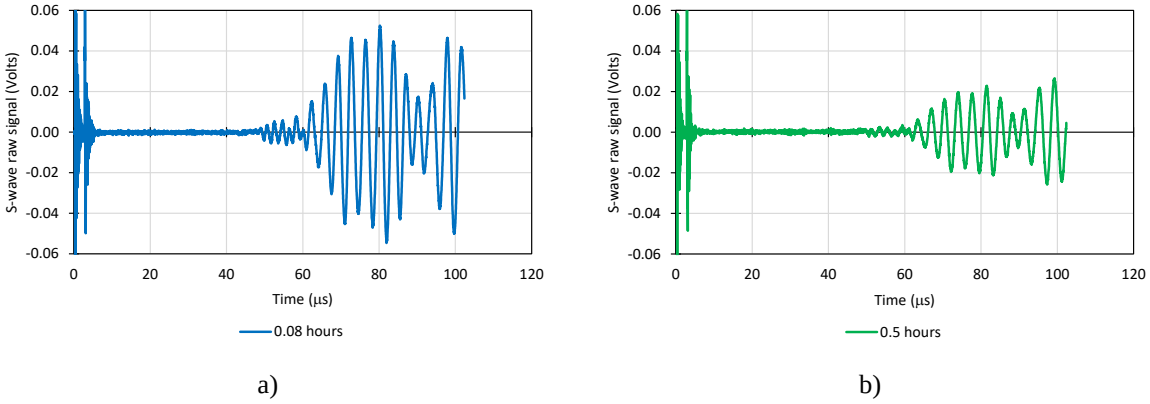

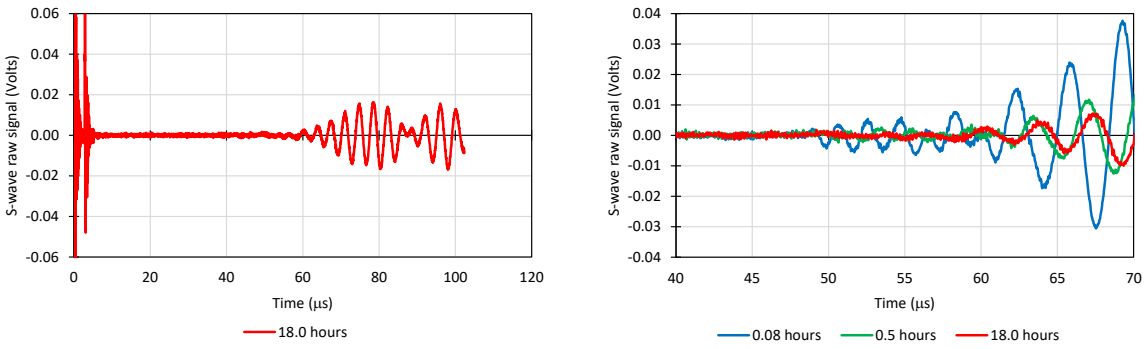

c) d)

Figure 4-45 – S-wave a) at 0.08 hours, b) 0.5 hours, c) 18 hours of CO_2 injection testing, and d) a zoom in the first peak of these three S waves on coquina sample C5.

4.2.2.3. Characterization after acid injection

After the CO_2 solution injection test on coquina C5, the sample was subjected to porosity and permeability measurements at Solintec, a micro CT scan and a multi-stage triaxial test for mechanical characterization. The values obtained for porosity and permeability before and after the injection test is presented in Table 4-6, with a measured permeability higher than the system limit.

Table 4-6 – Properties of sample C5 before and after the CO_2 solution injection test measured by Solintec.

Sample	Permeability (mD)		Porosity (%)	Pore volume (cm^3)	Solid volume (cm^3)
	to Air	Klinkenberg			
C5 (before)	14.48	12.91	11.04	2.76	22.24
C5 (after)	>10.000,00	>10.000,00	15.15	3.70	20.73

From the micro CT scan, Figure 4-46a presents the image of one slice of sample C5 after acid injection without image processing and the binary image from this same slice in Figure 4-46b. In addition, two 3D images of the pore structure of sample C5 before and after the acid injection test are shown in Figure 4-46c and Figure 4-46d for comparison.

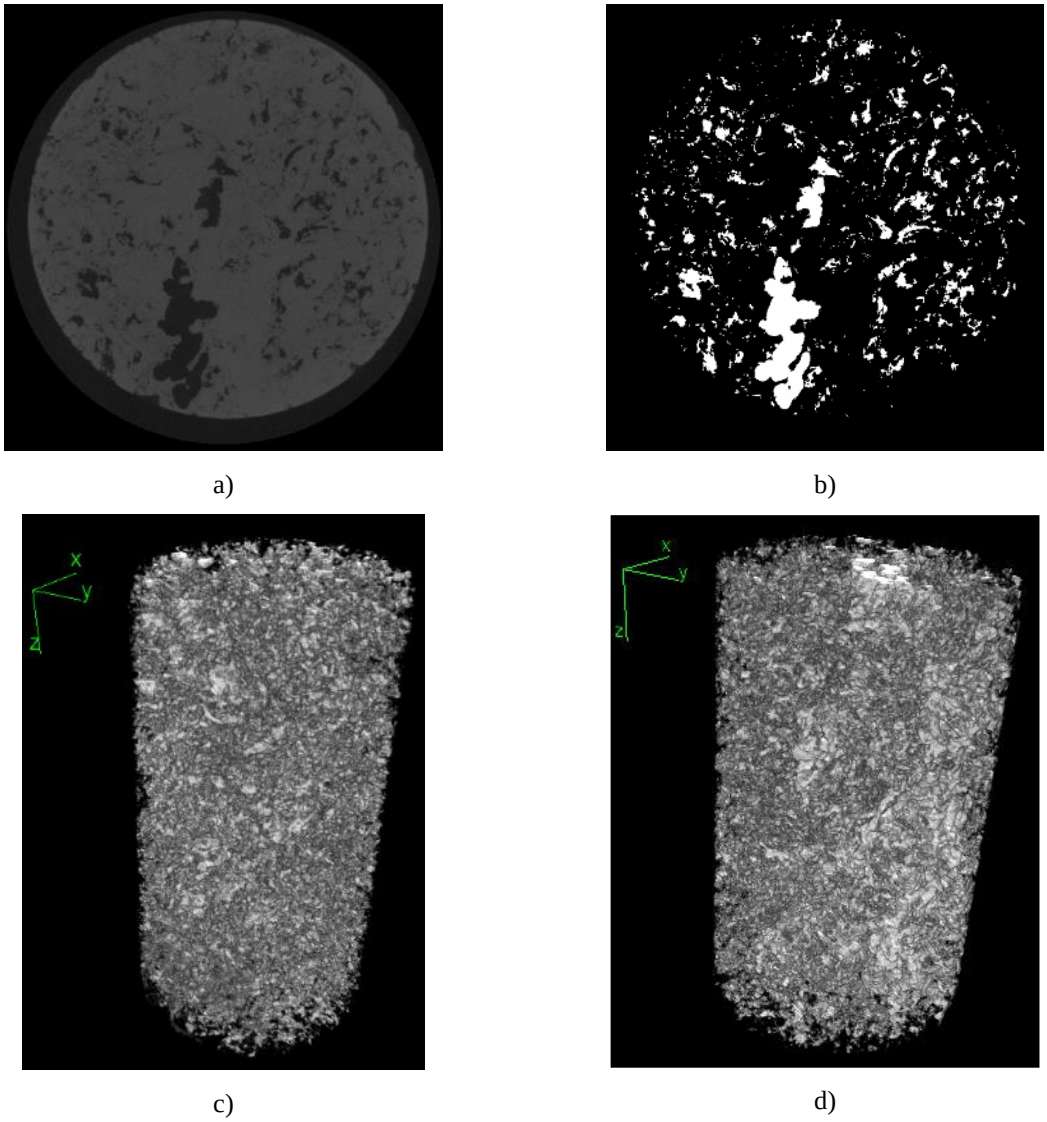

Figure 4-46 – CT scan slice on coquina sample C5 a) without any image processing and b) as binary image after CO_2 injection and 3D image of the pore structure of coquina sample C5 obtained from micro CT scan c) before and d) after acid injection test.

From the CT scan, the average porosity obtained on sample C5 after the CO_2 injection was 12%, again lower than the value obtained from the porosimeter measurement, of 15,15%. As previously mentioned, this was expected, due to the resolution of the micro CT scan, which does not account for pores smaller than 14 μm. Figure 4-47 presents the porosity along sample C5 obtained from CT scan before and after the CO_2 injection. The left side is the top end of the sample, while the right is the bottom end. It is interesting to observe a higher increase in porosity near the bottom of C5, where the fluid was injected into the plug, where porosity increased from around 8% up to 16%. Near the top surface, the porosity increased, but not as much as at the sample bottom.

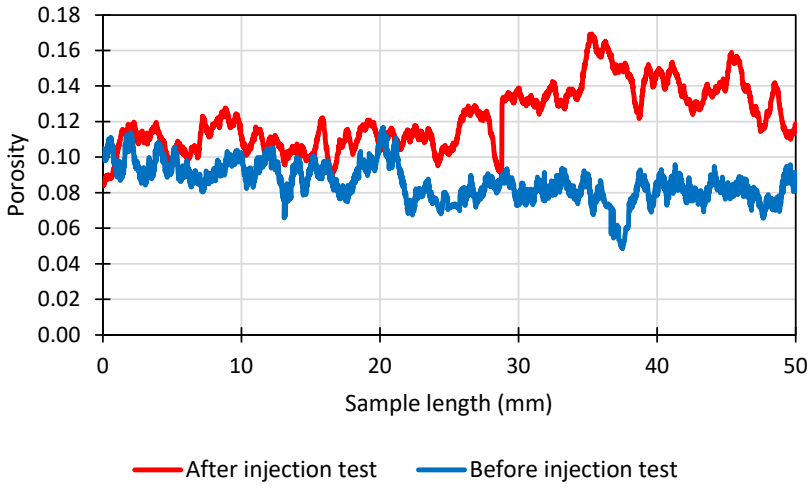

Figure 4-47 – Porosity from the CT scan before (blue) and after (red) CO_2 injection test along coquina sample C5. The left (0 mm) is the top surface of the sample, while the right (50 mm) is the bottom end, where the CO_2 solution was injected.

Figure 4-48 presents the axial strain and radial strain curves obtained for sample C5 after the CO_2 injection test. Regarding the mechanical parameters obtained from this test, UCS, Young's modulus and Poisson's ratio during the first stage are 12.42 MPa, 14.99 GPa and 0.339, respectively. In addition, the peak stresses for the second and third stages are 22.68 MPa and 30.36 MPa, respectively. Regarding the Mohr Coulomb parameters, the cohesion is 3.4 MPa and the friction angle is 41.0º.

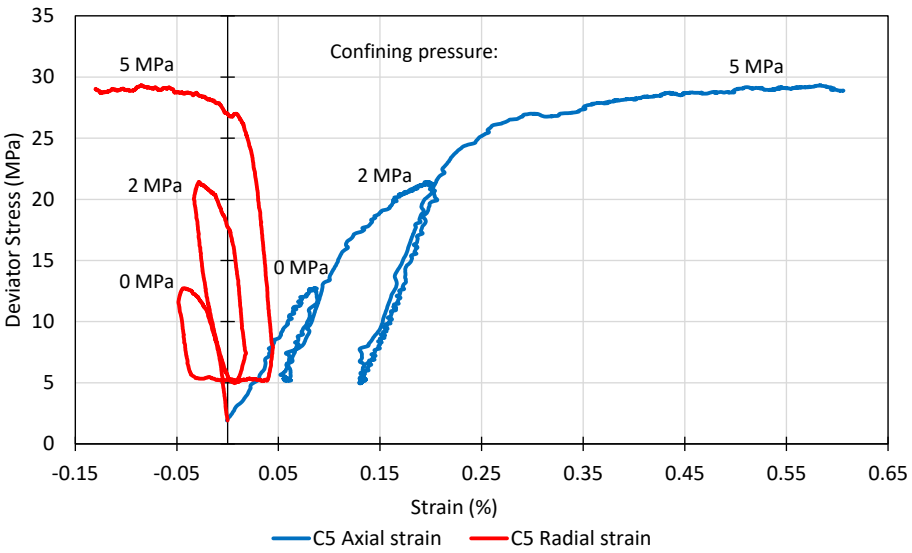

Figure 4-48 – Multi-stage triaxial compressive test (0 MPa, 2 MPa and 5 MPa confining pressures) results for coquina sample C5 after CO_2 solution injection.

A comparison was carried out between the intact samples and the sample subjected to CO_2 injection test. Figure 4-49 shows this comparison regarding the peak deviator stress for

each stage from the multi-stage triaxial test. It is clear the reduced values obtained in C5 (dissolved sample), when compared to the intact sample, B5. The UCS decreased 44% related to B5. For the next stage of confinement (2 MPa), the peak stresses reduced 31% as to B5. For the last stage, with 5 MPa of confining pressure, the peak stress obtained from C5 was 32% lower than the one obtained in the intact sample B5.

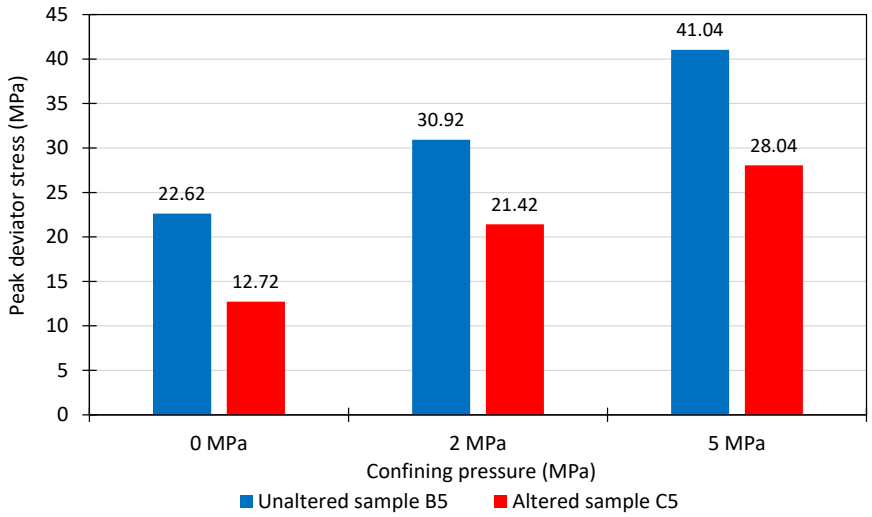

Figure 4-49 – Peak deviator stress for each stage for the coquina intact sample B5 and for altered coquina sample C5.

The Young's moduli from the intact and the dissolved samples are also assessed here, as shown in Figure 4-50. It decreased 64% compared to the unaltered sample.

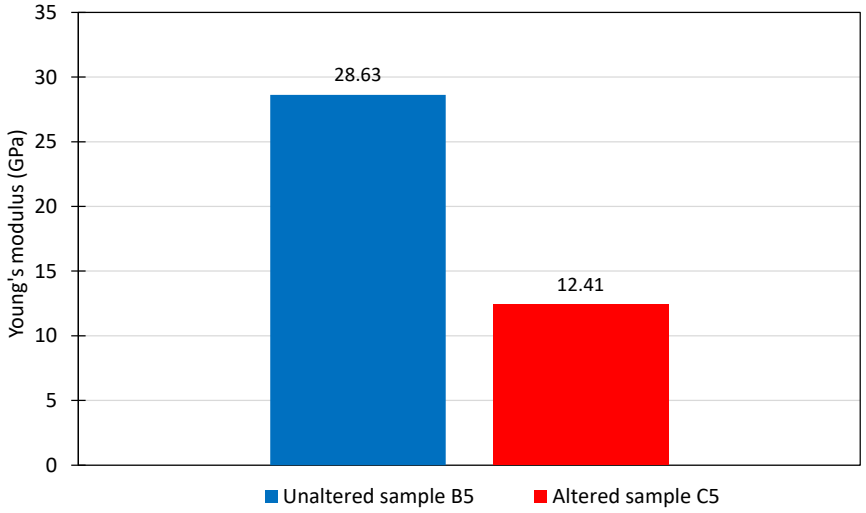

Figure 4-50 – Young's modulus for the coquina intact sample B5 and for altered coquina sample C5.

The Poisson's ratio from unaltered and altered samples were also considered here, in Figure 4-51, with an increase of 14% related to unaltered sample B5. The material degradation observed in the altered coquina sample, C5 when compared to the unaltered sample is higher

than the observed in the Indiana Limestone samples, with a more significant difference on the Young's modulus. This considerable reduction on the coquina Young's modulus is an indicative of a large change on the material pore structure, which result in a higher compaction.

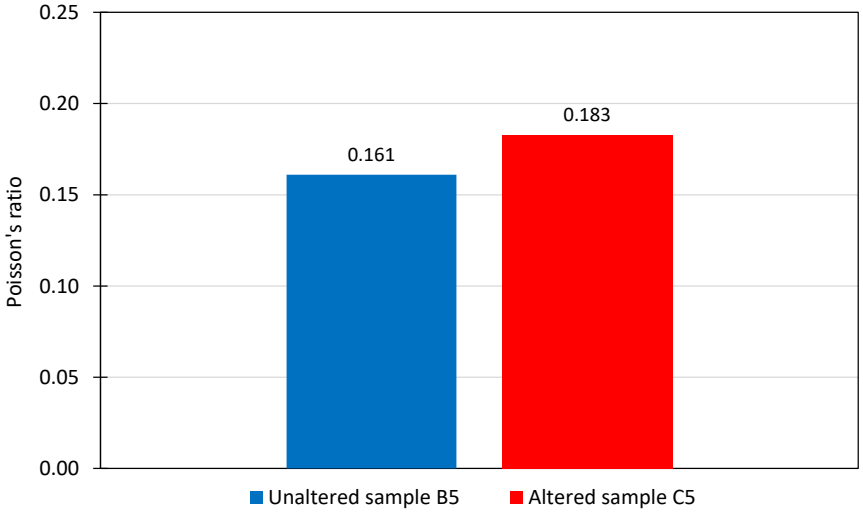

Figure 4-51 – Poisson's ratio for the coquina intact sample B5 and for altered coquina sample C5.

5
Comparing numerical and laboratory results

To study the effects of CO_2 injection into carbonate rocks, coupled laboratory experiments were carried out, considering mechanical, hydraulic and chemical effects. On the other hand, the DEM numerical model was adopted to simulate the mechanical behavior at the sample scale for comparison with the laboratory tests. In order to include the mechanical effects of the CO_2 solution on carbonate rock in the DEM model, a modified bonded contact model was used.

This chapter presents the implementation and validation of the modified DEM contact model to investigate the effects of CO_2 dissolution on the mechanical properties of carbonate rocks. The parameters from the DEM model were calibrated using laboratory experiments.

5.1.
Mechanical calibration and validation

As presented in the previous chapter, a series of laboratory experiments were conducted during this study for the mechanical characterization of the Indiana Limestone. This characterization was used to validate the sample generation procedure and the modified bonded contact model implemented in *Yade*.

The contact model used here is the modified BPM, as described in Sections 3.1.2.1 and 3.2.1. To simulate the uniaxial tests using DEM, facets were included on the top and bottom of the sample (Figure 5-1a). In the triaxial case, the same sample was considered, with the top and bottom facets, but including facets around the sample in order to apply constant pressure to the rock, simulating the confining pressure (Figure 5-1b). The top and bottom facets moved with a pre-defined velocity, compressing the sample. The axial stress was evaluated by summation of the vertical forces acting on the facets and dividing it by the sample cross-section area. The strain was calculated according to the displacement of the blue particles in Figure 5-1a. These blue particles tracking the axial strain were positioned between 15% and 20% and between 80% and 85% of sample height. For the radial strain, the displacements of the red particles from Figure 5-1a were monitored.

The DEM model parameters were adjusted until good agreement was reached when comparing the curves obtained numerically and experimentally from uniaxial, triaxial at 2 MPa confining pressure and tensile tests. Regarding the material tensile strength, the Brazilian

splitting test from the laboratory was used only as an estimate of the tensile strength of this material, as explained in Section 4.1.2.1. Then, the triaxial compressive test at 5 MPa confining pressure was simulated in DEM using the calibrated parameters, and compared with the experimental results for validation.

The DEM parameters obtained by the calibration procedure for the test with Indiana Limestone, as well as the DEM simulation parameters are presented in Table 5-1 and Table 5-2, respectively.

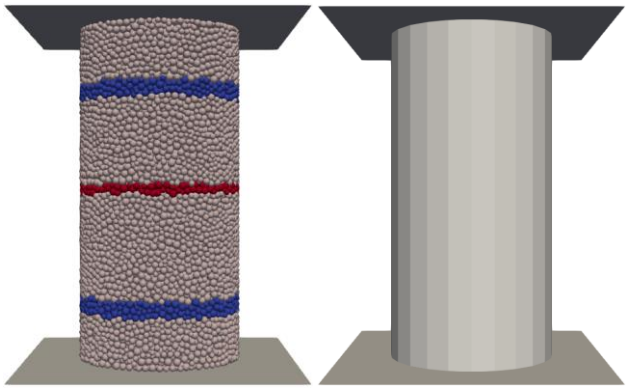

a) b)

Figure 5-1 – Scheme representing the DEM models used in the a) uniaxial compressive test and in the b) triaxial compressive test. The gray plates are the facets used to apply load to the sample. Blue spheres are tracked for axial strain calculations while red spheres are tracked for radial strain.

Table 5-1 – Calibrated DEM contact model parameters for the 42-mm-diameter Indiana Limestone tests.

$\bar{\lambda}$	E (GPa)	$\bar{E}$ (GPa)	ν	$\bar{\nu}$	ϕ (degrees)	$\bar{\phi}$ (degrees)	$\overline{\sigma_C}$ (MPa)	$\overline{\tau_C}$ (MPa)
1.0	7.5	7.5	2.5	2.5	65.0	6.0	1.65	3.30

Table 5-2 – DEM simulation parameters used in the model for the for the 42-mm-diameter Indiana Limestone tests.

R_{min} (m)	R_{max} (m)	Numerical damping	Gravity (m/s^2)	Enlarge Factor	Number of particles
0.0006	0.001	0.4	10.0	1.5	33,318

The results for the uniaxial compressive tests obtained in the numerical model and in the laboratory for the 42 mm samples are presented in Figure 5-2. The results from the DEM simulation and the laboratory tests are in good agreement in both radial strain and axial strain curves.

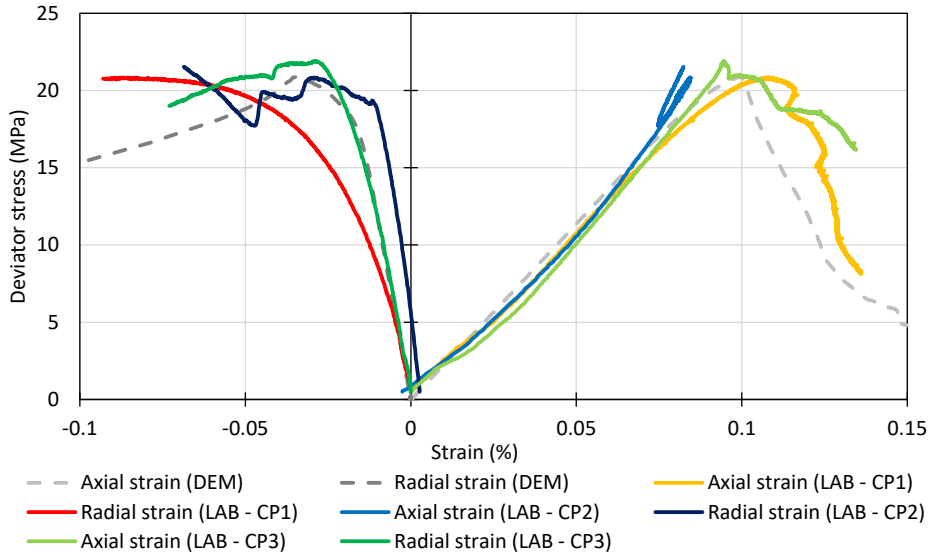

Figure 5-2 – Comparison between laboratory and DEM results for the uniaxial compressive test (zero confining pressure) on Indiana Limestone samples with diameter of 42 mm and height of 84 mm.

From the DEM simulation, it is possible to obtain the number of bonded contacts that broke during the simulation and also the mechanism in which these contacts were broken. In Figure 5-3a, the broken bonds due to tensile breaks (blue) and due to shear breaks (orange) are presented. In addition, Figure 5-3b shows the sample after the uniaxial compressive simulation, with the black lines as the remaining bonded contacts, and Figure 5-3c the Indiana Limestone sample after the experimental uniaxial test. The bonds broke first due to tensile stress at around 0.05% of axial strain, and these breaks increased sharply. Before reaching 0.1% of axial strain, the bonds started to break due to shear stress, and at 0.1% there was an increase on these breaks. This was also the configuration when the sample broke (peak axial stress was reached) and the trend of the tensile breaks curve changed, showing a slower increase of these breaks with respect to the axial strain. It is important to mention that the bonded contact breaks are highly influenced by the adopted DEM contact parameters, specially the ratio of tensile to shear strengths ($\overline{\sigma_C}/\overline{\tau_C}$). The higher number of tensile cracks when compared to the shear cracks in the uniaxial test from laboratory experiments is discussed in Xu et al. (2018).

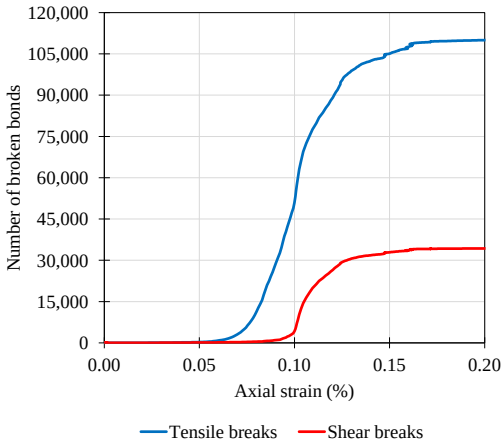

a)

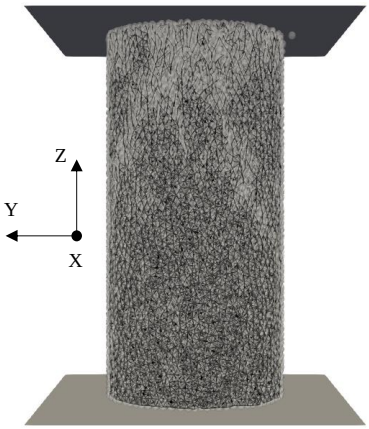

b)

c)

Figure 5-3 – a) Number of broken bonds in the DEM uniaxial test simulation for the Indiana Limestone with diameter of 42 mm and b) remaining bonded contacts in black in the DEM sample after the uniaxial test and c) Indiana Limestone picture after uniaxial test.

Figure 5-4 presents the results obtained by the DEM and by the experimental tests for the triaxial compressive tests at 2 MPa confining pressure. Again, a good agreement is observed between the numerical and the experimental results, specially up to the peak stress. The post peak behavior is slightly different, with the DEM curve decreasing more rapidly. In addition, Figure 5-5a shows the curves from the tensile and shear broken bonds and Figure 5-5b the DEM sample with the remaining bonded contacts after the 2 MPa confining pressure triaxial test. Again, the bonds broke first due to tensile stress, and then due to shear stress, but a higher number of shear breaks is observed when compared with the results from the uniaxial test. For comparison, Figure 5-5c and Figure 5-5d present two photographs of the Indiana Limestone sample after the triaxial test with 2 MPa confining pressure.

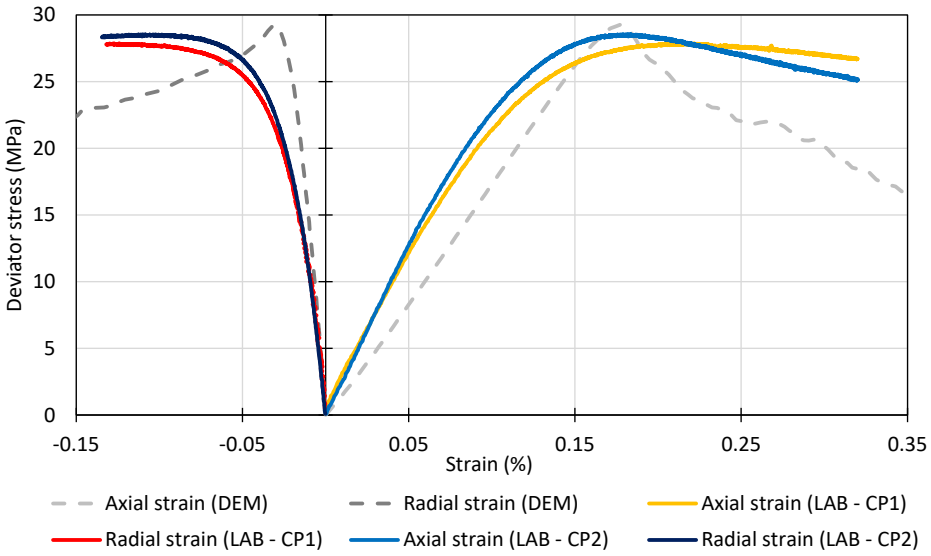

Figure 5-4 – Comparison between experimental and DEM results for the triaxial compressive test with confining pressure of 2 MPa on Indiana Limestone samples with diameter of 42 mm and height of 84 mm.

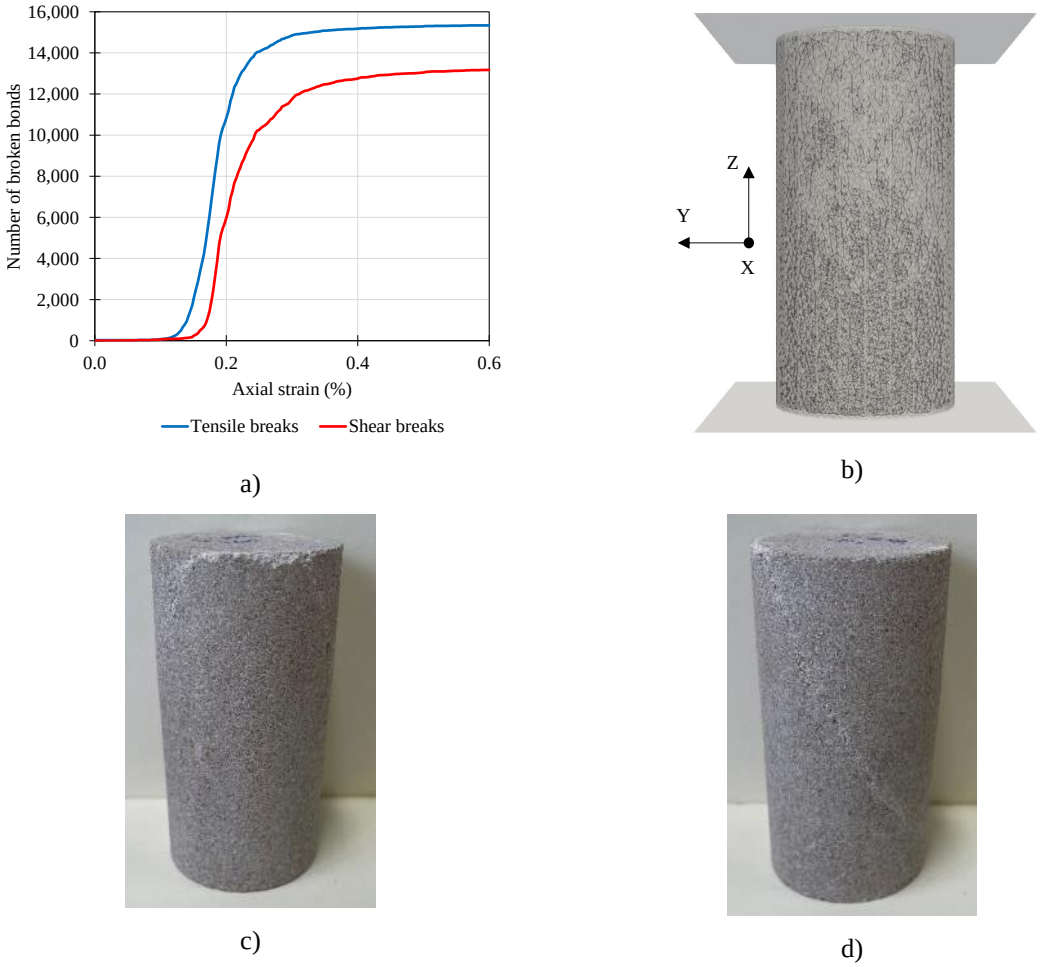

a) b)

c) d)

Figure 5-5 – a) Number of broken bonds during the DEM triaxial test with 2 MPa confining pressure simulation for the Indiana Limestone with diameter of 42 mm, b) remaining bonded contacts in black in the DEM sample

after the triaxial test and c) and d) Indiana Limestone pictures after the triaxial test with 2 MPa confining pressure.

Using the same set of DEM parameters from Table 5-1, the triaxial test at 5 MPa confining pressure was simulated. The comparison between the results from DEM and from the laboratory for this test is used to validate the sample generation methodology and the modified contact model implemented in *Yade* and are shown in Figure 5-6. As previously, the curves obtained from DEM and from the experimental tests show similar behavior. This agreement validates the methodology adopted here for the sample generation and for the contact model. Figure 5-7a also shows the curves from the tensile and shear broken bonds and Figure 5-7b the DEM sample with the remaining bonded contacts after the 5 MPa confining pressure triaxial test. With the increase of confining pressure from 2 MPa to 5 MPa, the number of bonds broken by shear stress increased considerably, surpassing the number of tensile breaks. In addition, Figure 5-7c presents a photograph of the Indiana Limestone sample after the triaxial test under 5 MPa confining pressure. There is no clear fracture on the surface of the sample after the triaxial test under 5 MPa of confining pressure, as opposed to what was observed in the previous tests (uniaxial and triaxial under 2 MPa confining pressure).

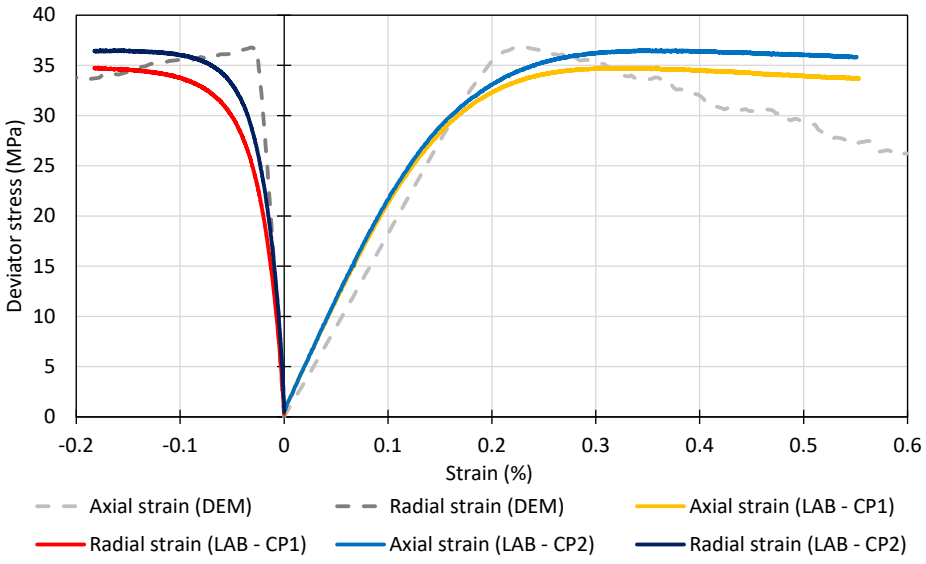

Figure 5-6 – Comparison between laboratory and DEM results for the triaxial compressive test with confining pressure of 5 MPa on Indiana Limestone samples with diameter of 42 mm and height of 84 mm.

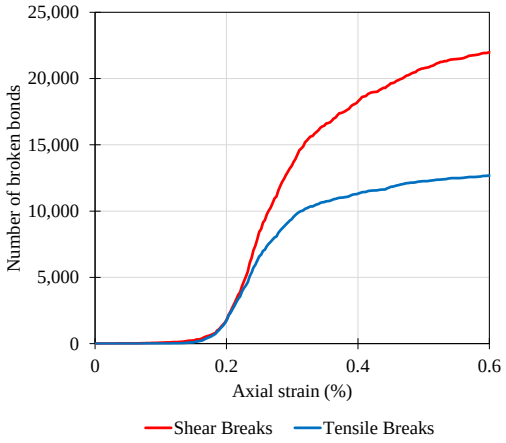

a)

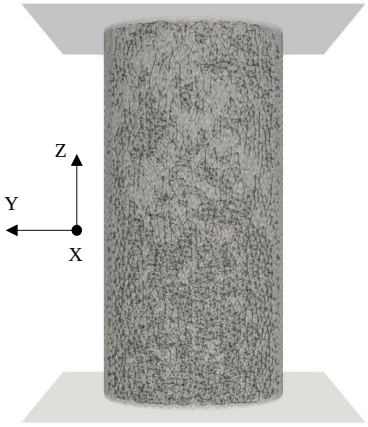

b)

c)

Figure 5-7 – a) Number of broken bonds during the DEM triaxial test with 5 MPa confining pressure simulation for the Indiana Limestone with diameter of 42 mm, b) remaining bonded contacts in black in the DEM sample after the triaxial test and c) Indiana Limestone picture after the triaxial test with 5 MPa confining pressure.

A summary considering the values for the peak axial stresses for the uniaxial and triaxial compressive tests obtained in the laboratory (reference) and in the DEM models are shown in Figure 5-8 and in Table 5-3.

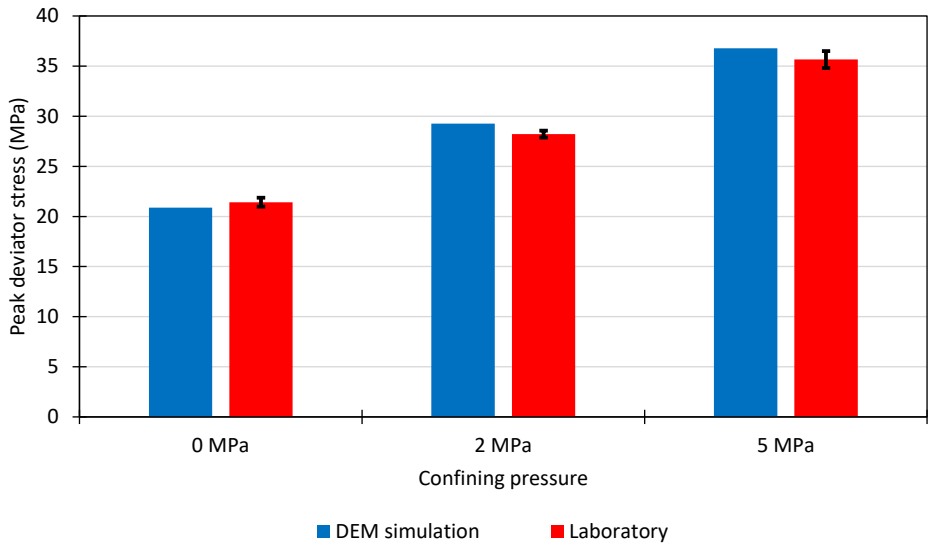

Figure 5-8 – Peak deviator stress for the DEM simulation and for the laboratory tests, considering the uniaxial compressive (0 MPa of confining pressure) and triaxial compressive (2 MPa and 5 MPa of confining pressures) tests for the Indiana Limestone samples with 42 mm in diameter. The standard deviation is presented for the laboratory results by the black markers.

Table 5-3 – Summary of the results obtained from the laboratory experiments and the DEM simulation for the Indiana Limestone samples with 42 mm diameter.

		Lab. average	Lab. stand dev.	DEM
Uniaxial	Strength (MPa)	21.42	0.44	20.87
	E (GPa)	23.46	0.98	22.42
	ν	0.24	0.08	0.195
2 MPa confining pressure	Peak deviator stress (MPa)	28.22	0.34	29.27
5 MPa confining pressure	Peak deviator stress (MPa)	35.66	0.85	36.79

It is important to observe the small variation on the laboratory results, showing that these samples presented a considerably homogeneous behavior, and also a very good agreement when comparing the DEM with the experimental results.

5.2. Mechanical changes due to CO_2 injection test

In addition to the single triaxial tests, a multi-stage triaxial compressive test was also carried out to evaluate how the mechanical properties of the carbonate rocks were affected by the CO_2 solution injection. As discussed in Youn and Tonon (2010), the strength obtained in multi-stage triaxial tests are very close to those obtained in a single triaxial test. Therefore, the

simulation used in the numerical model for the comparison study between the DEM model and the experimental results is the single triaxial test.

5.2.1. Indiana Limestone calibration

Calibration of DEM parameters for the intact Indiana Limestone

This comparison between DEM and laboratory tests were performed for both materials: coquina and Indiana Limestone. First, the results obtained from the Indiana Limestone samples are discussed. In the laboratory experiments, three samples with diameter of 54 mm and height of 108 mm were subjected to the multi-stage triaxial compressive test, as presented in Section 4.1.2.1. Table 5-4 presents the parameters from the DEM contact model adopted after performing the calibration procedure, while Table 5-5 presents the simulation parameters. This procedure was carried out by comparing the results from the DEM simulations with the results from the laboratory tests considering the uniaxial and the 2 MPa confining pressure triaxial tests.

Table 5-4 – Calibrated DEM contact model parameters used in the 54-mm-diameter Indiana Limestone tests.

$\bar{\lambda}$	E (GPa)	$\bar{E}$ (GPa)	ν	$\bar{\nu}$	ϕ (degrees)	$\bar{\phi}$ (degrees)	$\overline{\sigma_C}$ (MPa)	$\overline{\tau_C}$ (MPa)
1.0	9.0	9.0	2.0	2.0	65.0	11.0	2.00	4.90

Table 5-5 – DEM simulation parameters used in the 54-mm-diameter Indiana Limestone tests.

R_{min} (m)	R_{max} (m)	Numerical damping	Gravity (m/s^2)	Enlarge Factor	Number of particles
0.0006	0.001	0.4	10.0	1.5	70,848

The results from these three samples were compared to the DEM simulation of the uniaxial compressive test in Figure 5-9. In addition, the values of the peak deviator stress (MDS), Young's modulus (E) and Poisson's ratio (ν) from the laboratory and the DEM were compared.

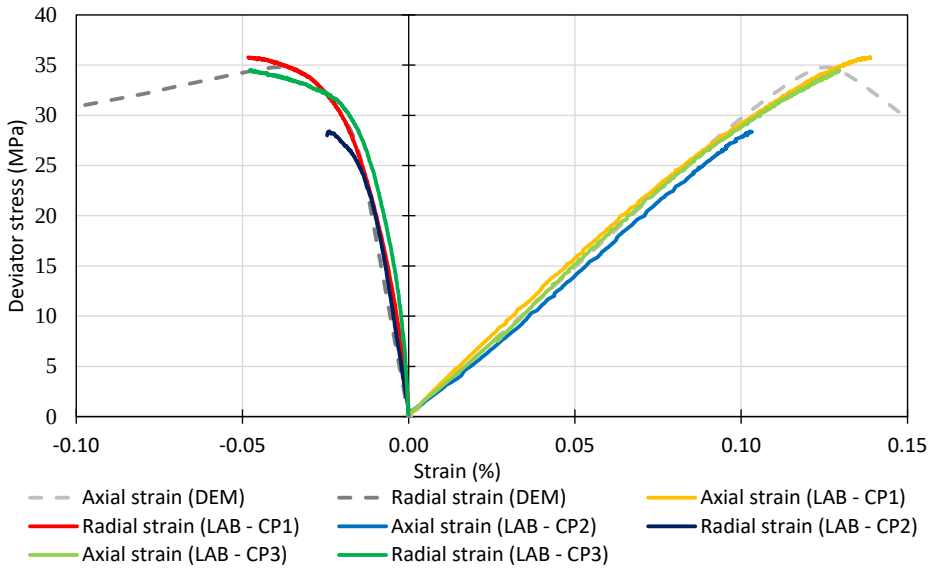

Figure 5-9 – Comparison between DEM and laboratory experiment for the uniaxial compressive test on Indiana Limestone samples.

Both the axial strain and the radial strain curves from the DEM simulation are in great agreement with the ones from the laboratory for the uniaxial compressive test. The average UCS obtained from the laboratory tests was 32.90 $\pm$ 3.22 MPa, while the one obtained from the DEM was 34.79 MPa. The average Young's modulus and the average Poisson's ratio from the experimental tests were 30.87 $\pm$ 1.31 GPa and 0.15 $\pm$ 0.01, respectively, while for the DEM simulation, they were 29.81 GPa and 0.166, respectively, showing good agreement between numerical and experimental results.

The same comparison was also carried out with the results from the triaxial compressive test at 2 MPa confining pressure, presented in Figure 5-10. For this comparison, the peak deviator stress was compared between the average value from the laboratory and the value from the DEM simulation. From the experiments, the average peak deviator stress was 45.08 $\pm$ 1.52 MPa, while for DEM, it was 43.97 MPa.

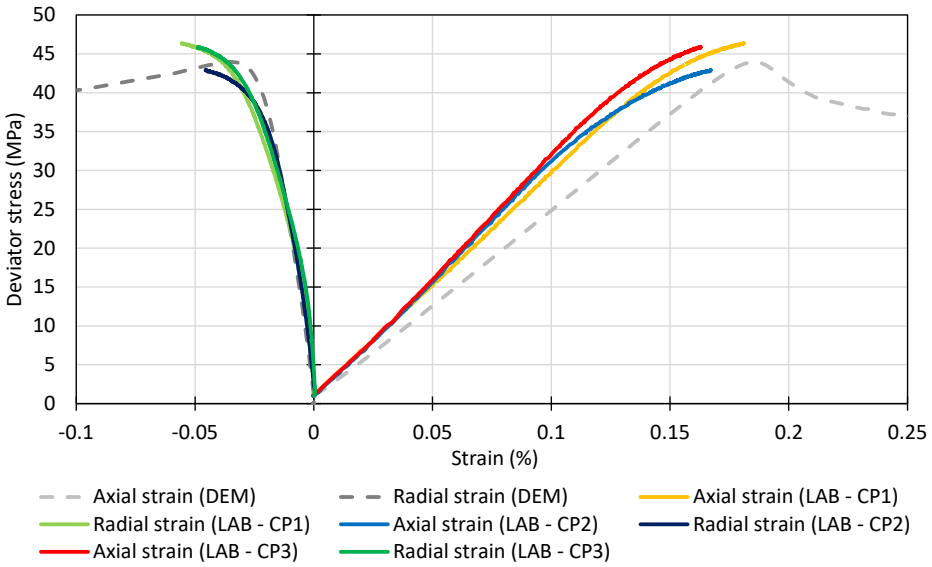

Figure 5-10 – Comparison between DEM and laboratory experiment for the 2 MPa confining pressure triaxial compressive test for the Indiana Limestone samples.

In addition, Figure 5-11 presents the comparison between the results from the triaxial compressive test with 5 MPa confining pressure from the laboratory and the DEM. The results were also in good agreement, considering the axial strain and radial strain curves. The average peak deviator stress obtained from the laboratory test was 55.63 $\pm$ 1.80 MPa, while from the DEM test, it was 54.63 MPa.

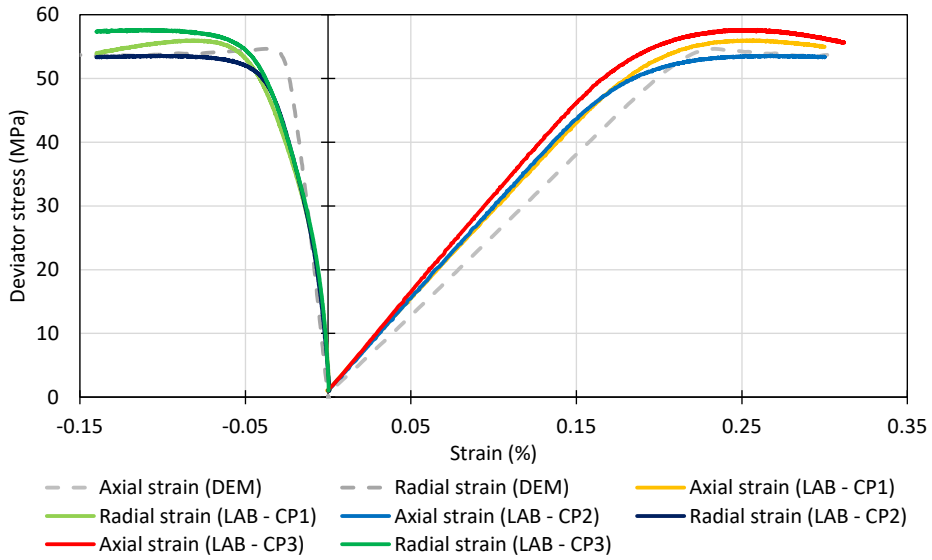

Figure 5-11 – Comparison between DEM and laboratory experiment for the 5 MPa confining pressure triaxial compressive test for the Indiana Limestone samples.

Figure 5-12 shows a result summary considering the average laboratory results and the DEM simulation result for the peak stress in each stage of the triaxial test.

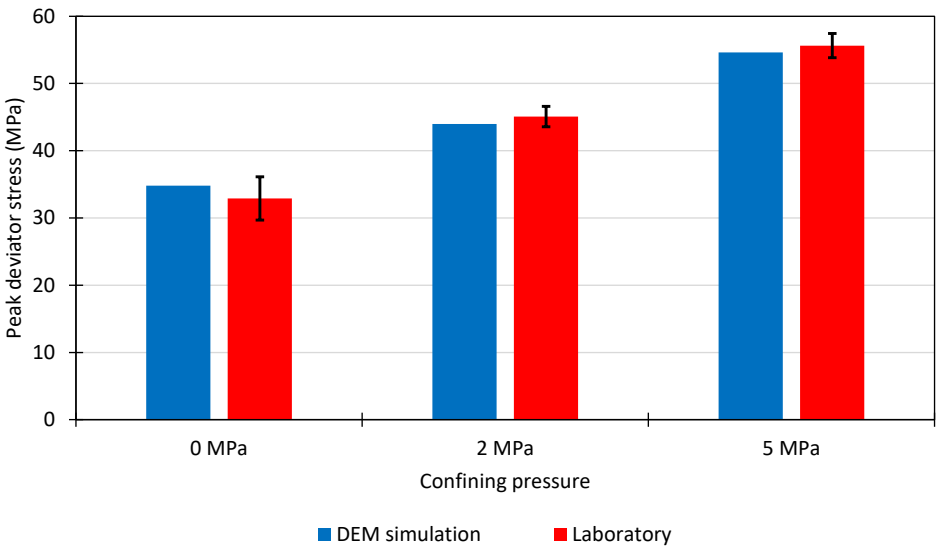

Figure 5-12 – Peak deviator stress for the DEM simulation and for the laboratory tests, considering the uniaxial compressive (0 MPa of confining pressure) and triaxial compressive (2 MPa and 5 MPa of confining pressures) tests for the Indiana Limestone samples with 54 mm in diameter. The standard deviation is presented for the laboratory results by the black markers.

Calibration of $\bar{\lambda}$ for the altered Indiana Limestone

The next step is to calibrate parameter $\bar{\lambda}$ to match the uniaxial test curve from the DEM model with the one from laboratory after subjected to a CO_2 solution injection. Then, this same DEM sample is subjected to the triaxial compressive tests with 2 MPa and 5 MPa of confining pressure, and the results are compared with the results from the multi-stage triaxial test in the laboratory for validation. The values of $\bar{\lambda}$ after calibration for each sample are shown in Table 5-6.

Table 5-6 – Values of $\bar{\lambda}$ after calibration for Indiana Limestone samples P03, P04 and P05 after the injection of CO_2 solution and the value adopted for the intact samples.

Intact	P03	P04	P05
1.00	0.89	0.79	0.85

Figure 5-13 presents the results for the uniaxial compressive tests from the Indiana Limestone samples (P03, P04 and P05) used for calibration, and the curves obtained from the DEM models. There is a great agreement between the numerical and experimental results, regarding the axial strain and radial strain curves, and the peak deviator stress.

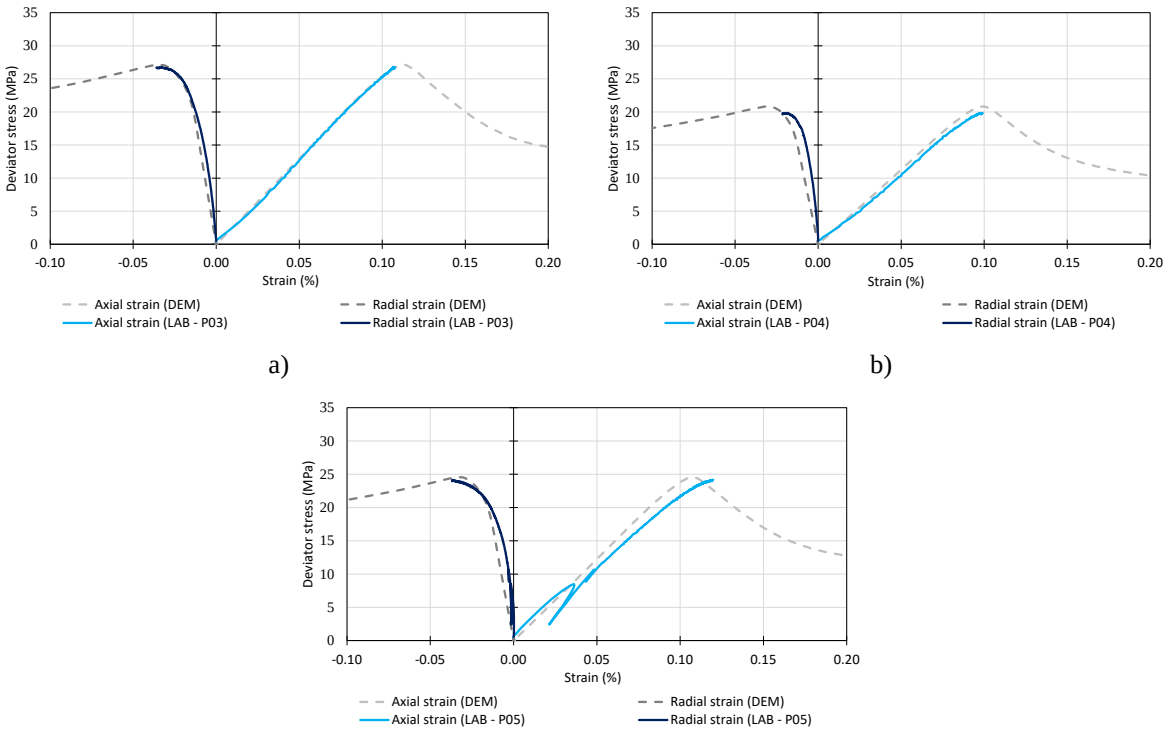

Figure 5-13 – Comparison among the results for the uniaxial compressive test carried out on Indiana Limestone samples a) P03, b) P04 and c) P05 after CO_2 injection in the laboratory and in DEM simulations.

In Figure 5-14, the curves from the second stage (2MPa confining pressure) of the multi-stage triaxial test in the laboratory and the curves obtained from the DEM simulations of the triaxial test with a confining pressure of 2 MPa are presented. The agreement among the curves shows that all model parameters, including $\bar{\lambda}$ were calibrated accurately. When assessing sample P04, it is observed that the peak deviator stress from the DEM curve is below the corresponding value from the laboratory. This difference is around 10%, which is assumed here acceptable for this numerical model, following Wang and Cao (2017).

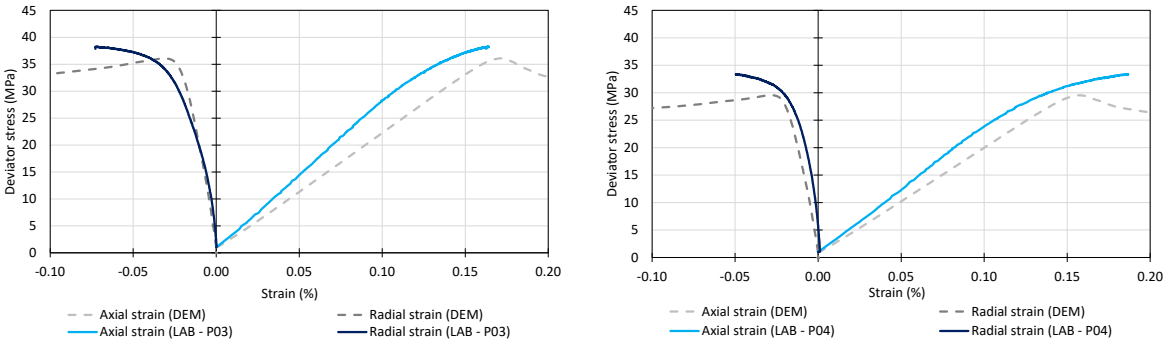

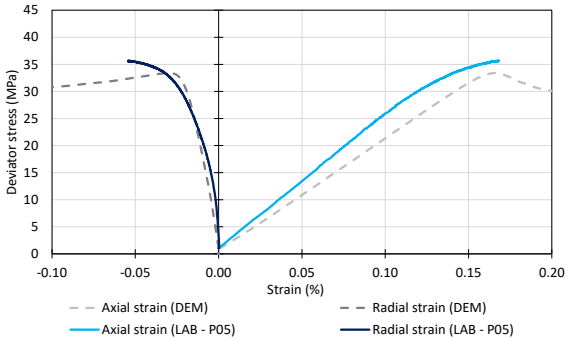

c)

Figure 5-14 – Comparison among the results for the triaxial compressive test with 2 MPa of confining pressure carried out on Indiana Limestone samples a) P03, b) P04 and c) P05 after CO_2 injection in the laboratory and in DEM simulations.

Also for validation purpose, the results from the third stage of the multi-stage triaxial tests are compared with the DEM results for the triaxial test with 5 MPa of confining pressure, as shown in Figure 5-15. Very good agreement among the numerical and experimental curves for all the altered samples is observed. There is a slight difference on the post-peak behavior, when comparing the DEM and the laboratory results. The DEM curves from the intact Indiana Limestone also presented this difference on the post-peak behavior. More effort could be spent on the calibration procedure, but we assumed we reached a good trade-off between computational time and accuracy in this thesis for this calibration.

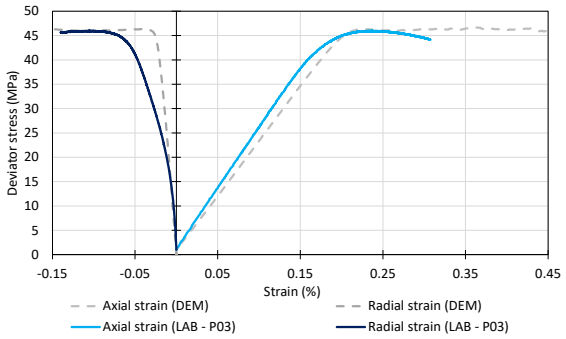

a)

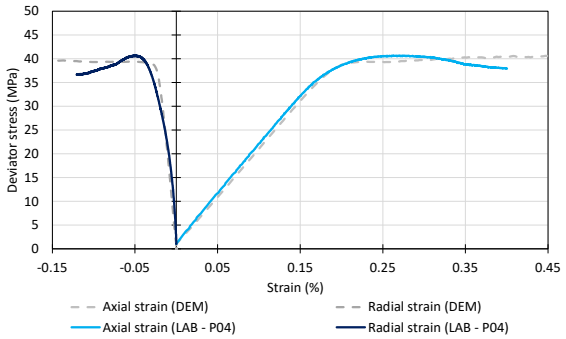

b)

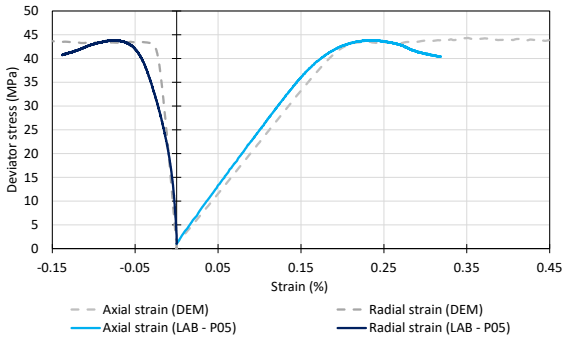

c)

Figure 5-15 – Comparison among the results for the triaxial compressive test with 5 MPa of confining pressure carried out on Indiana Limestone samples a) P03, b) P04 and c) P05 after CO_2 injection in the laboratory and in DEM simulations.

5.2.2. Coquina calibration

Calibration of DEM parameters for the intact coquina

The same comparison among the laboratory tests and DEM simulation was carried out considering the coquina samples. For that, a calibration procedure was needed and the parameters for the DEM contact model used for the coquina samples are presented in Table 5-7, while the simulation parameters are shown in Table 5-8.

Table 5-7 – Calibrated DEM contact model parameters used in the coquina tests.

$\bar{\lambda}$	E (GPa)	$\bar{E}$ (GPa)	ν	$\bar{\nu}$	ϕ (degrees)	$\bar{\phi}$ (degrees)	$\overline{\sigma_c}$ (MPa)	$\overline{\tau_c}$ (MPa)
1.0	9.2	9.2	1.88	1.88	65.0	6.0	1.10	4.10

Table 5-8 – DEM simulation parameters used in the comparison between numerical and experimental results for the coquina samples.

R_{min} (m)	R_{max} (m)	Numerical damping	Gravity (m/s^2)	Enlarge Factor	Number of particles
0.00035	0.0006	0.4	10.0	1.5	33,368

Figure 5-16 presents the comparison for the first stage, when no confining pressure was applied to the sample. In addition, the values of UCS, Young's modulus and Poisson's ratio were compared. The UCS from the unaltered sample B5 was 22.62 MPa, while from DEM, it was 22.60 MPa. For the Young's modulus, B5 was 28.63 GPa and DEM sample was 30.18 GPa. Regarding Poisson's ratio, the values for the unaltered sample and from DEM samples were 0.161.

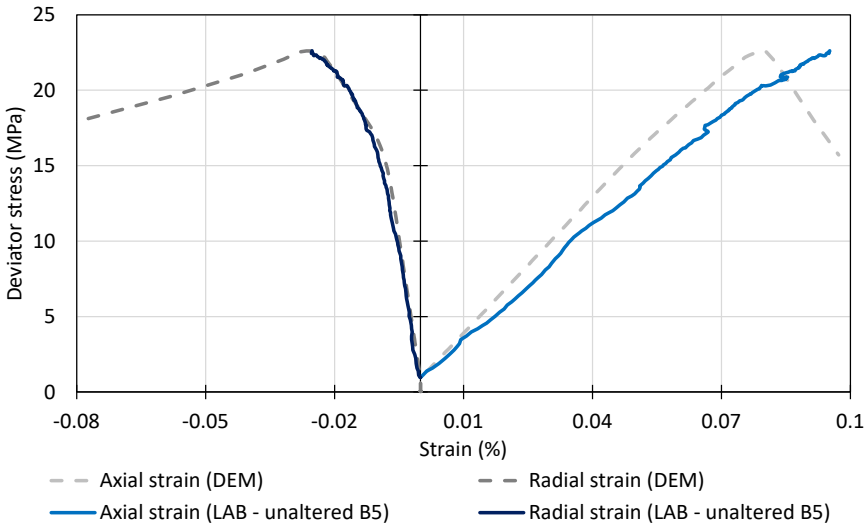

Figure 5-16 – Comparison among the results for the uniaxial compressive test carried out on intact coquina samples in the laboratory and in DEM simulation.

Great agreement between the DEM and the experimental results was reached for both the radial strain and axial strain curves.

The comparison for the second stage of the test, when a 2 MPa confining pressure was applied to the sample is shown in Figure 5-17. During this stage, the peak deviator stress for the unaltered sample B5 was 30.92 MPa and the corresponding value in the DEM simulation was 31.62 MPa.

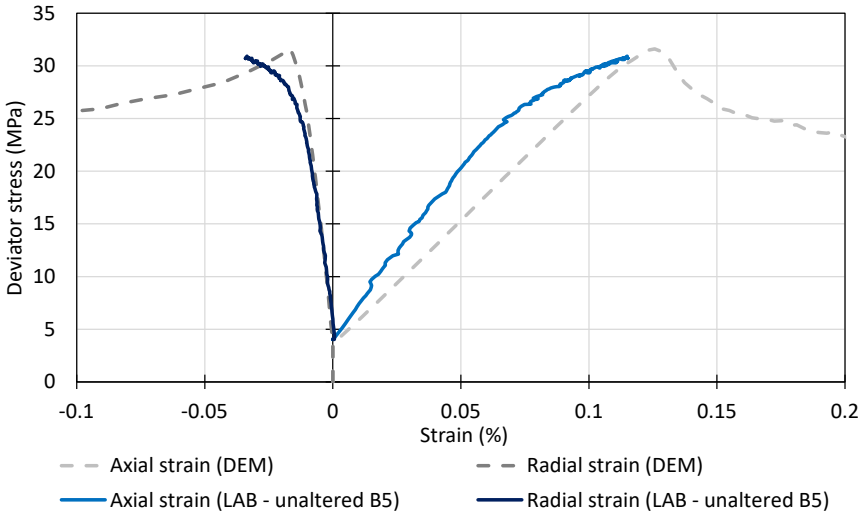

Figure 5-17 – Comparison among the results for the triaxial compressive test at 2 MPa confining pressure carried out on intact coquina samples in the laboratory and in DEM simulation.

Again, good agreement is observed between the numerical and experimental curves. As described in the multi-stage procedure in Section 4.2.1.1, the unloading step ends when a deviator load of 2 kN (deviator stress of 4 MPa) is reached in the coquina samples. This was

performed to ensure that the piston was still in contact with the sample during the confining pressure raise in the following step. In addition, the axial and radial strains were set to zero before starting the deviatoric loading. Therefore, it can be observed that the curves start at a stress deviator of 4 MPa with zero strains.

The last stage from the test is presented in Figure 5-18. In this stage, there was a 5 MPa of confining pressure applied to the sample. The results obtained from the comparison between the numerical and experimental curves are very good. In addition, the peak deviator stress was compared, with values of 41.04 MPa for unaltered sample and 38.82 MPa for the DEM simulation.

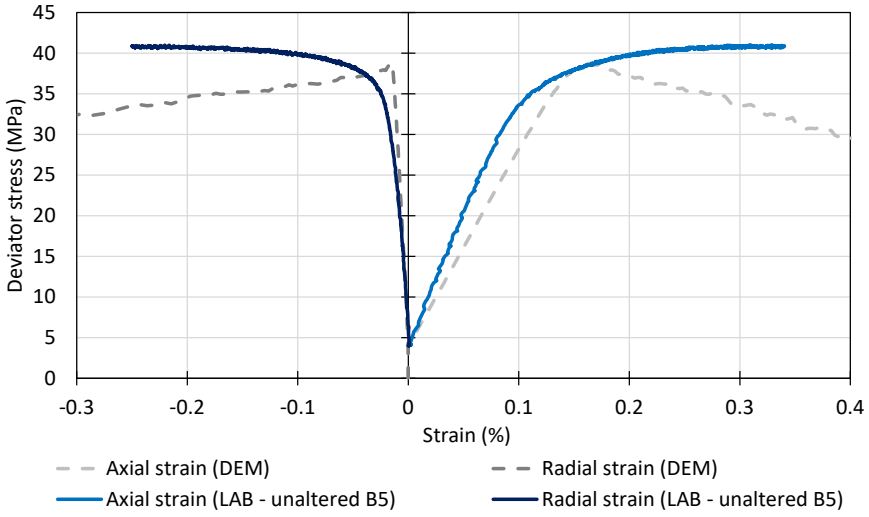

Figure 5-18 – Comparison among the results for the triaxial compressive test at 5 MPa confining pressure carried out on intact coquina samples in the laboratory and in DEM simulation.

A summary of the main results obtained from the comparison between the laboratory and the numerical results with the coquina intact samples is presented in Figure 5-19.

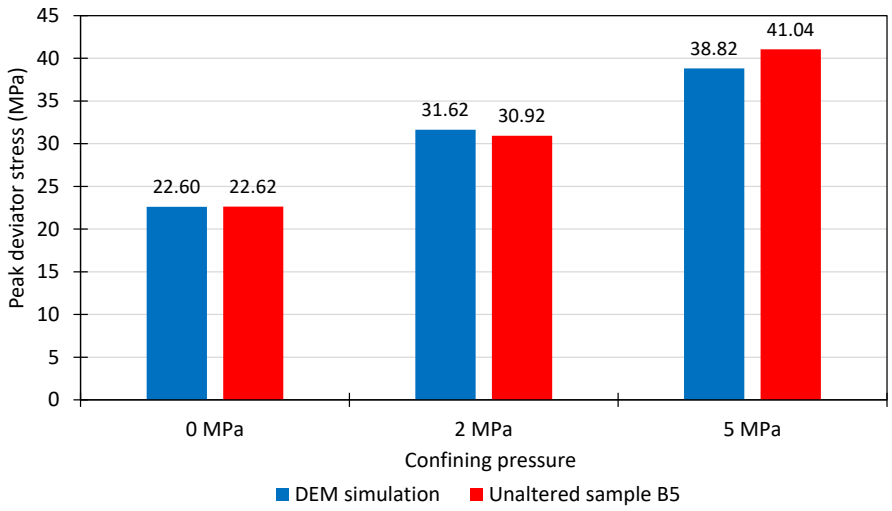

Figure 5-19 – Peak deviator stress for the DEM simulation and for the laboratory test, considering the uniaxial compressive (0 MPa of confining pressure) and triaxial compressive (2 MPa and 5 MPa of confining pressures) tests for the unaltered coquina sample.

The agreement between the numerical and experimental results for all three stages of testing validate the methodology used in the DEM simulation (calibration, sample preparation and contact model implementation).

Calibration of $\bar{\lambda}$ for the altered coquina

Here, $\bar{\lambda}$ was calibrated with the results obtained from the first stage of the multi-stage triaxial test (uniaxial test), as presented in Figure 5-20, and the value obtained for $\bar{\lambda}$ was 0.775. The UCS from the laboratory was 12.72 MPa, with Young's modulus of 12.41 GPa and a Poisson's ratio of 0.183. These same parameters obtained from the DEM simulation were 12.74 MPa, 21.81 GPa and 0.241, respectively. It is observed that the UCS obtained from the numerical and experimental tests are in great agreement, while the Young's modulus and the Poisson's ratio are not. These higher differences in Young's modulus and Poisson's ratio are mainly due to material pore structure. For the Indiana Limestone samples, the degradation observed was smaller than the one in the coquina sample. In the coquina sample, the Young's modulus was highly impacted by the CO_2 injection test, as the porosity increased considerably. Vajdova et al. (2004) tested three kinds of carbonate rocks, Indiana limestone, Tavel limestone and Solnhofen limestone in triaxial tests. The influence of the porosity over elastic, inelastic and failure properties of the tested rocks was clear. This higher porosity increase is not fully considered in the numerical model, once it only affects the size of the bonded contacts, and not the particle sizes.

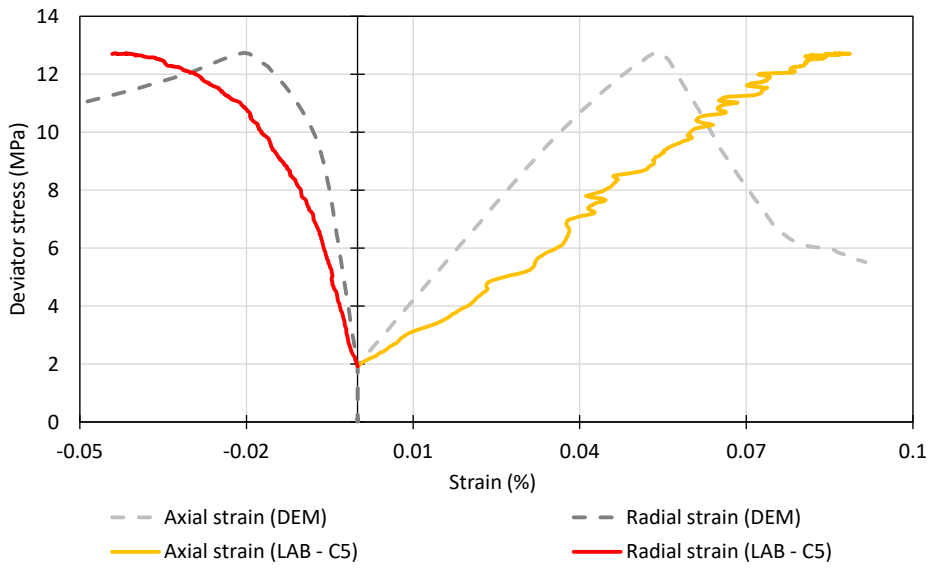

Figure 5-20 – Comparison among the results for the uniaxial compressive test carried out on C5 coquina sample after CO_2 injection in the laboratory and in DEM simulation considering $\bar{\lambda}$ = 0.775.

Then, to validate the numerical model, a comparison among the laboratory results from the multi-stage triaxial tests and the DEM simulations for the 2 MPa and 5 MPa confining pressures are presented in Figure 5-21 and Figure 5-22, respectively.

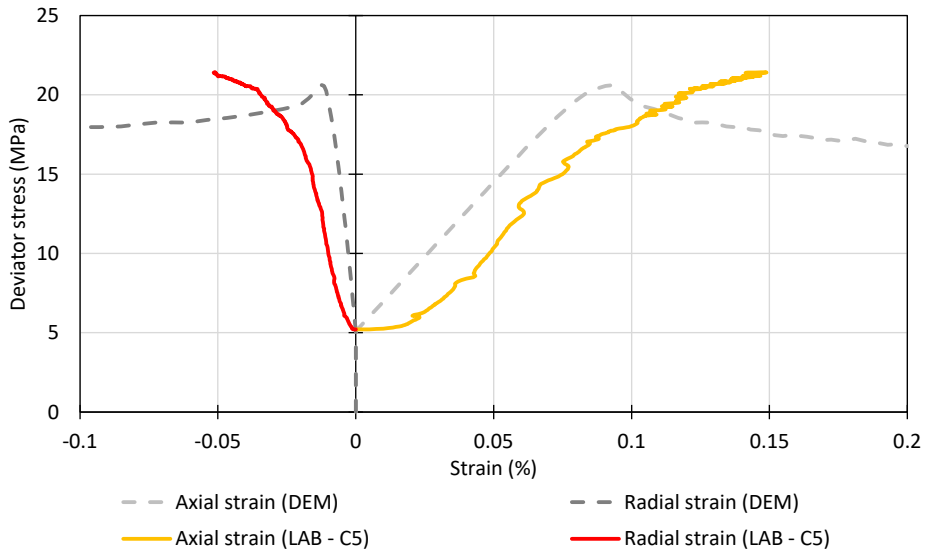

Figure 5-21 – Comparison among the results for the triaxial compressive test with 2 MPa of confining pressure carried out on C5 coquina sample after CO_2 injection in the laboratory and in DEM simulation considering $\bar{\lambda}$ = 0.775.

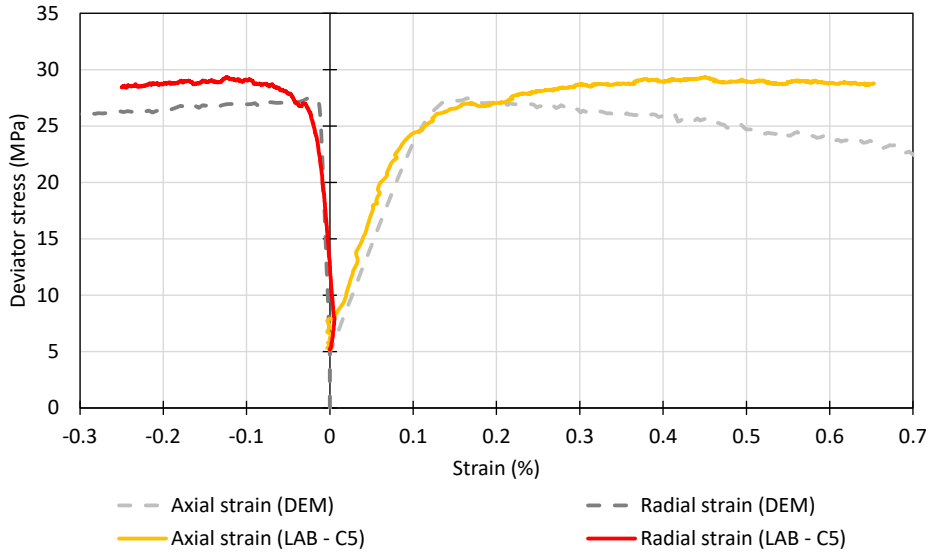

Figure 5-22 – Comparison among the results for the triaxial compressive test with 5 MPa of confining pressure carried out on C5 coquina sample after CO_2 injection in the laboratory and in DEM simulation considering $\bar{\lambda}$ = 0.775.

The curves from the laboratory results are in good agreement with the ones from the DEM simulations for the coquina sample. This contributes to the validation of the methodology used for the DEM modeling. In addition, the agreement among the numerical and experimental results also shows that this methodology can be applied to other materials besides the Indiana Limestone. On the other hand, the assumptions for considering the mechanical degradation on the DEM model must be considered when comparing with the laboratory results. The main assumption that may limit the use of this model is that it only changes the bond contact size, not the particle size. This may result in different behaviors when comparing the numerical and experimental results from samples subjected to a very high porosity change.

6
Conclusions

In this thesis, a study of the mechanical effect of CO_2 solution on carbonate rocks was developed, by performing experimental tests and numerical simulations using the Discrete Element Method (DEM). To perform DEM simulations, a workflow was proposed following some crucial steps, such as the definition of contact model, sample preparation and parameters calibration. For the contact model, a modification of the Bonded Particle Model was implemented in the open-source software *Yade* to consider the material mechanical degradation. New methodology for sample preparation was developed, focusing on creating compact models with good model resolution to accurately simulate rock behavior with less computational effort. For parameter calibration, this study brings the application of genetic programming to increase the accuracy of the calibration procedure, while reducing computational time. Then, a laboratory workflow was designed to improve the understanding on the interaction between CO_2 and carbonate rocks, while using the experimental results for numerical calibration and validation. First, samples were subjected to mechanical tests, optical microscopy, tomography scans, and porosity and permeability measurements for characterization purposes. Then, CO_2 solution injection tests were performed under certain pressure and temperature conditions. Afterwards, samples subjected to this CO_2 injection were again characterized.

The entire numerical workflow presented here for the DEM model was validated with the experimental results. The contact model implementation was calibrated and validated with mechanical tests carried out on Indiana Limestone samples, and the mechanical properties, as well as the axial strain and radial strain curves showed very good agreement between numerical and experimental results. Regarding sample preparation, a model resolution of 26 showed small variances on the uniaxial test simulation results when considering different realizations, while keeping computational efficiency. In addition, it was confirmed that sample structure created using Packgen and compaction was able to reproduce the mechanical rock behavior observed in uniaxial and triaxial compressive tests. The calibration procedure using genetic programming also showed small differences between estimated values and target ones using data sets with 30 models, indicating that GP can be a good candidate to DEM calibration. For

the last step of the workflow, parameter $\bar{\lambda}$ could be successfully used to consider the mechanical effect of the CO_2 injection on the carbonate rocks, reflecting the changes on the material mechanical properties observed in the laboratory. This numerical workflow was applied to two different materials: Indiana Limestone and coquina, with both showing good agreement between numerical and experimental results. In addition, the DEM also reflected the expected particle structure behavior, according to the literature, when observing the breaks on the bonded contacts due to tensile and shear stresses.

From the experimental workflow, the mechanical properties of the carbonate rocks were successfully obtained before and after the CO_2 injection test for Indiana Limestone and coquina samples. Microscope images obtained from the bottom and top surfaces of the carbonate samples indicate a porosity increase due to the injection of CO_2 solution. Five CO_2 injection tests were carried out, and the porosity alterations were different for each tested sample. Among these five samples, three of them were subjected to the same test conditions, regarding confining and injection pressures and temperature. Even these three samples had different variation on their surface porosity. This difference is probably due to the different flow rates of CO_2 solution and the total time in which the CO_2 solution flowed through the samples. The GCTS creep with CO_2 injection testing system allows for injection pressure control. Therefore, as dissolution takes place, flow rate changes, resulting in different dissolution rates. A porosity increase was also observed on the coquina sample C5. In this case, the increase was observed from the tomography scans (from ≈9% to ≈12%) and the porosimeter measurement (from ≈11% to ≈15%) carried out before and after the injection of CO_2 solution. The changes on the pore structure from the carbonate rocks significantly influenced their mechanical behaviors. This influence can be observed when comparing the peak stresses and Young's modulus obtained from the multi-stage triaxial tests on intact samples with those from samples subjected to CO_2 solution injection. For the Indiana Limestone samples, the change on the peak stresses varies from 15% (sample P03) up to 40% (sample P04), while for Young's modulus, the reduction is between 16% (sample P03) and 28% (sample P04). Regarding the coquina samples, the reduction was even higher, with up to 44% decrease on the UCS, and 64% reduction on the Young's modulus.

The objective of this thesis was to gain more insight into the mechanical effect of CO_2 solution on carbonate rocks. This was achieved by developing a methodology using numerical models and laboratory experiments. It is still necessary to continue improving the numerical and experimental workflows and the CO_2 injection system set up. For the numerical model, it

would be interesting to add the chemical effect, considering some test parameters, such as flow rate, temperature and reaction time to the DEM contact model. Also, it would be interesting to include the change on pore structure with dissolution in the numerical workflow. In addition, a multi-stage triaxial compressive test may be modeled in the DEM simulations. It is worth mentioning that although the DEM workflow produced stable analyses, it is very computationally intensive. For instance, the uniaxial compressive models took around 14 hours to run, in a computer with Dual Intel(R) Xeon(R) CPU E5-2640 v4 @ 2.40 GHz with 256 GB of RAM, using five cores. The main advantage observed for the DEM is its use as a numerical laboratory, simulating tests that are difficult to perform in the laboratory. Regarding the proposed laboratory workflow, the use of nuclear magnetic resonance before and after the CO_2 injection test would improve the pore structure characterization. Samples of CO_2 solution could also be studied by using inductively coupled plasma optical emission spectroscopy (ICP-OES) to assess the amount of calcite dissolved in the solution, at specific periods of the CO_2 injection procedure. In addition, the flow rate and pressure monitoring must be improved, also allowing permeability measurements. For the next steps, we are planning on performing the CO_2 injection test with constant flow rate, instead of constant injection pressure, and also using a brine solution, instead of deionized water. To be able to perform these tests, the GCTS system set up must be upgraded.

References

Aghababaei, M., Behnia, M., & Moradian, O. (2019). Experimental investigation on strength and failure behavior of carbonate rocks under multistage triaxial compression. *International Journal of Rock Mechanics and Mining Sciences*, *123*(January), 104099. https://doi.org/10.1016/j.ijrmms.2019.104099

Agofack, N., Lozovyi, S., & Bauer, A. (2018). Effect of CO2 on P- and S-wave velocities at seismic and ultrasonic frequencies. *International Journal of Greenhouse Gas Control*, *78*(March), 388–399. https://doi.org/10.1016/j.ijggc.2018.09.010

ASTM. (2008). Standard test method for splitting tensile strength of intact rock core specimens 1 D3967-08. *ASTM International, West Conshohocken, PA, Reapproved*, 20–23. https://doi.org/10.1520/D3967-08.2

Bachu, S. (2008). CO2 storage in geological media: Role, means, status and barriers to deployment. *Progress in Energy and Combustion Science*, *34*(2), 254–273. https://doi.org/10.1016/j.pecs.2007.10.001

Bemer, E., Nguyen, M. T., Dautriat, J., Adelinet, M., Fleury, M., & Youssef, S. (2016). Impact of chemical alteration on the poromechanical properties of carbonate rocks. *Geophysical Prospecting*, *64*(4), 810–827. https://doi.org/10.1111/1365-2478.12387

Berger, K. J., & Hrenya, C. M. (2014). Challenges of DEM : II . Wide particle size distributions. *Powder Technology*, *264*, 627–633. https://doi.org/10.1016/j.powtec.2014.04.096

Boadu, F. K. (1997). Rock properties and seismic attenuation: Neural network analysis. *Pure and Applied Geophysics*, *149*(3), 507–524. https://doi.org/10.1007/s000240050038

Brugada, J., Cheng, Y. P., Soga, K., & Santamarina, J. C. (2010). Discrete element modelling of geomechanical behaviour of methane hydrate soils with pore-filling hydrate distribution. *Granular Matter*, *12*(5), 517–525. https://doi.org/10.1007/s10035-010-0210-y

Cante, J. C., Oliver, X., Weyler, R., Cafiero, M., & Dávalos, C. (2009). Particle finite element method to granular material flow. *International Conference on Particle-Based Methods*, 1–4.

Cha, M., & Santamarina, J. C. (2016). Hydro-chemo-mechanical coupling in sediments:

Localized mineral dissolution. *Geomechanics for Energy and the Environment*, *7*, 1–9. https://doi.org/10.1016/j.gete.2016.06.001

Chehreghani, S., Noaparast, M., Rezai, B., & Shafaei, S. Z. (2017). Bonded-particle model calibration using response surface methodology. *Particuology*, *32*, 141–152. https://doi.org/10.1016/j.partic.2016.07.012

Cho, N., Martin, C. D., & Sego, D. C. (2007). A clumped particle model for rock. *International Journal of Rock Mechanics and Mining Sciences*, *44*(7), 997–1010. https://doi.org/10.1016/j.ijrmms.2007.02.002

Choquette, P. W., & Pray, L. C. (1970). Geologic Nomenclature and Classification of Porosity in Sedimentary Carbonates. *AAPG Bulletin*.

Cundall, P. A., & Strack, O. D. L. (1979). A discrete numerical model for granular assemblies. *Géotechnique*, *29*(1), 47–65. https://doi.org/10.1680/geot.1979.29.1.47

De Simone, M., Souza, L. M. S., & Roehl, D. (2019). Estimating DEM microparameters for uniaxial compression simulation with genetic programming. *International Journal of Rock Mechanics and Mining Sciences*, *118*(July 2018), 33–41. https://doi.org/10.1016/j.ijrmms.2019.03.024

Deen, N. G., Van Sint Annaland, M., Van der Hoef, M. A., & Kuipers, J. A. M. (2007). Review of discrete particle modeling of fluidized beds. *Chemical Engineering Science*, *62*(1–2), 28–44. https://doi.org/10.1016/j.ces.2006.08.014

Deng, Z., Cui, J., Hou, X., & Jiang, S. (2017). Calibration of Discrete Element Heat Transfer Parameters by Central Composite Design. *Chinese Journal of Mechanical Engineering*, *30*(2), 419–427. https://doi.org/10.1007/s10033-017-0072-x

Ding, X., Zhang, L., Zhu, H., & Zhang, Q. (2014). Effect of model scale and particle size distribution on PFC3D simulation results. *Rock Mechanics and Rock Engineering*, *47*(6), 2139–2156. https://doi.org/10.1007/s00603-013-0533-1

Eide, K. E. (2012). *CO2 Sequestration: The effect of carbonate dissolution on reservoir rock integrity* (Número April). Norwegian University of Science and Technology.

Fairhurst, C. (1964). On the validity of the “Brazilian” test for brittle materials. *International Journal of Rock Mechanics and Mining Sciences and*, *1*(4), 535–546. https://doi.org/10.1210/endo.133.1.7686481

Fakhimi, A., & Villegas, T. (2007). Application of dimensional analysis in calibration of a discrete element model for rock deformation and fracture. *Rock Mechanics and Rock Engineering*, *40*(2), 193–211. https://doi.org/10.1007/s00603-006-0095-6

Filho, R. D. G. D. F. (2017). *Dissolution of Carbonate Rocks in High Pressure CO2 /Brine*

Systems: Effects on Porosity and Permeability [Universidade Estadual De Campinas]. www.tcpdf.org

Gozalpour, F., Ren, S. R., & Tohidi, B. (2005). CO2 EOR and storage in oil reservoirs. *Oil and Gas Science and Technology*, *60*(3), 537–546. https://doi.org/10.2516/ogst:2005036

Grgic, D. (2011). Influence of CO2 on the long-term chemomechanical behavior of an oolitic limestone. *Journal of Geophysical Research: Solid Earth*, *116*(7), 1–22. https://doi.org/10.1029/2010JB008176

Gunter, W. D., Bachu, S., & Benson, S. (2004). The role of hydrogeological and geochemical trapping in sedimentary basins for secure geological storage of carbon dioxide. *Geological Society, London, Special Publications*, *233*(1), 129–145. https://doi.org/10.1144/GSL.SP.2004.233.01.09

Haghi, R. K., Chapoy, A., Peirera, L. M. C., Yang, J., & Tohidi, B. (2017). pH of CO2 saturated water and CO2 saturated brines: Experimental measurements and modelling. *International Journal of Greenhouse Gas Control*, *66*(January), 190–203. https://doi.org/10.1016/j.ijggc.2017.10.001

Hawez, H., & Ahmed, Z. (2014). Enhanced oil recovery by CO2 injection in carbonate reservoirs. *WIT Transactions on Ecology and the Environment*, 547–558. https://doi.org/10.2495/ESUS140481

Idelsohn, S. R., Oñate, E., & Del Pin, F. (2003). A Lagrangian meshless finite element method applied to fluid-structure interaction problems. *Computers & Structures*, *81*(8–11), 655–671. https://doi.org/10.1016/S0045-7949(02)00477-7

Institute, A. P. (1998). *Recommended practices for core analysis* (Número Second edition). https://doi.org/10.1016/j.jamcollsurg.2008.01.015

ISRM. (1983). *Suggested methods for determining the strength of rock materials in triaxial compression: Revised version* (Vol. 20, Número 6, p. 285–290). https://doi.org/10.1016/0148-9062(83)90598-3

Jiang, M. J., Konrad, J. M., & Leroueil, S. (2003). An efficient technique for generating homogeneous specimens for DEM studies. *Computers and Geotechnics*, *30*(7), 579–597. https://doi.org/10.1016/S0266-352X(03)00064-8

Kazerani, T., & Zhao, J. (2010). Micromechanical parameters in bonded particle method for modelling of brittle material failure. *International Journal for Numerical and Analytical Methods in Geomechanics*, *34*(18), 1877–1895. https://doi.org/10.1002/nag.884

Koolivand-Salooki, M., Esfandyari, M., Rabbani, E., Koulivand, M., & Azarmehr, A. (2017). Application of genetic programing technique for predicting uniaxial compressive strength

using reservoir formation properties. *Journal of Petroleum Science and Engineering*, *159*(April), 35–48. https://doi.org/10.1016/j.petrol.2017.09.032

Koza, J. R. (1994). Genetic programming as a means for programming computers by natural selection. *Statistics and Computing*, *4*(2), 87–112. https://doi.org/10.1007/BF00175355

Le Guen, Y., Renard, F., Hellmann, R., Brosse, E., Collombet, M., Tisserand, D., & Gratier, J. P. (2007). Enhanced deformation of limestone and sandstone in the presence of high PCO2 fluids. *Journal of Geophysical Research: Solid Earth*, *112*(5), 1–21. https://doi.org/10.1029/2006JB004637

Lebedev, M., Zhang, Y., Sarmadivaleh, M., Barifcani, A., Al-Khdheeawi, E., & Iglauer, S. (2017). Carbon geosequestration in limestone: Pore-scale dissolution and geomechanical weakening. *International Journal of Greenhouse Gas Control*, *66*(September), 106–119. https://doi.org/10.1016/j.ijggc.2017.09.016

Leung, D. Y. C., Caramanna, G., & Maroto-Valer, M. M. (2014). An overview of current status of carbon dioxide capture and storage technologies. *Renewable and Sustainable Energy Reviews*, *39*, 426–443. https://doi.org/10.1016/j.rser.2014.07.093

Li, D., & Wong, L. N. Y. (2013). The brazilian disc test for rock mechanics applications: Review and new insights. *Rock Mechanics and Rock Engineering*, *46*(2), 269–287. https://doi.org/10.1007/s00603-012-0257-7

Lin, H., Xiong, W., Zhong, W., & Xia, C. (2014). Location of the Crack Initiation Points in the Brazilian Disc Test. *Geotechnical and Geological Engineering*, *32*(5), 1339–1345. https://doi.org/10.1007/s10706-014-9800-5

Liu, H., Zou, D., & Liu, J. (2008). Particle shape effect on macro-and micro behaviours of monodisperse ellipsoids. *International Journal for Numerical and Analytical Methods in Geomechanics*, *32*(March 2007), 189–213. https://doi.org/10.1002/nag

Lozano, E., Roehl, D., Celes, W., & Gattass, M. (2016). An efficient algorithm to generate random sphere packs in arbitrary domains. *Computers & Mathematics with Applications*, *71*(8), 1586–1601. https://doi.org/10.1016/j.camwa.2016.02.032

Luquot, L., & Gouze, P. (2009). Experimental determination of porosity and permeability changes induced by injection of CO2 into carbonate rocks. *Chemical Geology*, *265*(1–2), 148–159. https://doi.org/10.1016/j.chemgeo.2009.03.028

Manrique, E., Calderon, G., Mayo, L., & Stirpe, M. T. (1998). Water-alternating-gas flooding in Venezuela: Selection of candidates based on screening criteria of international field experiences. *Proceedings of the European Petroleum Conference*, *2*, 161–169. https://doi.org/10.2118/50645-MS

Marbler, H., Erickson, K. P., Schmidt, M., Lempp, C., & Pollmann, H. (2013). Geomechanical and geochemical effects on sandstones caused by the reaction with supercritical CO2: An experimental approach to in situ conditions in deep geological reservoirs. *Environmental Earth Sciences*, *69*(6), 1981–1998. https://doi.org/10.1007/s12665-012-2033-0

Melo, L. M. P. de. (2012). *Análise numérico-experimental de rochas carbonáticas sintéticas submetidas à injeção de um fluido reativo*. Universidade Federal de Pernambuco.

Menke, H. P., Bijeljic, B., Andrew, M. G., & Blunt, M. J. (2015). Dynamic three-dimensional pore-scale imaging of reaction in a carbonate at reservoir conditions. *Environmental Science and Technology*, *49*(7), 4407–4414. https://doi.org/10.1021/es505789f

Monaghan, J. J. (1994). Simulating free surface flows with SPH. *Journal of Computational Physics*, 399–406.

Monte-Mor, L. S., & Trevisan, O. V. (2016). Laboratory study on carbonate rocks characterization and porosity changes due to CO2 injection. *Brazilian Journal of Petroleum and Gas*, *10*(2), 105–117. https://doi.org/10.5419/bjpg2016-0009

Morschbacher, M. J., Vasquez, G. F., Justen, J. C. R., & Silveira, A. J. P. P. M. (2015). Implicações da interação rocha-fluido na geofísica de reservatórios carbonáticos. *14th International Congress of the Brazilian Geophysical Society*.

Noiriel, C., Luquot, L., Madé, B., Raimbault, L., Gouze, P., & van der Lee, J. (2009). Changes in reactive surface area during limestone dissolution: An experimental and modelling study. *Chemical Geology*, *262*(3–4), 353–363. https://doi.org/10.1016/j.chemgeo.2009.01.032

Nwodo, M. N., Cheng, Y. P., & Minh, N. H. (2016). Sand production modelled with Darcy fluid flow using Discrete Element Method. *International Journal of Environmental, Chemical , Ecological, Geological and Geophysical Engineering*, *10*(2), 154–161. https://doi.org/10.1017/CBO9781107415324.004

Oliveira, A. D. de. (2016). *Análise das alterações físico-químicas decorrentes de ensaio de dissolução em rochas carbonáticas sintéticas*.

Panthi, S., & Hu, L. B. (2014). A discrete element approach for coupled chemo-mechanical mechanisms in geomaterials. *Geo-Congress 2014*, *Rutqvist 2012*, 624–633. https://doi.org/10.1002/cplu.201490022

Peng, C., Crawshaw, J. P., Maitland, G. C., Martin Trusler, J. P., & Vega-Maza, D. (2013). The pH of CO2-saturated water at temperatures between 308 K and 423 K at pressures up to 15 MPa. *Journal of Supercritical Fluids*, *82*, 129–137. https://doi.org/10.1016/j.supflu.2013.07.001

Phillips, J. C., Braun, R., Wang, W., Gumbart, J., Tajkhorshid, E., Villa, E., Chipot, C., Skeel, R. D., Kalé, L., & Schulten, K. (2005). Scalable molecular dynamics with NAMD. *Journal of Computational Chemistry*, *26*(16), 1781–1802. https://doi.org/10.1002/jcc.20289

Poschel, T., & Schwager, T. (2005). *Computational Granular Dynamics*. Springer-Verlag. https://doi.org/10.1007/3-540-27720-X

Potyondy, D. O. (2011). Parallel-bond refinements to match macroproperties of hard rock. *2nd FLAC/DEM Symposium*, *February*, 14–16.

Potyondy, D. O., & Cundall, P. A. (2004). A bonded-particle model for rock. *International Journal of Rock Mechanics and Mining Sciences*, *41*(8 SPEC.ISS.), 1329–1364. https://doi.org/10.1016/j.ijrmms.2004.09.011

Rochelle, C. A., Czernichowski-Lauriol, I., & Milodowski, A. E. (2004). The impact of chemical reactions on CO2 storage in geological formations: a brief review. *Geological Society, London, Special Publications*, *233*(1), 87–106. https://doi.org/10.1144/GSL.SP.2004.233.01.07

Rougier, E., Munjiza, A., & John, N. W. M. (2004). Numerical comparison of some explicit time integration schemes used in DEM, FEM/DEM and molecular dynamics. *International Journal for Numerical Methods in Engineering*, *61*(6), 856–879. https://doi.org/10.1002/nme.1092

Schaef, H. T., & McGrail, B. P. (2005). Direct measurements of pH and dissolved CO2 in H2O-CO2 brine mixtures to supercritical conditions. *Greenhouse Gas Control Technologies*, *II*.

Scholtès, L., & Donzé, F.-V. (2013). A DEM model for soft and hard rocks: Role of grain interlocking on strength. *Journal of the Mechanics and Physics of Solids*, *61*, 352–369. https://doi.org/10.1016/j.jmps.2012.10.005

Šmilauer, V., Angelidakis, V., Catalano, E., Caulk, R., Chareyre, B., & Chèvremont, W. (2021). *Yade Documentation 3rd ed. The Yade Project*. https://doi.org/10.5281/zenodo.5705394

Sulsky, D., Zhou, S. J., & Schreyer, H. L. (1995). Application of a particle-in-cell method to solid mechanics. *Computer Physics Communications*, *87*(1–2), 236–252. https://doi.org/10.1016/0010-4655(94)00170-7

Sun, Y., Aman, M., & Espinoza, D. N. (2016). Assessment of mechanical rock alteration caused by CO2-water mixtures using indentation and scratch experiments. *International Journal of Greenhouse Gas Control*, *45*, 9–17.

https://doi.org/10.1016/j.ijggc.2015.11.021

Sun, Z., Balhoff, M. T., & Espinoza, D. N. (2017). Discrete element modeling of micro-scratch tests on rocks altered by CO2. *American Rock Mechanics Association*.

Sutton, M., Wolters, W., Peters, W., Ranson, W., & McNeill, S. (1983). Determination of displacements using an improved digital correlation method. *Image and Vision Computing*, *1*(3), 133–139. https://doi.org/10.1016/0262-8856(83)90064-1

Tompkins, M. J., & Christensen, N. I. (2001). Ultrasonic P- and S-wave attenuation in oceanic basalt. *Geophysical Journal International*, *145*(1), 172–186. https://doi.org/10.1046/j.0956-540x.2001.01354.x

Vajdova, V., Baud, P., & Wong, T. fong. (2004). Compaction, dilatancy, and failure in porous carbonate rocks. *Journal of Geophysical Research: Solid Earth*, *109*(5), 1–16. https://doi.org/10.1029/2003JB002508

Vaz, R. G. (2017). *Efeitos da dissolução na porosidade e na permeabilidade de dolomitos durante a injeção de água carbonatada*. Universidade Estadual de Campinas.

Velloso, R. Q. (2010). *Simulação Numérica de Problemas de Acoplamento Fluidomecânico em Meios Porosos Utilizando o Método dos Elementos Discretos*. Pontifícia Universidade Católica do Rio de Janeiro.

Vialle, S., & Vanorio, T. (2011). Laboratory measurements of elastic properties of carbonate rocks during injection of reactive CO2-saturated water. *Geophysical Research Letters*, *38*(1), 1–5. https://doi.org/10.1029/2010GL045606

Walton, G., Arzúa, J., Alejano, L. R., & Diederichs, M. S. (2015). A laboratory-testing-based study on the strength, deformability, and dilatancy of carbonate rocks at low confinement. *Rock Mechanics and Rock Engineering*, *48*(3), 941–958. https://doi.org/10.1007/s00603-014-0631-8

Wang, M., & Cao, P. (2017). Calibrating the micromechanical parameters of the PFC2D(3D) models using the improved simulated Annealing Algorithm. *Mathematical Problems in Engineering*, *2017*. https://doi.org/10.1155/2017/6401835

Wu, S., & Xu, X. (2016). A study of three intrinsic problems of the classic discrete element method using Flat-Joint model. *Rock Mechanics and Rock Engineering*, *49*(5), 1813–1830. https://doi.org/10.1007/s00603-015-0890-z

Xu, X., Wu, S., Jin, A., & Gao, Y. (2018). Review of the Relationships between Crack Initiation Stress, Mode I Fracture Toughness and Tensile Strength of Geo-Materials. *International Journal of Geomechanics*, *18*(10), 04018136. https://doi.org/10.1061/(ASCE)GM.1943-5622.0001227

Yasuda, E. Y., Koroishi, E. T., Vidal Vargas, J. A., & Trevisan, O. V. (2018). Dissolution evaluation of Coquina, part 1: Carbonated-brine continuous injection using computed tomography and PHREEQC. *Energy and Fuels*, *32*(4), 5289–5301. https://doi.org/10.1021/acs.energyfuels.7b03970

Yoon, J. (2007). Application of experimental design and optimization to PFC model calibration in uniaxial compression simulation. *International Journal of Rock Mechanics and Mining Sciences*, *44*(6), 871–889. https://doi.org/10.1016/j.ijrmms.2007.01.004

Youn, H., & Tonon, F. (2010). Multi-stage triaxial test on brittle rock. *International Journal of Rock Mechanics and Mining Sciences*, *47*(4), 678–684. https://doi.org/10.1016/j.ijrmms.2009.12.017

Yu, Z., Yang, S., Liu, K., Zhuo, Q., & Yang, L. (2019). An experimental and numerical study of CO2-brine-synthetic sandstone interactions under high-pressure (P)-temperature (T) reservoir conditions. *Applied Sciences (Switzerland)*, *9*(16). https://doi.org/10.3390/app9163354

Zhang, Q., Zhu, H.-H., & Zhang, L. (2015). Studying the effect of non-spherical micro-particles on Hoek-Brown strength parameter mi using numerical true triaxial compressive tests. *International Journal for Numerical and Analytical Methods in Geomechanics*, *39*(1), 96–114. https://doi.org/10.1002/nag.2310

Zhou, X., Zeng, Z., Liu, H., & Boock, A. (2009). Laboratory testing on geomechanical properties of carbonate rocks for CO2 sequestration. *American Rock Mechanics Association*.

A. **Appendix A**

In this section, the main parameters from the CO_2 solution injection tests for samples P03 and P04 are presented. The tests performed are presented in Table 4-2 in Section 4.1.2.2. The results for the test carried out in sample P05 are shown in Section 4.1.2.2.

As discussed before, the fluid mixing tank (FMT) and the confining pressures oscillate during all the tests carried out here. For P03, test parameters are presented in Figure A - 1. The axial and radial strains increased after applying the confining pressure, and decreased when CO_2 solution injection starts. Further, radial strain was almost constant, while axial strain increased around 4 hours of testing, which can indicate sample compaction. The injection flow was kept between 1 and 2 ml/min until around 5 hours of testing, when it decreased to 0.2 ml/min until the end of the test. The temperature from the triaxial cell and the fluid mixing tank decreased during the experiment, as they follow room temperature variations.

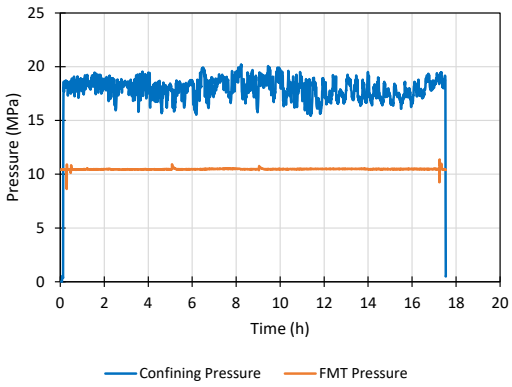

a)

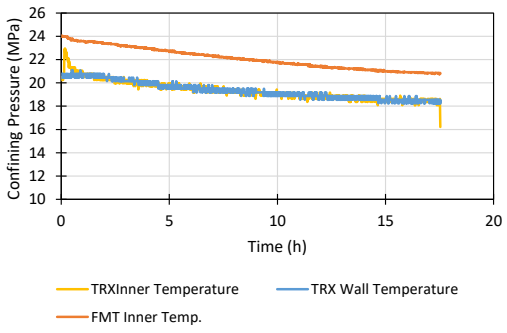

b)

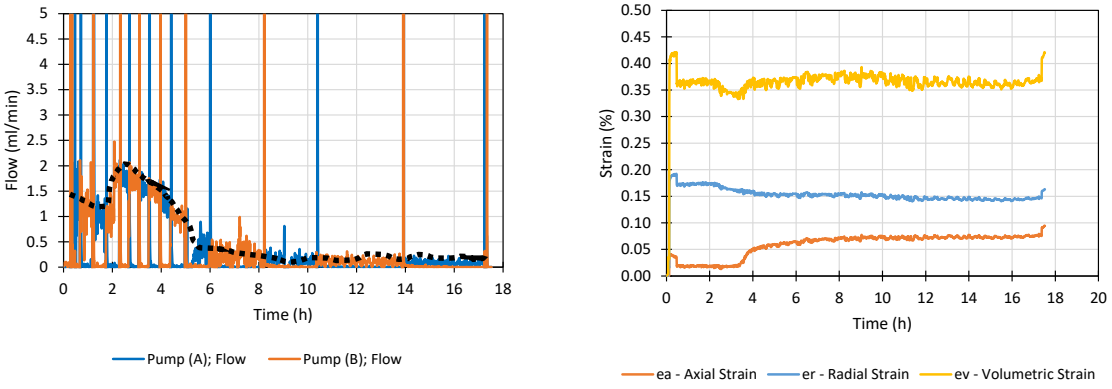

c) d)

Figure A - 1 – Plots obtained during the continuous-flow test on an Indiana Limestone specimen P03. In (a) confining and pore pressures; (b) the inner and wall temperatures of the triaxial cell and the inner temperature of the FMT; (c) pumps A and B flows with the approximately average flow rate in black; and (d) axial, radial and volumetric strains developed during the test.

Figure A - 2 presents the curves from test on P04 sample. It is observed that the flow is very high in the beginning of the test, as the system required a high frequency of refills. On the other hand, after around 8 hours, the flow decreased. Figure A - 2c presents the flow until 8.0 hours of testing, with average flow oscillating between 4.0 and 6.0 ml/min during this period. After 7.5 hours the flow pattern changed significantly, showing very low values, around 0.15 ml/min during this period.

Throughout the test, axial and radial strains were almost constant, except between 5 hours and almost 8 hours of testing. In this period, radial strain decreased, while axial strain increased. This behavior could indicate the occurrence of a compaction process. This is in accordance with the flow pattern during this time interval, when flow starts to decrease.

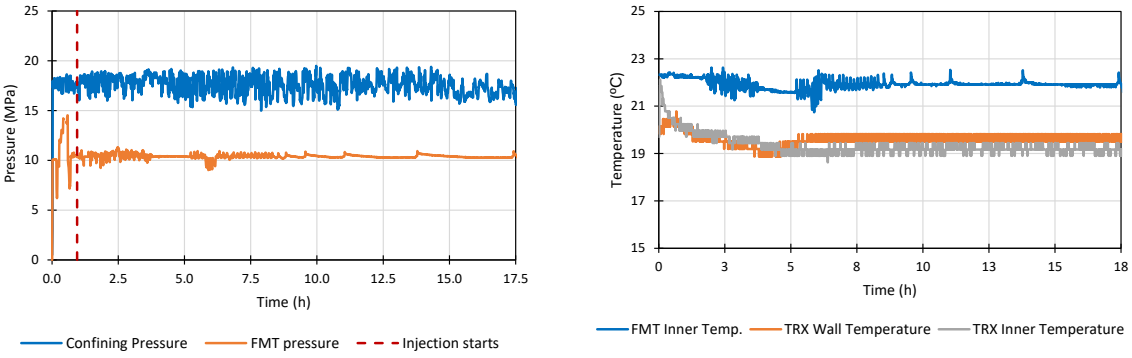

a) b)

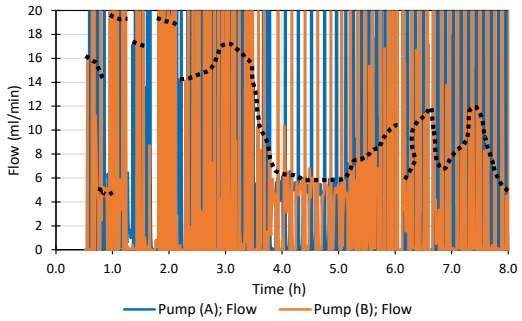

c)

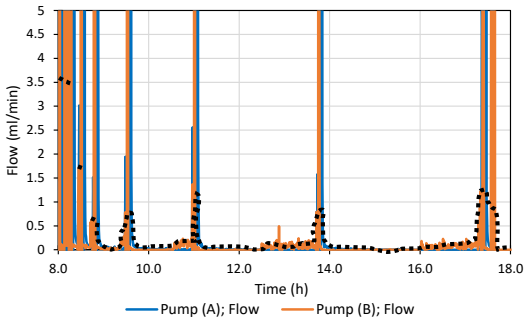

d)

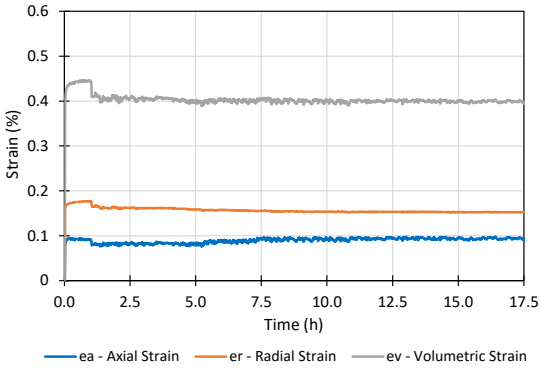

e)

Figure A - 2 – Plots obtained during the continuous-flow test on an Indiana Limestone specimen P04. In (a) confining and pore pressures; (b) the inner and wall temperatures of the triaxial cell and the inner temperature of the FMT; (c) pumps A and B flows from 0.5 to 8.0 hours of testing; (d) pumps A and B flows from 8.0 to 18.0 hours of testing; and e) axial, radial and volumetric strains developed during the test. The approximately average flow rate is represented by the black lines in (c) and (d).

The P and S-waves for the P03 and P04 tests before and after the solution injection are shown in Figure A - 3. The changes observed on the P and S-waves from the beginning to the end of the tests were discussed in Section 4.1.2.3.

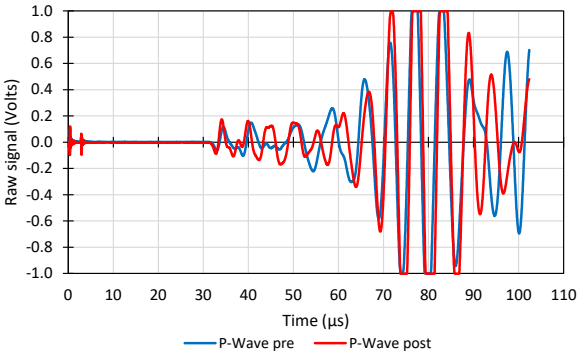

a)

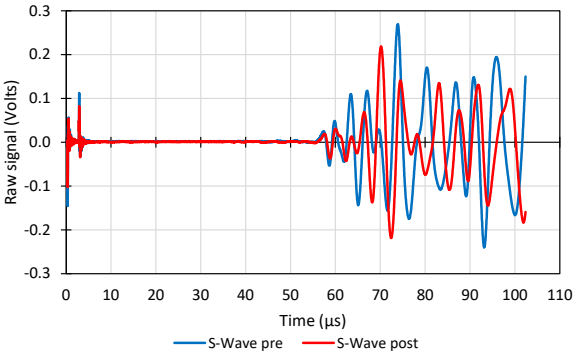

b)

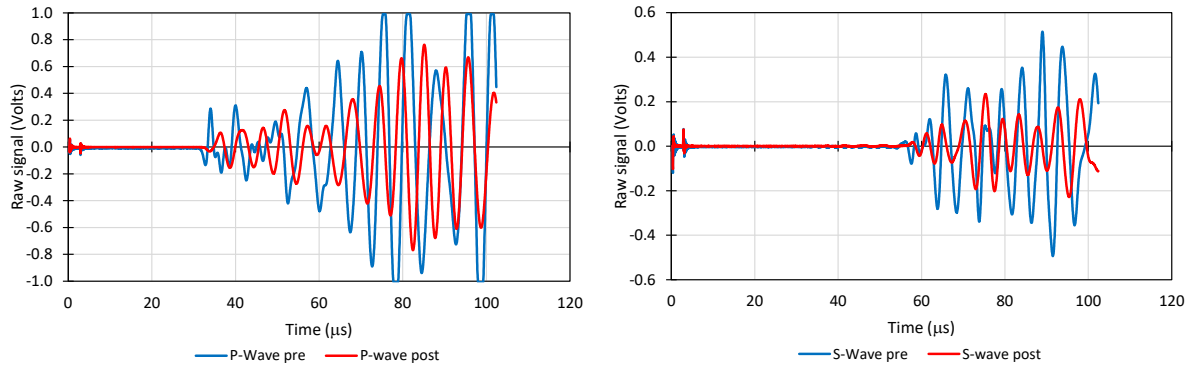

c) d)

Figure A - 3 – a) P-wave and b) S-wave before and after the solution injection in sample P03, and c) P-wave and d) S-wave before and after the solution injection in sample P04.

B. **Appendix B**

To provide a comparison between the two integration methods (finite difference method and the predictor/corrector method) presented in Section 3.1, a simple problem is assessed considering a mass body (m) in an initial position (x_0), with an initial velocity (v_0) and an initial acceleration (a_0). This mass is connected to a spring, with a specific stiffness (k), as presented in Figure B - 1 (initial configuration).

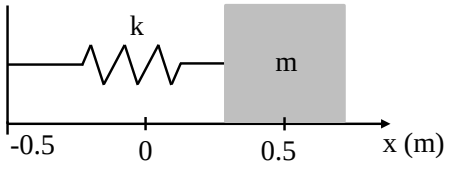

Figure B - 1 – Initial configuration of mass / spring system used in the example.

This problem is assessed using three different approaches: analytical solution, finite difference integration and Gear's integration (predictor/corrector). The values used in this model are presented in Table B - 1.

Table B - 1 – Input data used in the example.

Mass (kg)	1
Spring stiffness (N/m)	10
Initial position (m)	0.5
Initial velocity (m/s)	0
Final time (s)	10

The results are presented for this problem using different time increments (Δt). Figure B - 2 presents the comparison between the three approaches with $\Delta t = 0.2$.

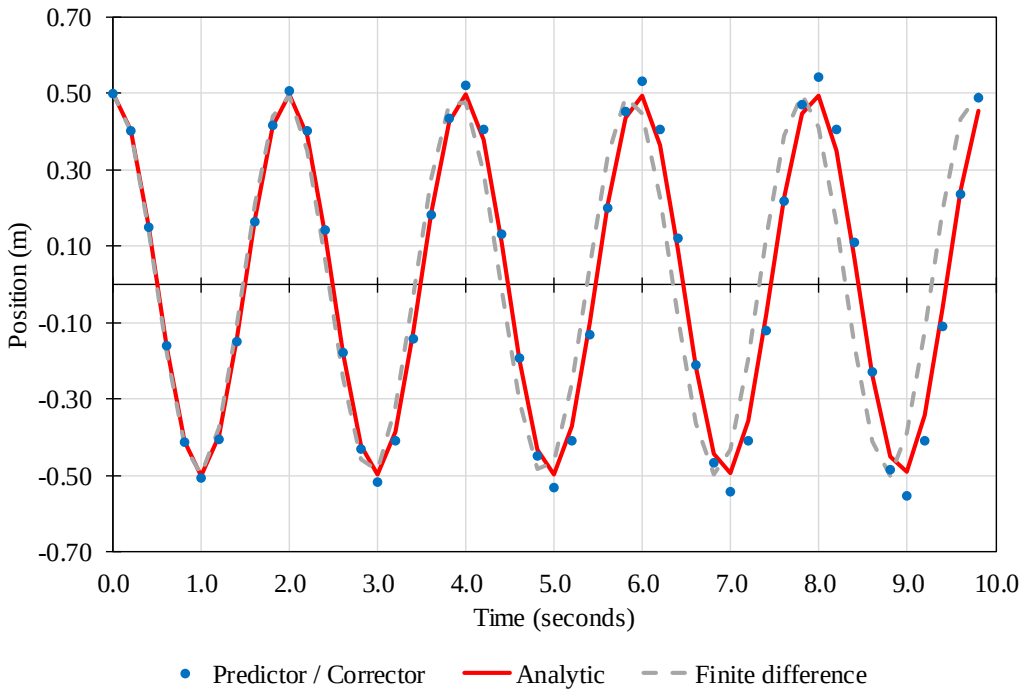

Figure B - 2 – Mass position according to three methodologies using $\Delta t = 0.20$ seconds.

The predictor-corrector achieves a more accurate result than the finite difference. On the other hand, the maximum and minimum positions from Gear's integration are higher than the analytical and the finite difference methods in modulus. This represents a worse stability condition in this method, which means that the body energy is increasing with time. Figure B - 3 describes the mass position in time, considering the time increment $\Delta t = 0.15$.

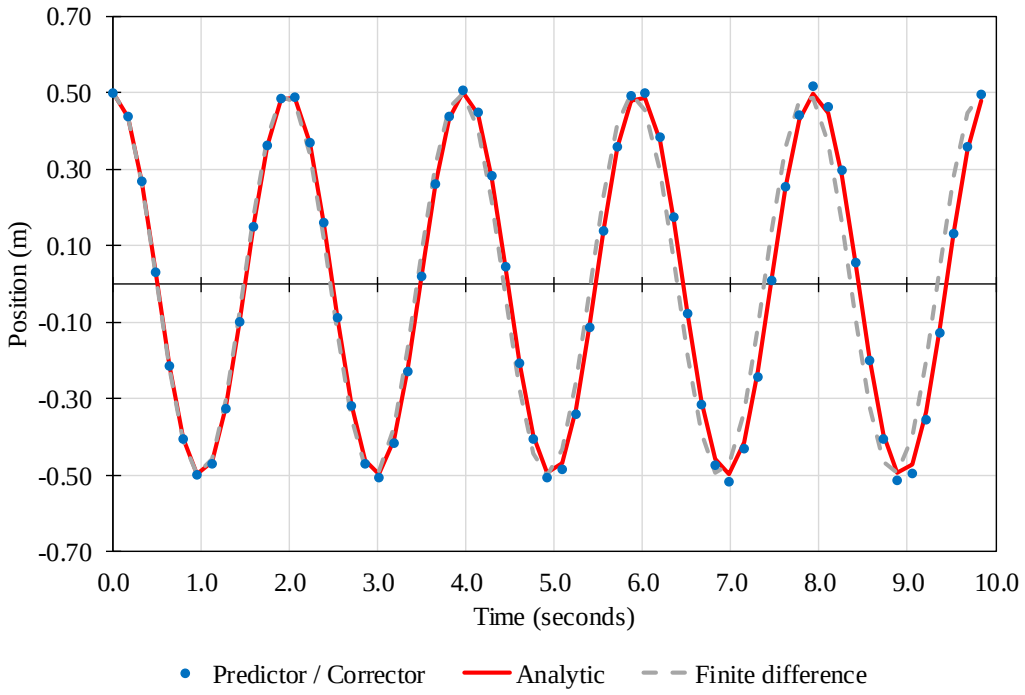

Figure B - 3 – Mass position according to three methodologies using $\Delta t = 0.15$ seconds.

The results from Figure B - 3 are similar to the ones from Figure B - 2, showing an energy increase with Gear's integration but a more accurate result, when compared to the finite difference scheme.

Figure B - 4 shows the mass position in time, considering three approaches: predictor/corrector, analytical solution and finite difference method for $\Delta t = 0.1$ seconds.

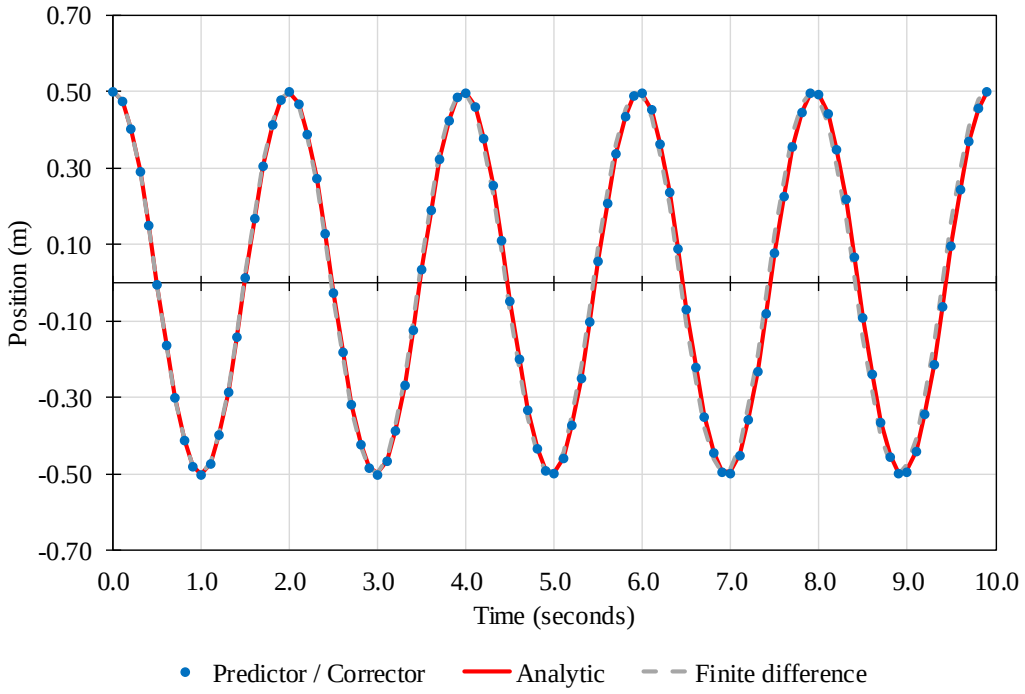

Figure B - 4 – Mass position according to three methodologies using $\Delta t = 0.10$ seconds.

In Figure B - 4, both numerical integrations are in good agreement with the analytical result. At the end of 10 seconds, it is possible to see that the values from Gear's integration are closer to the analytical solution than the finite difference values.

According to these results, Gear's integration (predictor/corrector) method is more accurate but less stable, when compared to the finite difference method. This conclusion is similar to the one presented in Rougier et al. (2004). In that work, the authors compare some of the integration schemes used in computational mechanics. Consequently, in this study, the finite difference will be used in the DEM code, once this integration method is easier to implement, and more stable than Gear's integration scheme.